UNIVERSIDADE FEDERAL DO PARANÁ

LUCAS FEDALTO SARTORI

CALIBRATION AND MIXING SIMULATIONS OF FINE POWDERS USING A COARSE-GRAINED MODEL AND PRIMITIVE PARTICLE SHAPES ON A DISCRETE ELEMENT METHOD (DEM) FRAMEWORK

CURITIBA PR

2023

LUCAS FEDALTO SARTORI

CALIBRATION AND MIXING SIMULATIONS OF FINE POWDERS USING A COARSE-GRAINED MODEL AND PRIMITIVE PARTICLE SHAPES ON A DISCRETE ELEMENT METHOD (DEM) FRAMEWORK

Dissertação apresentada ao Programa de Pós-Graduação em Engenharia Química, do Setor de Tecnologia da Universidade Federal do Paraná, como requisito parcial para a obtenção do título de Mestre em Engenharia Química..

Área de concentração: *Engenharia Química*.

Orientador: Prof. Dr. Fernando Augusto Pedersen Voll.

Coorientador: Prof. Dr. Nicolin Govender.

CURITIBA PR

2023

DADOS INTERNACIONAIS DE CATALOGAÇÃO NA PUBLICAÇÃO (CIP)
UNIVERSIDADE FEDERAL DO PARANÁ
SISTEMA DE BIBLIOTECAS – BIBLIOTECA DE CIÊNCIA E TECNOLOGIA

Sartori, Lucas Fedalto
Calibration and mixing simulations of fine powders using a coarse-grained model and primitive particle shapes on a discrete element method (DEM) framework / Lucas Fedalto Sartori. – Curitiba, 2023.
1 recurso on-line : PDF.

Dissertação (Mestrado) - Universidade Federal do Paraná, Setor de Tecnologia, Programa de Pós-Graduação em Engenharia Química.

Orientador: Fernando Augusto Pedersen Voll
Coorientador: Nicolin Govender

1. Sólidos. 2. Método dos Elementos Discretos. 3. Calibração. I. Universidade Federal do Paraná. II. Programa de Pós-Graduação em Engenharia Química. III. Voll, Fernando Augusto Pedersen. IV. Govender, Nicolin. V. Título.

Bibliotecário: Elias Barbosa da Silva CRB-9/1894

TERMO DE APROVAÇÃO

Os membros da Banca Examinadora designada pelo Colegiado do Programa de Pós-Graduação ENGENHARIA QUÍMICA da Universidade Federal do Paraná foram convocados para realizar a arguição da Dissertação de Mestrado de **LUCAS FEDALTO SARTORI** intitulada: **CALIBRATION AND MIXING SIMULATIONS OF FINE POWDERS USING A COARSE-GRAINED MODEL AND PRIMITIVE PARTICLE SHAPES ON A DISCRETE ELEMENT METHOD (DEM) FRAMEWORK**, sob orientação do Prof. Dr. FERNANDO AUGUSTO PEDERSEN VOLL, que após terem inquirido o aluno e realizada a avaliação do trabalho, são de parecer pela sua APROVAÇÃO no rito de defesa.

A outorga do título de mestre está sujeita à homologação pelo colegiado, ao atendimento de todas as indicações e correções solicitadas pela banca e ao pleno atendimento das demandas regimentais do Programa de Pós-Graduação.

CURITIBA, 06 de Setembro de 2023.

Assinatura Eletrônica
12/09/2023 10:13:10.0
FERNANDO AUGUSTO PEDERSEN VOLL
Presidente da Banca Examinadora

Assinatura Eletrônica
12/09/2023 14:15:23.0
MARCO ANDRE ARGENTA
Avaliador Externo (DEPARTAMENTO DE CONSTRUÇÃO CIVIL - UFPR)

Assinatura Eletrônica
12/09/2023 10:47:35.0
ALEXANDRE FERREIRA SANTOS
Avaliador Interno (UNIVERSIDADE FEDERAL DO PARANÁ)

Ne dovete mangiare ancora
di pastasciutta

iacta alea est

ACKNOWLEDGEMENTS

I'd like to acknowledge my "national" advisors, Profs. Fernando Voll, Alexandre F. Santos, Eliton Fontana and Luiz Fernando Luz Jr., for their trust and support for the last two years;

On that note, thanks to my "international" advisor, Prof. Nicolin Govender, for his genuine interest in my development as a DEM/bulk solids engineer;

Thanks to everyone at the BlazeDEM group for always being willing to help;

Thanks to my friends from CFDEQ, in particular Elivaldo Sapucaia and João Segatto for their help in making my experiments work and/or reconnecting the computer on the university's weekly power loss;

Thanks to Andrew Kondlatsch, Lucas Cava and Ben Trank for maintaining and supporting this project;

Thanks to Victor Vieira for massively helping with a lot of the experimental work;

Thanks to Camila F. for providing her opinion on some figures. All complaints about the images here shown should be directed at her;

In all seriousness, thank you, my wife, for your patience, friendship and sacrifice. *L'amore è un faro fisso che sovrasta la tempesta*;

Special thanks to my dear friend Devin Garrett Townsend for outstanding moral and philosophical support.

RESUMO

O Método dos Elementos Discretos (DEM) é uma ferramenta para simular e prever o comportamento macroscópico de sólidos particulados. Porém, a escala dos processos industriais envolvendo estes sólidos implica em custos computacionais proibitivamente altos. Uma forma de se reduzir o número de partículas e melhorar a viabilidade do DEM em escalas industriais é o *Coarse Grain Modeling* (CGM), que agrupa partículas em grãos maiores mas ainda alcança resultados realísticos de simulação. Aqui, o CGM é demonstrado pela calibração – o processo pelo qual parâmetros de sólidos são obtidos – para dois pós finos, um deles coesivo, utilizando tanto partículas poliédricas como esféricas. Experimentos que produzem um Ângulo de Repouso (AoR) são realizados e simulados; os parâmetros que reproduzem AoRs experimentais com sucesso são tomados como os parâmetros do material. Dois experimentos são aqui usados: o *ledge test*, que produz um ângulo de repouso estático ao deixar material confinado em uma caixa escoar e formar uma pilha; e o *rotating drum*, que é único por fornecer AoRs dinâmicos. A calibração foi feita utilizando-se partículas 30x maiores que seu tamanho original e os resultados foram comparados às mesmas simulações em escalas variadas, para avaliar os limites do CGM. O *ledge test* teve um bom comportamento com o redimensionamento, mas na escala de 40x teve um aumento de cerca de cinco graus. Isto é causado por efeitos gravitacionais terem influência diminuta com partículas mais pesadas. No *rotating drum*, há uma pronunciada redução nos ângulos de repouso quando partículas poliédricas são reduzidas para o tamanho real. Foi proposto que os pesos reduzidos são mais permissivos ao rearranjo de partículas, reduzindo assim os ângulos de repouso pelo intertravamento mais intenso. A inclusão do parâmetro de coesão amplifica este efeito, pois a lei de contato de coesão varia com a escala; a redução do tamanho de partículas causa um aumento relativo nas forças de atração. Por fim, cinco misturas entre os dois materiais, numa proporção 70/30 entre o material não-coesivo (FFM) e coesivo (CM), respectivamente, foram feitas num *In-Bin Blender* (IBB) com variadas velocidades de rotação (10 a 20 RPM) e preenchimento (45 à 70% em volume). Quando simuladas estas misturas, os parâmetros previamente calibrados foram incapazes de reproduzir os resultados experimentais. Entendendo-se os mecanismos de mistura, uma série de modificações aos parâmetros originais foi proposta; talvez de maior relevância, um parâmetro adesivo artificial FFM-CM foi usado para melhor modelar o formato de partículas e a consequente redução nas taxas de percolação. Foi demonstrado que, para RPMs baixos, o número total de revoluções é o parâmetro chave que controla a homogeneidade das misturas. Em termos de preenchimento, a mistura com 45% teve a melhor performance entre todas as cinco, em decorrência do *headspace* maior aumentar as taxas de mistura – em contrapartida, a quebra de partículas foi maior se comparada a casos com maior preenchimento. Todos os resultados indicam a importância do formato de partículas ao se modelar misturas com grandes razões entre tamanhos, pois o AoR é insuficiente para caracterizar sólidos nestas circunstâncias.

Palavras-chave: Solidos Particulados DEM Calibração

ABSTRACT

The Discrete Element Method (DEM) is a tool to simulate and predict particulate solid bulk behaviour. However, the scale of industrial processes involving these solids means that the computational effort to simulate them is prohibitively high. One approach to reducing particle count and improving the feasibility of DEM at the industrial scale is Coarse Grain Modeling (CGM), which groups individual particles into larger grains but can achieve realistic simulation results. Here, CGM is demonstrated via the calibration – the process by which solid parameters are obtained – of two powdered solids, one of which cohesive, using both polyhedral and spherical particles. Experiments that produce an Angle of Repose (AoR) are performed and then simulated; the parameters that successfully reproduce experimental AoRs are then taken to be the materials' parameters. Two experiments are here used: the ledge test, which produces a static angle of repose by letting material confined in a box flow out and form a pile; and the rotating drum, which is unique in giving a dynamic AoR. Calibration was performed using particles 30x bigger than their original size and results were compared to the same simulations on smaller and bigger scales, to evaluate the limits of CGM. The ledge test performed well upon scaling, but at 40x scaling for the free-flowing material had an increase in AoR of about five degrees. This is due to gravitational effects becoming less dominant with heavier particles. On the rotating drum, there is a pronounced reduction in repose angles for polyhedra when scales are reduced to real-size. It was proposed that reduced particle weights are more permissive to particle rearrangement, thus reducing angles of repose by the more intense interlocking of particles. With the inclusion of a cohesive parameter, this effect is amplified as the cohesion force law is variant with size; as particle sizes are reduced, there is a relative increase in attractive forces. Finally, five mixtures of both materials, at a 70/30 split for the free flowing (FFM) and cohesive (CM) materials, respectively, were performed in a lab-scale In-Bin Blender (IBB) with varying rotational speeds (10 to 20 RPM) and fill percentages (45 to 70% volume). When simulating these mixtures, previously calibrated parameters were unsuccessful in reproducing experimental results. By understanding the underlying mixing mechanisms, a series of modifications to the original parameters were proposed: perhaps more importantly, an artificial FFM-CM adhesive parameter was used to better account for particle shapes and reduce percolation rates. In the RPM-varying cases, it was demonstrated that for low RPM ranges, number of revolutions is the key controlling parameter to mixing quality. In terms of fill percentages, the 45% case had the best performance between all mixtures, due to mixing rates being aided by the larger headspace – although particle breakage was increased if compared to higher fillings. All results point to the importance of considering particle shape when modelling mixtures with high size ratios, as the AoR is not sufficient as a characterization parameter under these circumstances.

Keywords: Powdered Solids DEM Calibration

LIST OF FIGURES

LIST OF TABLES

LIST OF ACRONYMS

DEM	Discrete Element Method
CPU	Core Processing Unit
GPU	Graphics Processing Unit
CGM	Coarse-Grain Model
AoR	Angle of Repose
CUDA	Compute Unified Device Architecture
PLA	Polylactic Acid
IBB	In-Bin Blender
FFM	Free-Flowing Material
CM	Cohesive Material

CONTENTS

1 INTRODUCTION

The largest ever Discrete Element Method (DEM) simulation to date was produced by three Japanese scientists at the Japan Agency for Marine-Earth Science and Technology (JAMSTEC); it was a simulation of the fault formation in accretionary prisms, a phenomenon related to earthquakes, on a square metre of sand.[1] At 1.9 billion particles – approximately 0.019 m^3 – and five seconds of simulation, it was run on 36% of the available nodes at the JAMSTEC's Earth Simulator, the world's 51^{th} most powerful supercomputer.[2] It took a full 24h to finish.

A real-time simulation run, however, was achieved on 4,000 nodes of the K Computer (Riken Institute, Japan), at the time of its decommission the 20^{th} fastest computer of its kind.[3] Both supercomputers have a peak performance of approximately 10 petaFLOP/s,[†] while the fastest CPUs commercially available peak at 0.0016 petaFLOP/s.[4] A direct, numerical comparison is imprecise, since supercomputers are designed to be highly specialized, as well as more expensive to build, maintain and operate. The work of Dr. Nishiura and colleagues – perhaps unwittingly – exposes the challenges and impediments of DEM.

DEM is a numerical method used to compute the behaviour of particulate, non-continuous solids in motion, by treating every single particle as a *discrete element*, each independent from all others.[5] Through Newton's Laws of motion, changes in the relevant *momenta* are calculated from the forces between two or more colliding particles and integrated over time, which is subdivided into time steps (usually on the order of 10^{-5} seconds or less). Under the usual assumption of "soft particles", particles are allowed to overlap, which is used as the basis to calculate forces using a parallel spring-and-dashpot model. The key computational aspects of DEM are detecting whether or not a collision has occurred; determining the geometric nature of each overlap; and calculating the forces arising from these interactions at every time step.

As outlined above, the framework of DEM is relatively simple; and yet, the supercomputers were needed. Assuming a time step of 10^{-5}, the five simulated seconds would equal 500,000 time steps in total. This would also be the number of times that all calculations – from detecting collisions to calculating forces – would have to be done for all 1.9 billion particles, which puts the total number of calculations near the one quadrillion mark. It shows how unavoidably colossal the endeavor of DEM can be, from no more than 20 litres of sand thinly spread on a square metre.

The technical prowess of their work lies in achieving a very high degree of parallelization of calculations, which suits DEM particularly well since each particle is an independent entity. For each time step, particle calculations are distributed over the large network of computer nodes and run simultaneously. Common available DEM solvers that run on CPUs, such as LIGGGHTS, have limited parallelism, since most computers have a single processor with a relatively low number of cores. The architecture of GPUs, on the other hand, is specifically geared towards parallel computing; with thousands of individual cores per unit, GPU computing is an attractive platform for DEM codes. Notably, Ansys and ESSS have recently entered the DEM market with Rocky, a multi-GPU DEM software with multi-physics integration.[6] Free or open-source codes are available as well; in this work, Blaze-DEM,[7] an open-source and GPU-based DEM code is used.[‡]

In industrial applications, where the number of particles can nonchalantly go above billions, real-scale simulations are prohibitively expensive – computationally, temporally, energetically –, so that DEM can appear to be of no practical use. An approach to reduce the number

[†]FLOP/s = Floating Point Operations per second, a measure of computing performance.

[‡]Newer versions are closed-source, but available for free for academic partners.

of particles whilst maintaining the realism of simulations, and thus providing useful information, is hence needed. The Coarse-Grain Model (CGM) substitutes a certain number of individual particles into larger "grains", reducing the number of discrete elements of a given simulation.[8] Coarse-Grain modelling has been widely reported for spherical particles, but little has been done with real-shaped particles – partly because of the added computational costs involved in simulating polyhedra.

Here, the idea of upscaling particles to a more amenable size and a reduced number was explored via the calibration of two powdered solids, one of which cohesive, using real-shaped particles. Calibration, in the context of particulate solids, is the procedure by which a set of physical parameters that describe its bulk behaviour is obtained. A series of experiments were performed with a given solid, and attempts at simulating these experiments by successive guessing of parameters – mainly the static and rolling friction coefficients – were made. Those that accurately reproduced the Angle of Repose (AoR) in multiple experiments were taken to be the solid's properties, that can then be used in other simulations. The goal was to determine if particle behaviour is, in fact, invariant with size by comparing experimental results with calibration at different scales. Finally, laboratory-scale mixtures of both solids were modeled in DEM.

The statistician George Box stated throughout his career that "all models are wrong, but some are useful", an idea that can be extended to scientific and mathematical models as well.[9] In creating models of particle behaviour, we are creating something that is fundamentally wrong, but correctly predictive in specific situations – this is applicable to CGM, but more broadly to DEM itself. That is a key aspect that underlies most of this work: the aim is to get close enough (but not necessarily quite) to the "real" answer, so as to extract a useful and practical model. Moreover, understanding how and why the model of DEM works is imperative to understanding when it works, and when it does not, so that it can be properly used as a tool.

2 LITERATURE REVIEW

2.1 THE DISCRETE ELEMENT METHOD AND COARSE-GRAIN MODELLING

2.1.1 Introduction

The Discrete Element Method (DEM) is a numerical technique useful for the calculation of the motion and interaction of small solid particles.[10] Applications are found in diverse fields, such as deep-sea mining and general mining operations,[11,12] agriculture,[13] geomechanics,[14] pharmaceuticals,[15] and food industries.[16–18] Since DEM algorithms have to account for the position and kinetic conditions of a large number of particles, it may take a large amount of computational resources to complete a given simulation, which may lead to very large simulation times. One interesting strategy to circumvent this issue is the use of GPU-based acceleration, making use of their parallelized processing power to achieve relatively quick simulations.[7] DEM, as such, is a powerful tool with many applications but with short-term challenges that make it an interesting long-term field of study.

Paralellization in CPUs is indeed possible – in fact, in the JAMSTEC paper discussed in the Introduction, a supercomputer "node" refers to individual computers having one or more CPUs – and in terms of raw processing speed, a CPU core has generally faster clock speeds than a GPU core. However, CPUs are designed to perform sequential calculations, and to have one instance of a program running on multiple CPUs requires some specific and complex coding to distribute tasks between CPUs.[19–21] GPU programming is made easier by Nvidia's CUDA (Compute Unified Device Architecture), a parallel computing platform designed to facilitate GPU computing.

Movement of particles is calculated by Newton's laws of motion. For a body moving through space, its linear and angular *momenta* are altered by forces F and torques τ, respectively, given by:

$$\begin{aligned} F &= m\frac{dv}{dt} \\ \tau &= I\frac{d\omega}{dt} \end{aligned} \tag{2.1}$$

where m and v are mass and velocity, respectively, while I and ω, the moment of inertia and angular velocity, their rotational counterparts.

Both velocities must be obtained by time integration of Equations 2.1, where time t is discretized into user-defined time steps. The stability of a given simulation is dependent on the choice of time step, and it must not exceed the critical time step. It is mostly a function of particle size (R) and the Young's modulus (E), being directly proportional to the former and inversely proportional to the latter (Equation 2.2).

$$\Delta t_{crit} = \frac{\pi R}{0.8766 + 0.163\upsilon}\sqrt{\frac{\rho}{E}} \tag{2.2}$$

Since particle density and size (which, in turn, allows computation of individual particle mass) are provided by the user, the problem now reduces to determining the magnitude of forces acting on particles. In section 2.2, a more detailed overview of how forces are calculated by BlazeDEM is given. It's specific to the software at hand, but similar to other DEM codes (e.g. LIGGGHTS).

2.1.2 Coarse Grain Modelling

Coarse Grain Modelling (CGM) consists in representing a small group of particles by one upscaled particle, thus reducing the overall number of entities in a simulation.[8] The scaling factor (f_{CGM}) reduces the particle count of a simulation by f_{CGM}^3, since particles are three-dimensional entities. The advantage of such an approach is self-evident in the context of DEM, since doubling particle diameter reduces particle count by a factor of 8; furthermore, since particle diameter is a key variable in defining the critical time step, using CGM also increases simulation speed by increasing the values of time step at which it is stable.

For CGM to work as a model, it must be able to reproduce bulk behaviour at increased scales. Bierwisch *et al.* have demonstrated a set of scaling rules for normal, tangential and cohesive damping that, when applied to upscaled particles, maintain bulk properties, flow-rates and angles of repose unaffected by scaling.[8] Furthermore, the Hertz and Mindlin force models (described in section 2.2) are invariant with particle size, provided that physical parameters (such as density and Young's modulus) are kept constant.[22–24] However, upscaling is limited by the size and geometry of the equipment; the upscaled particle must be of a dimension much smaller than the equipment being considered.[25] In general, the ratio between the characteristic length of equipment and particles should be no less than 25.[26]

2.2 CONTACT MODELS

Force calculations are based on the seminal work of Cundall and Strack,[27] in which normal and tangential contacts are each modelled as parallel spring-dashpot systems. Time is discretized into timesteps and, for each timestep, forces arising from these contacts are computed. The viscous dashpot dissipates some collision energy due to (non-simulated) particle deformation, while the spring is an elastic component that stores kinetic energy.[28] Solids that display this viscoelasticity are called Kelvin-Voigt materials, and the general form of their stress-strain behaviour is given by:[29]

$$\sigma = E\varepsilon + \eta\varepsilon \tag{2.3}$$

where E is the Young's Modulus and η the viscosity. Strain ε is equal in both spring and dashpot due to their parallel configuration, meaning that the distribution between dissipative and elastic forces is controlled by their respective coefficients. Force models in DEM differ in their description of such coefficients, applying Equation 2.3 in terms of force rather than stress; E and η then become a spring stiffness K [N/m] and a viscous damping coefficient C [N.s/m], respectively. Since stress has units of force per area, Equation 2.3 can be rearranged as:

$$F_i = K_i\delta_i - C_iV_{rel} \tag{2.4}$$

the subscript i denotes force direction, V_{rel} is the relative velocity and the negative sign in the viscous part of the equation denotes that it is a dissipative force. For spherical particles, the displacement δ is calculated using a soft-sphere model, in which particles are allowed to overlap and the displacement comes from the depth of indentation – formally, for two overlapping particles A and B, $\delta = R_A + R_B - d$ where R_i are particle *radii* and d is the distance between particle centres.[30] Displacement in polyhedral particles, which is further discussed in the normal contact models section, is calculated based on the overlap volume of two particles using the same soft-particle concept.[31,32]

2.2.0.1 *Common Definitions*

The following definitions, if applicable, are valid for all force models, both for spheres and polyhedral particles. Since forces and displacements are equal between two distinct elements in contact,[33] material properties used in calculations are a combination of the individual properties of materials involved in a given collision – these combined parameters are called equivalent (or reduced) properties and are here denoted by an asterisk:[34]

$$\begin{aligned} m^* &= \left(\frac{1}{m_A} + \frac{1}{m_B}\right)^{-1} & E^* &= \left(\frac{1-\upsilon_A^2}{E_A} + \frac{1-\upsilon_B^2}{E_B}\right)^{-1} \\ R^* &= \left(\frac{1}{R_A} + \frac{1}{R_B}\right)^{-1} & G^* &= \left(\frac{2(2-\upsilon_A)(1+\upsilon_A)}{E_A} + \frac{2(2-\upsilon_B)(1+\upsilon_B)}{E_B}\right)^{-1} \end{aligned} \tag{2.5}$$

where the relevant material properties are mass (m); radius (R); Young's modulus (E); Poisson's ratio (ν); and shear modulus (G), with A and B again representing two overlapping discrete elements. Surfaces are treated as particles of infinite mass and radius (i.e. as elastic half-spaces); the relations in 2.5 are valid with R^* and m^* equal to the particle's radius and mass, respectively.[35] Other material properties, such as friction coefficients and cohesion parameters, are calculated as the average of the values set for each individual material.

2.2.1 Normal Contact Models

Normal forces are the cornerstone of DEM modelling, since all other forces are directly or indirectly correlated. In BlazeDEM, two normal contact models are available, both based on a parallel spring-dashpot system: **LinearSpringDash**, which models the spring and dashpot as linearly increasing elements; and **HertzSpringDash**, which uses the Hertzian theory of contacts to account for non-linearities in spring stiffness. An illustration of the spring-dashpot modelling of a normal contact is presented in Figure 2.1. The overlapping region is exaggerated for ease of viewing – for a properly set timestep, the superposition of particles is much more limited.

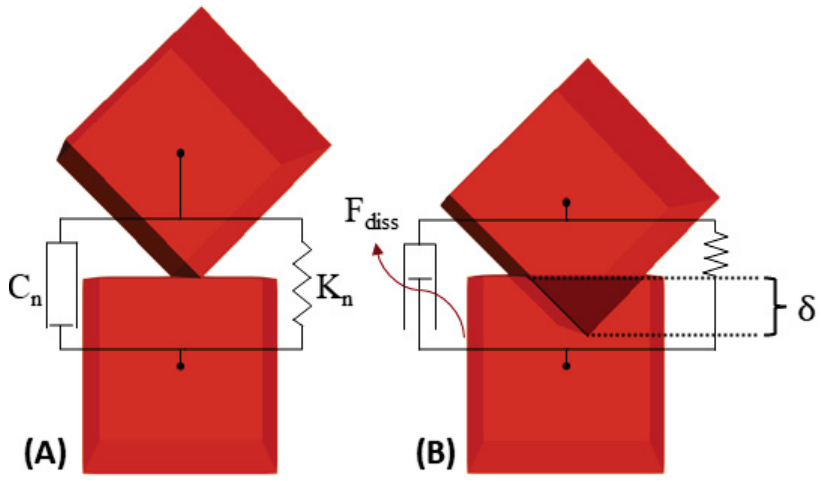

Figure 2.1: Schematic representation of the spring-dashpot model (A) before and (B) after normal collision. When particles overlap, a normal displacement δ_n causes a proportional contraction of the spring and of the dashpot.

2.2.1.1 LinearSpringDash

In the linear spring-dashpot model, both spring stiffness K_n and damping coefficient C_n are constant. Therefore, both elements respond linearly to an increase in displacement. Equation 2.4 can then be rewritten as:[36]

$$F_n = (K_n \delta_n)\,\bar{n} - (C_n V_{rel} \cdot \bar{n})\,\bar{n} \tag{2.6}$$

the equation is vectorized by inclusion of the normal vector $\bar{n}$; the dot product $V_{rel} \cdot \bar{n}$ is the normal relative velocity component. Furthermore, the above constants are functions of equivalent mass (m^*, Equation 2.5), coefficient of restitution (e) and contact duration ($t_{contact}$), which is set as a multiple of the timestep:[32]

$$K_n = \frac{m^*}{t_{contact}^2} \ln(e)^2 + \pi^2 \tag{2.7}$$

$$C_n = \frac{2 \ln(e) \sqrt{K_n m^*}}{\sqrt{\ln(e)^2 + \pi^2}} \tag{2.8}$$

By default, when using LinearSpringDash, computation of displacement δ_n in polyhedra is given by:[32]

$$\delta_n = n\sqrt[3]{v} \tag{2.9}$$

where v is the overlapping region volume and n is a positive real number that modulates particle softness.

2.2.1.2 HertzSpringDash

Hertzian contact theory assumes that the load distribution of two discrete elements in contact forms an area of elliptical shape, if displacements are much smaller compared to the particles' dimensions.[33] From these assumptions, a new formulation for spring stiffness arises:[37]

$$K_n = \frac{4}{3} E^* \sqrt{R^* \delta_n} \tag{2.10}$$

$$C_n = \beta \sqrt{5 K_n m^*} \tag{2.11}$$

$$\beta = \frac{\ln(e)}{\sqrt{\ln^2(e) + \pi^2}} \tag{2.12}$$

As in the LinearSpringDash model, Equation 2.6 is used as the basic mathematical layout for normal contacts; K_n, and by extension C_n, are now dependant on displacement, such that force computations now have a non-linear dependence on δ_n:

$$F_n = \left(\frac{4}{3} E^* \sqrt{R^*} \delta_n^{\frac{3}{2}}\right) \bar{n} - \left(\beta \sqrt{5 K_n m^*} V_{rel} \cdot \bar{n}\right) \bar{n} \tag{2.13}$$

HertzSpringDash is particularly well suited to spherical contacts, since the underlying model was developed assuming curved contacts.[38] For spheres, as previously discussed, displacement is $\delta = R_A + R_B - d$; for polyhedra under the HertzSpringDash model:

$$\delta_n = \sqrt{v.d} \tag{2.14}$$

where d is a distance measurement from the plane of contact. Since the overlap volume tends to grow unevenly for polyhedra, this model may not work properly for non-spherical simulations.

2.2.2 Tangential Contact Models

A relative velocity in the tangential direction (e.g. perpendicular to the normal $\bar{n}$) between two discrete elements causes shearing forces due to friction, again modelled by a spring and dashpot pair. These frictional forces are related to normal forces by a friction coefficient μ, which acts as a mechanical slider in the spring-dashpot framework.[39] Moreover, a stick-slip model is applied together with the Coulomb criterion, given by:[40]

$$\|F_t\| \leq \mu_s \|F_n\| \tag{2.15}$$

whereF_t is the tangential force and μ_s a static friction coefficient.

From the onset of contact until particle separation, a spring force is calculated and compared to the above inequality; when it's exceeded, particles are sliding (or slipping) and friction forces are set to the Coulombic limit ($\mu_s \|F_n\|$) itself. Conversely, if the tangential force does not surpass this limit, particles are sticking together.[40] Since frictional forces are overridden by the Coulombic limit when sliding, the spring-dashpot model is only applied when sticking; therefore, viscous damping (which again accounts for particle deformations)[41] is only calculated on timesteps where no slipping occurs.[42]

Differently from normal contacts, it cannot be assumed that tangential interactions occur in a single timestep. The stick-slip model requires that the tangential displacement be calculated over the whole contact period:[34]

$$\bar{\delta_t} = \int_0^t V_t \, \mathrm{d}t \simeq \sum V_t \Delta t \tag{2.16}$$

$$V_t = V_{total} - (V_{total} \cdot \bar{n})\, \bar{n} \tag{2.17}$$

$$where \quad V_{total} = V_{rel} + (\omega \times R)$$

where Δt is the timestep, ω the angular velocity and displacement is now a vector. V_{total} refers to the velocity of a single particle and adds the rotational contribution to velocity by the cross product $(\omega \times R)$, while V_t is the tangential component of total velocity. For a particle-particle collision, V_t is the difference between each particle's individual tangential velocity. Computationally, the shear displacement variable is incremented with each timestep iteration (as in the rightmost side of Equation 2.16), so that displacement "accumulates" over time. This is referred to as a history model of displacement.[43] Figure 2.2 illustrates two particles undergoing the tangential collision model here outlined.

Two models are provided in BlazeDEM: **LinearSpringDash**, a similarly designed counterpart to the normal model of the same name; and **Mindlin**, which uses the (Cattaneo-)Mindlin non-linear formulation for tangential forces based on Hertzian contact theory.[44]

2.2.2.1 LinearSpringDash

A formulation similar to Equation 2.6 in the normal contact model is used here for the spring and dashpot model:[32]

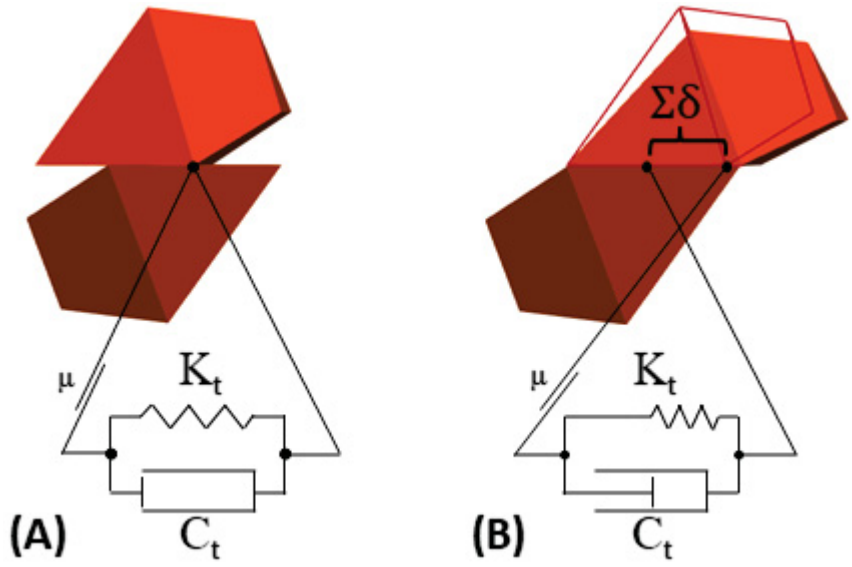

Figure 2.2: Schematic representation of the spring-dashpot model (A) at the onset of tangential contact and (B) in sticking regime, where the accumulated displacement causes an increase in spring loading. As an illustration, the top particle is deformed while sticking, with the red outline showing original dimensions. For simplicity, normal forces and displacements are omitted.

$$F_t = -\left(K_t \bar{\delta}_t + C_t V_t\right) \tag{2.18}$$

A minus sign is included since frictional forces act against movement direction. K_t and C_t are set as the normal force counterparts (Equations 2.7 and 2.8). For every contact timestep, a shear force in the form of Equation 2.18 is calculated and then the Coulomb criterion (Equation 2.15) is checked. If exceeded, F_t is replaced by the Coulombic form itself. Therefore, a general formulation can be expressed as:

$$F_t = -\min\left[\left(K_t \left\|\bar{\delta}_t\right\| + C_t V_t\right),\ \mu_s \left\|F_n\right\|\right] \frac{\bar{\delta}_t}{\left\|\bar{\delta}_t\right\|} \tag{2.19}$$

Multiplication by a normalized shear displacement vector is needed since the Coulombic friction is a scalar. In the case of sticking, the above equation reverts back to Equation 2.18 since both V_t and the $\bar{\delta}_t$ unit vector have the same direction.

2.2.2.2 Mindlin

The Mindlin model was developed under Hertzian contact theory, discussed in the HertzSpring-Dash normal contact model. Hence, the same assumptions and restrictions apply – namely, particles are spherical in nature and form ellipsoidal contact areas, by which non-linearities in tangential forces arise. Therefore, the mathematical formulation is similar and given by:[34]

$$K_t = 8G^* \sqrt{R^* \delta_n} \tag{2.20}$$

$$C_t = 2\sqrt{\frac{5}{6}} \beta \sqrt{K_t m^*} \tag{2.21}$$

where β is given by Equation 2.12 in HertzSpringDash. The tangential spring stiffness is dependant on normal displacement, implying that normal overlap is needed for shear forces to be calculated.[42] Applying the above relations into Equation 2.4:

$$F_t = -\left(8G^*\sqrt{R^*\delta_n}\bar{\delta}_t + 2\sqrt{\frac{5}{6}}\beta\sqrt{K_t m^*}V_t\right) \tag{2.22}$$

Equations 2.16 and 2.17 again apply here for $\bar{\delta}_t$ and V_t, respectively. Only the first half of Equation 2.22 (the elastic spring part) is calculated and compared to the Coulomb criterion (Equation 2.15); this is in contrast to LinearSpringDash, where the sum of both spring and dashpot are used. The right-hand damping term is added only when the spring term does not exceed the Coulombic friction, which again limits the shear force. Equation 2.19 can be restated for Mindlin as:

$$F_t = -\min\left[\left(K_t\left\|\bar{\delta}_t\right\| + \alpha C_t V_t\right),\ \mu_s\left\|F_n\right\|\right]\frac{\bar{\delta}_t}{\left\|\bar{\delta}_t\right\|} \tag{2.23}$$

$$\alpha = \begin{cases} 0 & \text{if } K_t\left\|\bar{\delta}_t\right\| > \mu_s\left\|F_n\right\| \\ 1 & \text{otherwise} \end{cases}$$

2.2.3 Rolling Contact Models

Rolling models are used to calculate forces that oppose the motion of rolling, and are closely related to tangential forces in that they happen on the tangential plane of contact and describe resistance to relative motion.[45] However, rolling resistance in DEM has another prominent role: it serves to model the non-spherical qualities of a given particle, and as such is especially important for rough spheres or real non-spherical particles simulated as spheres.[46]

Much like in the tangential models, a coefficient μ_r is used as a constant inherent to each material pair; this parameter is extensively called a "rolling friction coefficient" in DEM literature.[13,26,47,48] This definition is perhaps imprecise, since the term "friction coefficient" implies a constant of proportionality between normal and rolling forces, and here μ_r is a mathematical device that aims to model non-sphericity – thus, it's a non-physical parameter.[49] In BlazeDEM, μ_r is called coefficient of rolling resistance or rolling damping.

From the definition of rolling resistance, it follows that polyhedra – since their shape itself offers a geometrical resistance to rolling – and perfectly spherical particles do not need rolling damping.[48] Yet, it is recommended that a small value (in the order of 10^{-4} or smaller) be specified to act as numerical dissipation and slightly dampen angular velocities. On the other hand, as an example, cubes simulated as spheres may go as high as 0.10 rotation damping.

Four main models of rolling contact models are usually implemented in DEM codes,[50,51] two of which are in-built in BlazeDEM: **VelocityDamping**, a "Type C" model using an Elasto-Plastic Spring-Dashpot (EPSD) formulation; and **RollingFric**, a "Type A" constant directional torque (CDT) model. For particle-surface contacts, particle torque is always calculated as Type A, independent of model choice.

2.2.3.1 VelocityDamping

Type C, or Elasto-Plastic Spring-Dashpot models conceptualize rolling contacts as virtual springs and dashpots, similarly to the LinearSpringDash tangential contact model. For an angular displacement vector $\bar{\delta_\theta}$:

$$F_r = -K_r \bar{\delta_\theta} \tag{2.24}$$

Note that in defining a rolling force, only a spring term appears: rolling particle deformation is small and generally neglected. When this viscous term is ignored, oscillatory motion (i.e. back-and-forth rolling due to the constant torque reversal) may happen since no rolling energy is dissipated.[50]

This effect occurs when the spring stiffness K_r is modest, so that the oscillations are relatively slow. This implies that the tangential velocity V_t is also small, thus rendering the tangential dissipative terms in Equations 2.18 and 2.22 ineffective in damping motion. By reversing this logic, it becomes evident that a sufficiently large value of K_r foregoes the need for rolling damping, since shear damping becomes substantial enough to stop rolling.[46] Hence, an appropriate definition is given by:[52]

$$K_r = K_t R^{*^2} \tag{2.25}$$

Therefore, like shear damping, K_r is dependant on the tangential stiffness. Rotational displacement is incrementally calculated starting from contact onset and its formulation is analogous to the tangential displacement history models (Equation 2.16). The full Type C displacement is thus given by:

$$\bar{\delta_\theta} = \sum \frac{\omega_{rel}}{\|\omega_{rel}\|} \Delta t \tag{2.26}$$

Rolling is opposed proportionally to the relative rolling velocities of individual particles in contact, calculated as a simple difference in rotational velocities $\omega_{rel} = \omega_A - \omega_B$, which also serves to dampen the rolling oscillation. Finally, a rolling Coulombic limit is imposed on torque:

$$\|F_r\| \leq \mu_r \|F_n\| R^* \tag{2.27}$$

where μ_r is the rolling friction coefficient. The Coulombic limit becomes the acting force whenever it is exceeded:

$$F_r = -\min\left(\left\|K_r \bar{\delta_\theta}\right\|, \mu_r \|F_n\| R^*\right) \frac{K_r \bar{\delta_\theta}}{\left\|K_r \bar{\delta_\theta}\right\|} \tag{2.28}$$

2.2.3.2 RollingFric

In Type A models, a constant, directional torque (CDT) is applied on each particle. For a particle A with angular velocity ω_A:[53]

$$F_r = -\mu_r \|F_n\| R^* \frac{\omega_A}{\|\omega_A\|} \tag{2.29}$$

where the first section of the equation is the Coulomb criterion, given in Equation 2.27. Whereas in the Type C model there is a dependence on angular displacement – and, thus, loading history – here a torque is applied whenever a particle is in contact with another and produces a normal force.

The coefficient of rolling resistance is calculated as the sum of individual particle values, as opposed to the general rule of averaging parameters used in BlazeDEM; in the case of a particle in rolling contact with a surface, then double the maximum value is used instead. When a particle has no velocity but a torque is exerted (e.g. a stationary particle sheared by a surface) Equation 2.29 is adapted by substituting the angular velocity term with an analogous torque τ term:

$$F_r = -\mu_r \, \|F_n\| \, R^* \frac{\tau_A}{\|\tau_A\|} \tag{2.30}$$

2.2.4 Cohesion Contact Models

Attractive forces that provoke the sticking together of matter are a key aspect of granular material science, since cohesion has direct influence in bulk behaviour and flowability in solids. Bridging or arching,[54,55] ratholing,[54,56] unsteady flow,[54,57] as well as erratic behaviour in calibration of solid parameters,[58,59] are some of the problems due to cohesion in solids, particularly under high consolidation stress. While cohesion formally refers to attraction between like particles, the inter-material counterpart adhesion receives the same mathematical treatment in DEM and thus both terms are used interchangeably.

Proposed mechanisms of particulate solid cohesion involve van der Waals, electrostatic and capillary forces, liquid bridging and structural interlocking,[60,61] depending on the presence or not of moisture or liquids in general.[62] Those inter-particulate effects manifest themselves as a general "pull-off" surface energy per unit area – or the energy that needs to be spent in order to separate two bound surfaces.[62]

While adequate at particle-level scales, modelling of cohesion based only on microscopic-range parameters tend to underestimate, or under-represent, cohesive effects on a macroscopic bulk scale, since gravitational effects become dominant. Perhaps more importantly, the effect of consolidation stress are not taken into account,[58,63–65] which has a notable impact on cohesion and general material strength.[66,67] Efforts in bridging this micro-macro transition – accounting for microscopic effects so that a realistic macroscopic behaviour is achieved – involve history-based and elasto-plastic adhesive models that, as in tangential models, calculates forces incrementally through the variation of displacement with time. Examples of such models are the Luding Model,[63] the Edinburgh Elasto-Plastic Adhesive (EEPA) model,[65] and the Macroscopic Elasto-Plastic Adhesive (MEPA) model.[64]

Currently implemented in BlazeDEM is the simplified **JKR** (Johnson-Kendall-Roberts) model and a polyhedral counterpart, **Linear**; the difference is how the area parameter is calculated. The Johnson-Kendall-Roberts formulation of cohesive contacts is based on Hertzian contact mechanics and adds an attractive term to normal forces.[68] It's suitable for large spheres with strong cohesion and small contacts, but has some limitations in modelling bulk behaviour by not accounting for consolidation stress[58] and shear cohesion.[64] The cohesive/adhesive force is given by:[58]

$$F_{adh} = (-A\gamma)\bar{n} \tag{2.31}$$

The negative sign and inclusion of the normal unit vector $\bar{n}$ denote that adhesion acts against normal forces and γ is the surface energy per unit area previously discussed. Depending on model choice, the area term A is calculated as follows:

2.2.4.1 JKR

Since the original Johnson-Kendall-Roberts is based on Hertzian theory, contacts are assumed circular. Therefore, $A = \pi a^2$ and a is the radius of the intersection of two circles, given by:[69]

$$a = \frac{\sqrt{4R_A^2 d^2 - \left(R_B^2 + d^2 - R_B^2\right)^2}}{2d} \tag{2.32}$$

where d is the distance between particle centres. For surface-sphere contacts, a is the radius of a spherical cap:

$$a = \sqrt{h\,(2R - h)} \tag{2.33}$$

and $h = R - d$ is the distance between intersection surface and sphere centre. For polyhedra, these definitions can be problematic since volume, and therefore the "polyhedral radius", may not grow smoothly.

2.2.4.2 Linear

Contact area is approximated by the normal displacement:

$$A = \sqrt{\delta_n} \tag{2.34}$$

This definition may lead to underestimation of cohesion in polyhedra, for example in particles with large faces contacting in a face-face collision but with small displacement. Hence, to better model cohesion in polyhedra, a novel formulation for the attractive force is here used, given by:[70]

$$F_{Adh} \approx \sqrt{\delta_n} K_n \gamma_N \tag{2.35}$$

where the subscript N in the cohesion parameter γ denotes it is a numerical parameter, similarly to rolling friction in spheres. As discussed in Section 2.2.4, this approach allows for easier calibration by avoiding a hard-to-define strict physical parameter. This attractive force acts only in the normal direction.

2.3 DEM CALIBRATION

The general aim of calibration is to obtain a set of parameters that, when used in a DEM simulation, yield realistic results and can be used to predict particle behavior in multi-particle simulations. To this end, a set of experiments are performed in the laboratory and then simulated in DEM; since there is no reliable, straightforward correlation between experimental results and the parameters we wish to obtain, they are estimated by being systematically guessed until real and virtual experiments match.[71]

A description of each experiment proposed is provided in section 3. In general, the experiments provide the static and dynamic angles of repose (AoR) of a given material – the steepest slope, measured from the horizontal plane, that the unconfined material can maintain without devolving into motion.[72] These angles are dependent on the static friction coefficient and, in the case of spherical simulations, on rolling friction, between particles themselves and between particles and walls.[73] Therefore, if the angles of repose seen in the simulations closely match those obtained from the experiments, then the guessed friction coefficients are good representations of the real interactions.

Due to its relationship to flowability in solids, the angle of repose is also interesting as a classification of cohesiveness in granular media. The Carr classification,[74] given in Table 2.1, describes ease of flow as ranges of AoR:

Angle of Repose	Description
< 30^o	Very Free-Flowing
30^o to 38^o	Free-Flowing
38^o to 45^o	Fair to Passable Flow
45^o to 55^o	Cohesive
> 55^o	Very Cohesive

Table 2.1: Carr classification of powdered solids flowability. Increased cohesive strengths restrain particle movement, thus causing an increase in repose angles. Adapted from Al-Hashemi (2018).[73]

The process of calibration for a single experiment is ambiguous, since typically a range of possible friction values is found.[71] For this reason, multiple experiments must be run and calibrated for a single material, so that a unique set of parameters that truly capture bulk behaviour can be obtained.[67] Since BlazeDEM supports the simulation of polyhedral particles – which, as discussed in section 2.2.3, forego the need for a rolling friction coefficient –, calibration is simplified to finding the static friction coefficients that satisfy experimental results. For the purpose of comparing polyhedral and spherical solutions, the result found from the polyhedral case are then used to calibrate a rolling friction coefficient for the spherical case.

3 MATERIALS AND METHODS

Two powdered materials, one free-flowing and another that displays mild cohesion, were used in the following experiments. The first granular solid, with an assumed average size of 0.6 mm and cubic shape, was calibrated in Part I. The second material – henceforth referred to as "cohesive powder" – was calibrated in part II, with an assumed average size of 0.35 mm and also modelled as a cube. Microscope images were used as the basis for particle shape choice, as it was observed that both materials were made up of cube-like particles.

Scaling of particles was done based on the equivalent-sphere approach: the dimensions were changed by the software so that – for instance, on 10x scaling for the free-flowing material – the cube volume was equivalent to the volume of a sphere of diameter 6 mm. In practical terms, it means that the starting 0.6 mm average size is not necessarily the length of the cube sides or any other of its dimensions.

3.1 EXPERIMENTS

Four experiments were performed with the objective of recording either static or dynamic angles of repose. All four are related to one or more of four friction coefficients (μ) - static and rolling coefficients, in particle-particle and particle-wall interactions. The following test protocols were taken from previous work in DEM calibration of the angle of repose.[48]

3.1.1 Rotating Drum

A stainless-steel cylinder (4.8 cm diameter, 2.5 cm depth), closed by a glass cover, was filled with solids so that they occupied between 20% to 40% of its volumetric capacity. Then, it was mounted to a horizontal motor and rotated at constant speeds ranging from 10 to 50 RPM, at increments of 10 RPM per run; speeds were adjusted using an Arduino-controlled Hall effect sensor. For each run, a video showing the particle flow was recorded. These videos were post-processed on a frame-by-frame basis, using a Canny edge detection algorithm written in Python to isolate solid edges, and a linear regression performed on the edge points estimates the dynamic angle of repose. Since the regression is performed over each frame, an Angle versus frame graph is obtained, presenting a mathematical representation of flow behaviour over time. [†]

For certain rotational speeds, material flow reaches the “cascading regime”, in which the angle of repose is not continuous, but split in two (upper and lower) regions (Figure 3.1). A convenient way to characterize and compare flow regimes is the Froude number, which is the ratio between centrifugal and gravitational forces. For a rotating drum, it is given by:[75]

$$Fr = \frac{\omega^2 R}{g} \tag{3.1}$$

3.1.2 Heap Test

An open-ended cylinder (3 cm diameter, 5 cm height) was rested on a stainless-steel surface and filled with solids to about 50% of its volume. The cylinder was then pulled by and Arduino-controlled step motor at a constant speed of 3 mm/s, and the material was allowed to flow out of

[†]Code written by Prof. Dr. Éliton Fontana, from the Chemical Engineering department at UFPR

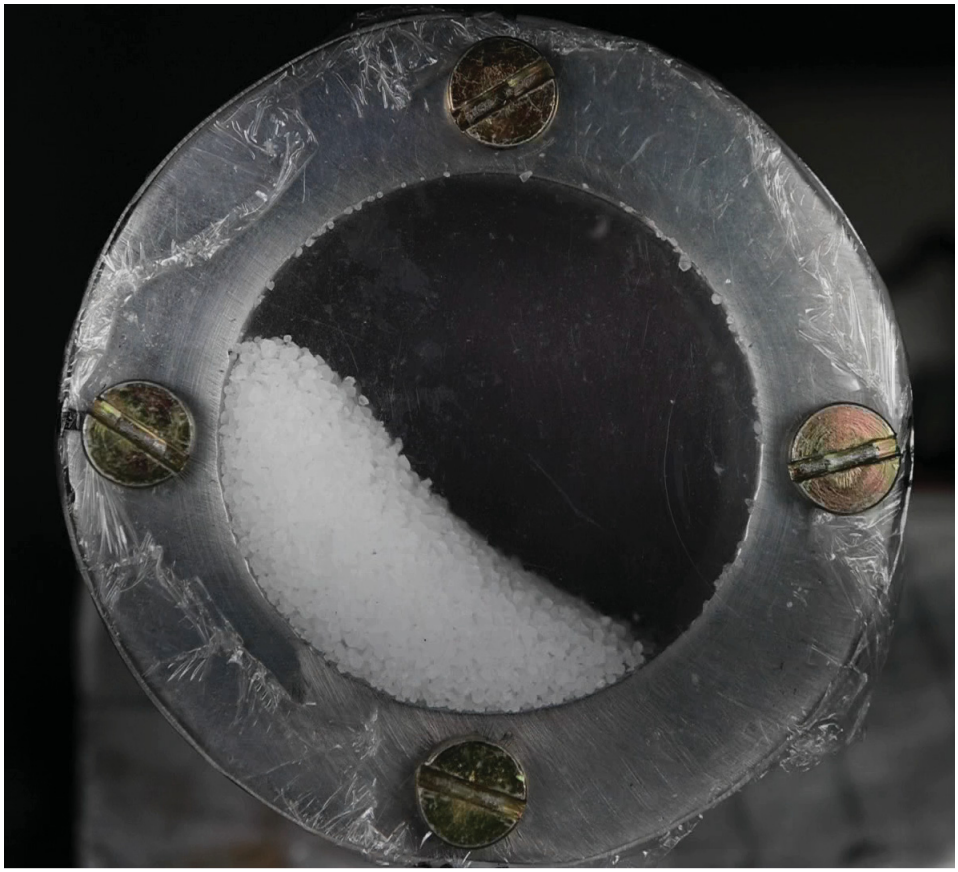

Figure 3.1: Snapshot of the rotating drum, filled with material, running at 40 RPM; the cascading regime can be observed, since the material does not form a continuous angle of repose. Plastic wrap placed underneath the glass cover prevents material from clinging.

the bottom opening and form a conical pile. Figure 3.2 shows the experimental setup, composed by three 3D-printed pieces in brown PLA: a cylinder and two support walls with rails. A metallic shaft goes through the cylinder and the rails, in a manner that the pulling motion was restricted to the vertical direction. Images of the final pile were recorded and the inclination of the left and right cone sides is the static angle of repose. This test is useful in defining material cohesiveness by the Carr classification (Table 2.1).

3.1.3 Ledge Test

Also called slump test, the ledge test is a test that can be performed using a hopper, such as the one shown in Figure 4.1. The lateral face is simply lifted upwards when the hopper has been filled to 50% of its volume, and the angle formed by the out-flowing particles is measured. To reduce the amount of solid needed to run the experiment (and the computational costs in the DEM simulations), the hopper was made as a 3 cm cube, 3D-printed using Polylactic Acid (PLA).

3.2 SIMULATIONS

BlazeDEM, a modular and high-performance GPU-based DEM code is the software employed for simulating. For all simulations, the Hertz-Mindlin model with RVelDamping for rolling resistance is used. The time step is half the critical value and adjusted for each particle size. Table 3.1 summarizes the relationships between scaling, particle size and time steps for the free-flowing

powder. For the cohesive material, a different approach to time-step choice is presented and discussed in Part II.

Scaling	Particle Size (mm)	Particle Volume (cm³)	Critical Time Step	Time Step
1x	0.6	1.13E-4	5.6E-6	2.8E-6
5x	3.0	1.41E-2	2.8E-5	1.4E-5
10x	6.0	0.113	5.6E-5	2.8E-5
20x	12.0	0.905	1.1E-4	5.5E-5
30x	18.0	3.05	1.7E-4	8.4E-5
40x	24.0	7.24	2.3E-4	1.1E-4

Table 3.1: Scaling factors and particle dimensions for the free-flowing material. Critical time steps, calculated by BlazeDEM, were used as basis for time step choice.

A particle size distribution centered around the particle sizes in Table 3.1 was assumed, to better represent the real powder. Particles with ±10% volume were added to all simulations under a normal distribution, assuming that ±10% is one standard deviation away from the mean; hence, 68.26% of all particles have the volumes in the table above, and the rest is split between the added particles.

Five materials were utilized throughout the experiments, three of which are "wall" materials: stainless steel, PolyLactic Acid (PLA, a polymer used in 3D printing) and glass. Table 3.2 summarizes material properties used in simulations. Apart from densities (which is coincidentally equal for both free-flowing and cohesive matrials, and thus listed as a single value), all properties were assumed; the Young's modulus, in particular, is set as a relatively low value, since it allows for higher time steps without compromising simulation results.[76]

	Powders	Stainless Steel	PLA	Glass
Density (g/cm³)	1667	7850	1270	2500
Young's Modulus (GPa)	1E8	2E9	1E8	1E8
Poisson's Coefficient	0.25	0.27	0.33	0.2
Coefficient of Restitution	0.50	0.65	0.50	0.50

Table 3.2: Material properties for simulations.

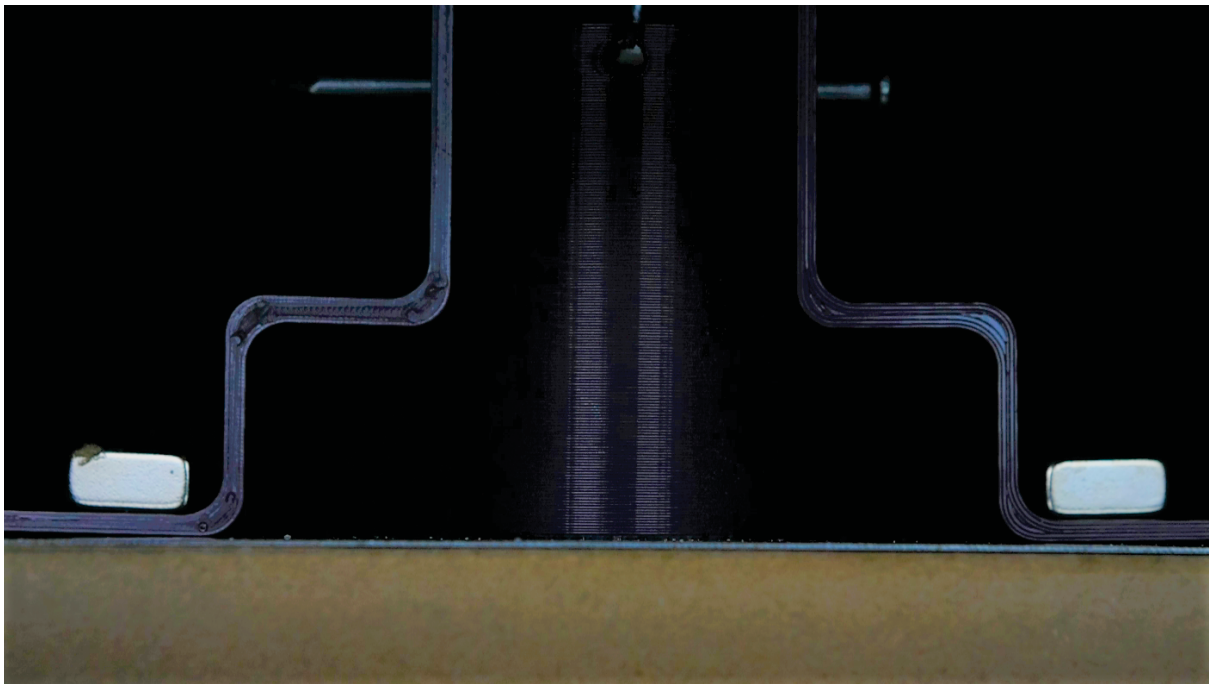

Figure 3.2: 3D-printed experimental apparatus for the heap test. The cylinder is pulled by an Arduino-controlled step motor at a constant speed, while the walls on both side prevent sideways motion.

4 PART I - CALIBRATION OF A FREE-FLOWING POWDERED MATERIAL

Three experiments were performed with the powdered solid, but not all were included here, or simulated, for calibration. Ambiguity in calibration mostly comes from having two friction coefficients (static and rolling) each in particle-particle and particle-wall forms, thus having four parameters to be adjusted. Since real-shaped, polyhedral particles do not need added rolling damping (Section 2.2.3), the problem is reduced to finding particle-particle and particle-wall static friction coefficients that reproduce bulk behaviour; hence, less experiments need to be simulated for an accurate calibration.

Two AoR experiments, the ledge test and rotating drum (10 and 20 RPM), were chosen because the former is the least computationally expensive and the latter is the only dynamic AoR experiment. Only two rotating speeds were used since the cascading regime at higher speeds is not reliably measurable with upscaled particles.

4.1 EXPERIMENTAL RESULTS

4.1.1 Ledge Test

Ledge test assays were run in triplicate, and their angles measured by importing still images into an image-editing software (GIMP, Version 2.10.24), which has an in-built measurement tool. The ledge test equipment consists of the hopper and a movable hatch, both printed separately. During printing, the geometry face that touches the printer's heated bed tends to have a smooth, glass-like finish, since it was in contact with a surface above its glass-transition temperature. To reduce shear effects when pulling the hatch, this face was always directed towards the hopper and material.

Figure 4.1 presents sequential snapshots of the ledge test being performed. As the hatch is lifted, particles tumble out of the hopper and come to a rest, forming the AoR shown in (C); it is then measured as in (D). The average AoR was 21.33 degrees, with a standard deviation of 0.4 degrees.

4.1.2 Rotating Drum

A single sample of the material was run continuously on the rotating drum. 10-second videos were recorded for each rotational speed (10 to 50 RPM), which were adjusted using an Arduino-controlled Hall effect sensor.

Figure 4.2 exemplifies the post-processing done for each video: first, a computer software (Kdenlive, Version 21.04.1) is used to increase contrast between white particles and the dark background (B); then, each video is split into frames and a Python algorithm performs a Canny edge detection over each frame (C), transforming the images into matrices of 1 (for white, detected edge pixels) and 0 (for dark, non-edge pixels). Finally, a linear regression over each matrix calculates the dynamic angle of repose, taken to be the angular coefficient of the regression.

The above process is run sequentially over the range of all frames, generating Figure 4.3. Average angles for 10 RPM in (A) and 20 RPM in (B) were calculated as 37.0 and 35.4 degrees, respectively. The primary driver of the formation of AoRs in rotating drum experiments is the lifting of particles due to particle-wall friction, which should increase in magnitude as the speed increases. Hence, higher angles of repose are expected for higher speeds, which is contrary to

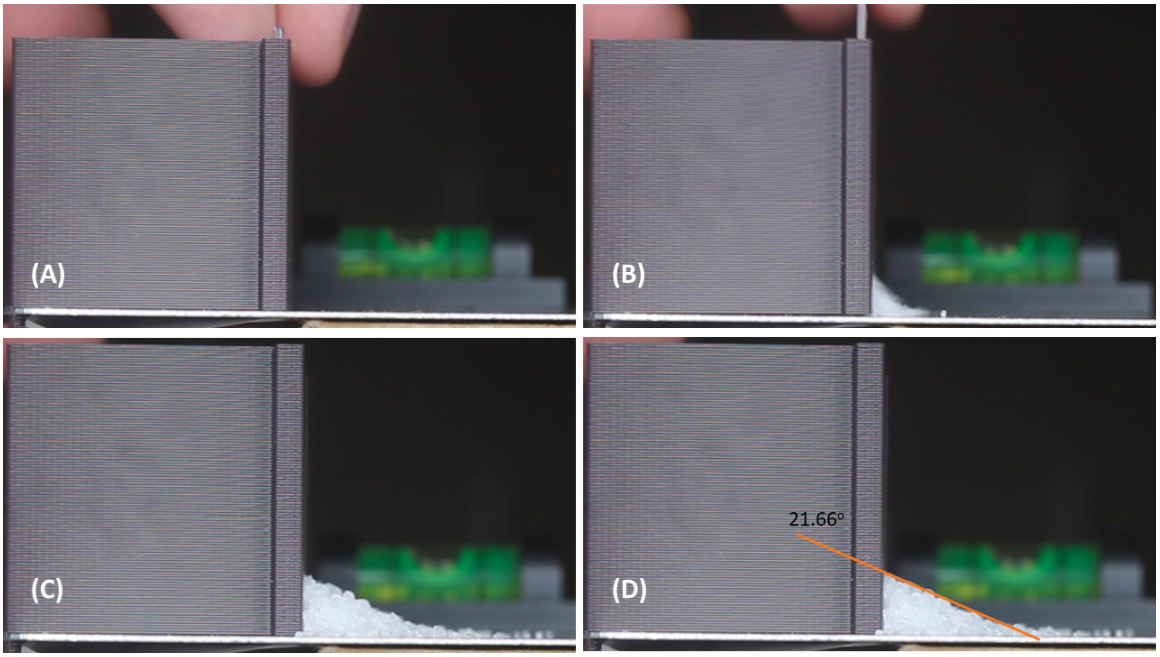

Figure 4.1: Sequential images of a ledge test run, (A) before (B) during and (C) after upwards pulling of the hatch, where the Angle of Repose is shown. In (D), the orange line is used to measure the angle (annotated in black).

the results here shown. This is most likely an "artifact" of the video-treatment procedure, and for the purposes of calibration it is assumed that both 10 and 20 RPM have a similar angle.

4.2 SIMULATION RESULTS

4.2.1 Calibration

Instead of following the natural course of simulating at real (1x) scale, calibration is done at 30x scale for the considerably higher speeds. Since calibration is done by trial-and-error, many runs of the same simulations must be done, and every erroneous trial greatly compounds the overall length of time to achieve a proper set of parameters. Hence, it is assumed that repose angles are, in fact, invariant with size – or, in other words, that CGM is valid – and then worked backwards toward the real scale.

Figure 4.4 is an example of the calibration procedure for polyhedra, wherein the end of some ledge test simulations (at 30x scaling) are shown. As a first attempt, in (A), both the particle-particle and particle-wall friction coefficients were set to 0.1; due to the low force resistance from the small coefficients, particles are allowed to sprawl forward and a low AoR is achieved. Since a much higher AoR is needed, a new value of 0.5 is then guessed in (B), where high friction forces prevent much outflow of material and the AoR is high. It becomes evident that one possible answer lies between the two previous attempts, so in (C) a particle-particle and particle-wall friction coefficients of 0.3 and 0.2, respectively, were now used. The measured AoR of 19.09 is slightly below the target value of 21.33, so a further adjustment of parameters is needed in (D). Finally, with particle-particle and particle-wall frictions at 0.35 and 0.25, an AoR of 21.38 is found, which is close to the experimental target.

The same set of parameters was then used to simulate both speeds of the rotating drum and fine-tune the friction coefficient between particles and stainless steel. To keep consistency between angle measurement procedures, the same Python script used for the experimental results was used for simulations, by using Paraview to transform the simulation files into black and

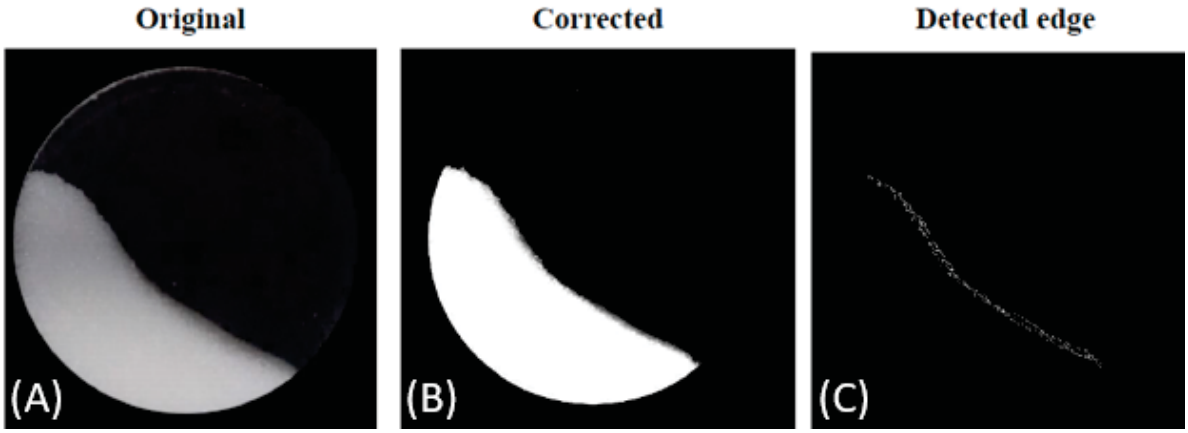

Figure 4.2: Example of a Rotating Drum video post-processing. (A) Original unchanged image; (B) first image with altered curves to increase black-and-white contrast; (C) canny edge detection of the previous image.

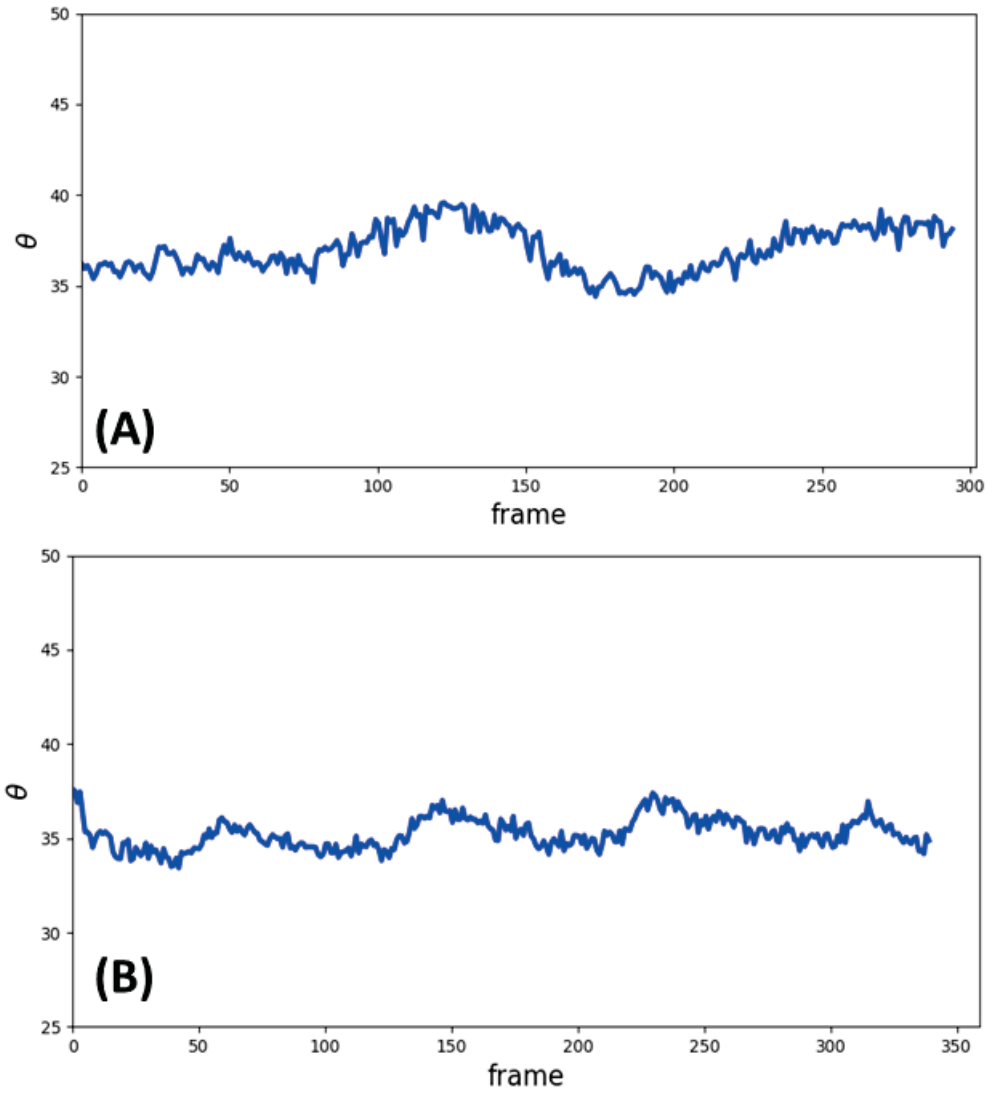

Figure 4.3: Angle *versus* frame graphs, resulting from the procedure shown in Figure 4.2, for the powdered material at (A) 10 and (B) 20 RPM.

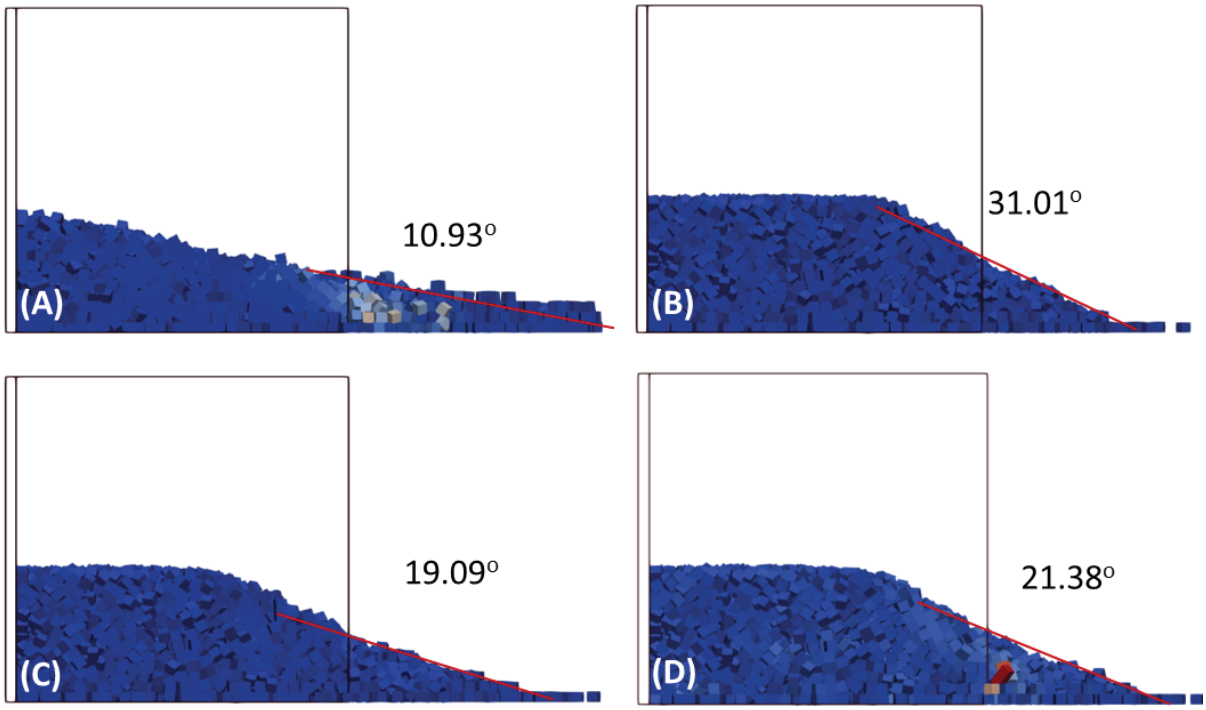

Figure 4.4: An illustration of the iterative process of calibration at 30x scaling, in which friction coefficients were systematically altered in successive runs of a ledge test simulation. The set of parameters in (D) generate an angle of repose very similar to that seen in experiments.

white images. Hence, edges were computed by the same algorithm, and a similar angles *versus* frame graph was generated and compared. In the case that average angles in any speed did not match, new parameters were tested and rerun on the ledge test as well, until all simulations were consistent with experiments.

Finally, for calibrating the rolling friction coefficient in spherical cases, the same procedure is undertaken while keeping static friction coefficients fixed. If no rolling damping paired with the above static friction coefficients is able to reproduce experimental AoRs, the calibration procedure is restarted. In the following discussion, a rolling damping coefficient of 0.09 was calibrated for spheres.

4.2.2 Ledge Test

The result shown in Figure 4.4D is a successful calibration of a ledge test at 30x scaling, since there is good agreement between simulated and experimental results. However, for the obtained set of parameters to be relevant for general use, they must match in the real-scale simulation of the ledge test.

When up-scaling particles, it is important to maintain a big enough ratio between characteristic lengths of the experimental apparatus and particle size; as previously discussed in Section 2.1.2, this ratio is usually 25, but here the target ratio is set at 30. If particle scaling causes the ratio to drop below the target value, then the ledge test box mesh is also up-scaled. Table 4.1 shows the scaling applied to both particles and mesh, as well as the ratio that it produces, on (polyhedral / spherical) simulations. The characteristic length is technically the side length – or the side of the box in view in the experimental and simulated videos – but since the experimental device is cube-shaped, it's the depth and height as well.

At 1x scaling, both particle and box sizes match the experimental dimensions. As particle size increases, the ratio tends to the minimum value, which also minimizes the number of

Particle Scaling	Box Scaling	Particle Size (mm)	Charact. Length (cm)	Ratio
1x	1x	0.5 / 0.6	3	62.05 / 50.01
5x	3x	2.4 / 3.0	9	37.25 / 30.03
10x	5x / 6x	4.8 / 6.0	15 / 18	31.02 / 30.00
20x	10x / 12x	9.7 / 12.0	30 / 36	31.01 / 29.99
30x	15x / 18x	14.5 / 18.0	45 / 54	31.03 / 30.01
40x	20x / 24x	19.3 / 24.0	60 / 72	31.02 / 30.00

Table 4.1: Particle and Ledge Test box scaling, for polyhedral and spherical simulations, with respective sizes separated by a slash. The ratios of characteristic ledge test length and particle size, which is limited at a value of 30 or more, are also listed.

particles – from 10x particle scale and above, the number of simulated particles is approximately the same, and the differences in simulation speed mainly come from the time step. Particle size in Table 4.1 refers to the characteristic length of particle geometries (cube side length in polyhedra, diameter in spheres) which explains why polyhedral particles are listed with smaller sizes, since they were resized based on the equivalent volume sphere.

Figure 4.5 shows the angles of repose measured for each simulation, with experimental results added for comparison and black and gray dotted lines representing one and two standard deviations, respectively, of the experimental measurements. Simulated results were generally close or inside the two standard deviations mark; some variation in measurements is admitted when applying a coarse grain modelling of particles, so that scales from 1x to 30x can be considered matching. Moreover, the act of manually measuring angles is subject to some added variability.

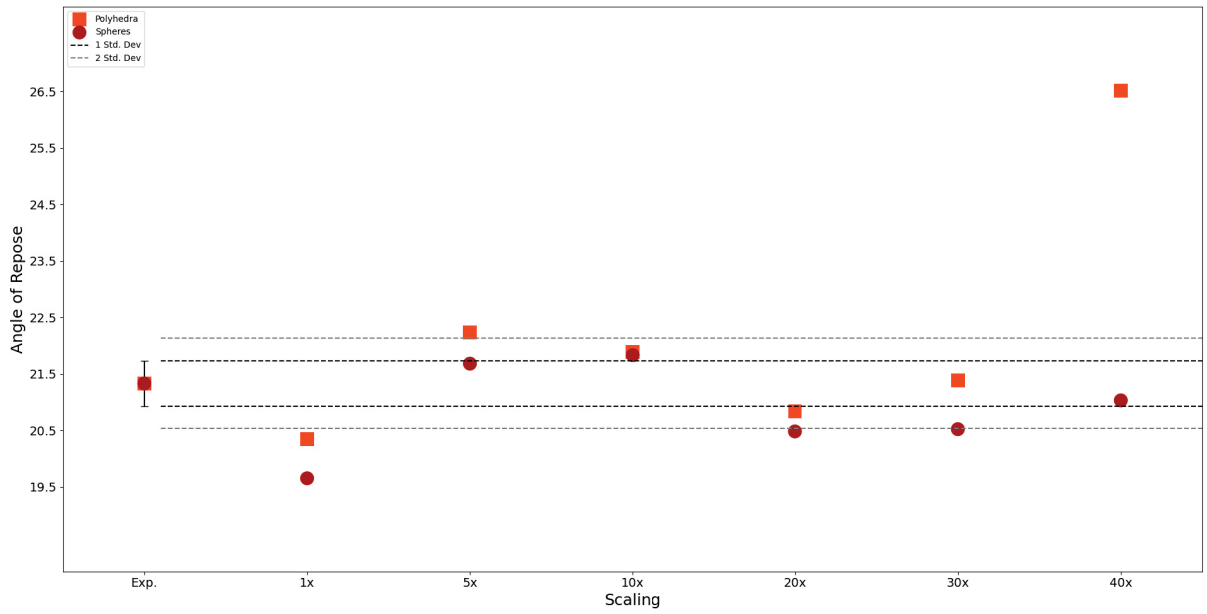

Figure 4.5: Experimental and simulated results for the ledge test using both polyhedra (square, orange) and spheres (circles, red). Dotted lines represent standard deviations from experimental results.

Three points in particular merit some discussion: both polyhedral and spherical simulations at 1x scale and the polyhedral simulation at 40x scaling. In taking a CGM approach to calibration, individual particles can be thought of as being grouped, or packed, into larger and more compact grains. This compactness, in turn, means that on up-scaled simulations particles have less freedom to spread out from the ledge test box, creating a less defined angle of repose.

Figure 4.6 presents measurements of AoR in 1x and 30x scale showing this effect, which impacts AoR measurements since the "tail end" of the pile was ignored in measuring experimental angles, and thus ignored in simulations as well. Since the "tail" is the result of particle spread, the frame-of-reference for angle measuring in up-scaled simulations is skewed. The same is valid for spherical simulations; yet, the deviation here discussed is only one degree from the 30x (calibrating) scale, small enough to be ignored.

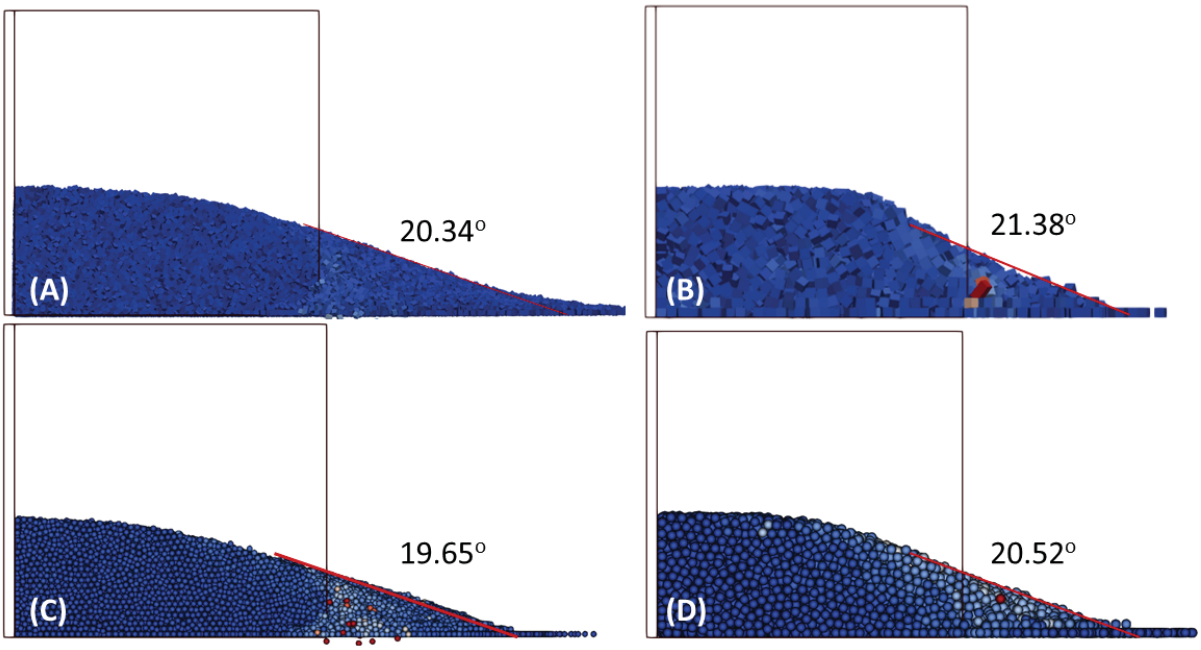

Figure 4.6: Simulation results, and AoR measurement, of the ledge test at (A, C) 1x and (B, D) 30x scaling for polyhedra and spheres respectively. At bigger scales such as in (B), where particle number is reduced, the "tail-end" of the pile is not present as in (A), leading to differences in the frame-of-reference of measurements.

The polyhedral 40x scale result is approximately five degrees higher than its 30x counterpart, suggesting a limit as to how much up-scaling can be applied in CGM. Table 4.1 shows that the characteristic length ratio at 40x is the same as in 30x, 20x and 10x scales – the number of particles is therefore approximately the same – suggesting that the nature of the error is unrelated to scaling *per se*. In Table 3.1, where time steps as related to scaling are presented, it is shown that half of the critical time step – the criterion here adopted for setting time steps – for 40x scaling is 1.1E-4, which is high in terms of DEM; this leads to poor calculation accuracy, which might explain the results here shown.

Figure 4.7 tests this hypothesis by comparing the original 40x simulation (A) against the same simulation run on a 5.5E-5 time step (B). The AoR is minimally influenced by the time step, although there is some difference in particle arrangement. One possibility is that, at this scale, particle mass is big enough that, together with the geometric stability of cubes, gravity has a diminished influence on bulk behaviour and particles remain mostly stationary. Spherical 40x simulations, however, give a similar result to other scales. Particle mass is equal in polyhedral and spherical cases for the same scaling, but spheres have only artificial geometric stability due to rolling damping; hence, gravity is still able to act in moving spheres better than in the polyhedral case. This is evidence that simulating polyhedra-as-sphere using rolling friction can miss bulk behaviour effects due to shape. [¶]

[¶]In Appendix A, a more thorough discussion on the different effects of mass on polyhedral and spherical simulations (a recurring theme throughout this work) is provided.

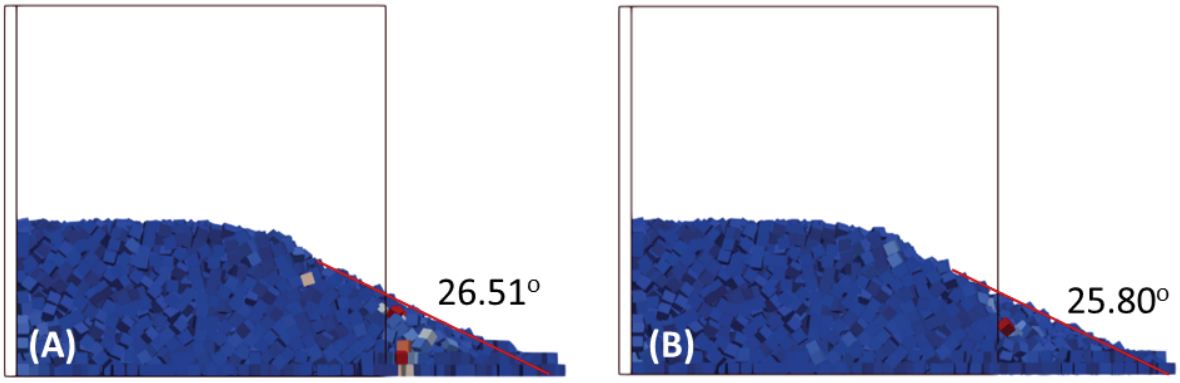

Figure 4.7: Simulation results and angle of repose measurement of the 40x scaling ledge test at (A) 1.1E-4 and (B) 5.5E-5 time step, showing little influence on AoR.

Table 4.2 presents number of particles and total running time, as measured by process execution time in Bash, for each run of the ledge test simulations (simulation time of 2 seconds). A slash again separates polyhedral and spherical cases.

There is an 8.7x reduction in particle number (and doubling of time step) from polyhedral 1x to 5x scale, but running time is cut by a factor of 35. At larger particle counts, GPU threads and cores tend to be fully "saturated", meaning that for each time step particle calculations do not run in total parallelism. With reductions in particle numbers due to CGM, GPU utilization is better distributed, explaining why from 10x onward running times decrease proportionally to time step increases.

Particle Scaling	Time Step	Number of Particles	Total Running Time (s)
1x	2.8E-6	131,830 / 55,454	23,639 / 926
5x	1.4E-5	15,932 / 11,994	675 / 151
10x	2.8E-5	8,255 / 12,224	250 / 76
20x	5.5E-5	7,658 / 12,383	127 / 34
30x	8.4E-5	7,640 / 11,961	84 / 25
40x	1.1E-4	7,424 / 12,085	72 / 21

Table 4.2: Number of particles and simulation times, and how they relate to particle scaling and choice of time step, for the ledge test.

4.2.3 Rotating Drum

Figure 4.8 is a post-processing example for the 30x scaling used in calibration, which generated the graphs show in Figure 4.9 for 10 and 20 RPM.

The rotating drum process is analogous to the ledge test, with the caveat that average angles were measured and compared instead of a single, still image. Table 4.3 presents the scaling rules and *criteria*, where the characteristic length now is the drum diameter. Since it is bigger than the ledge test box length (4.8 cm and 3 cm, respectively), it allows for less aggressive scaling. Most of the preceding discussion with regards to particle number and its relation to ratio applies here.

As in the ledge test, Figures 4.10 and 4.11 provide comparisons between experimental and simulated results for the rotating drum at 10 and 20 RPM,[§] respectively, where black and

[§]Perhaps erroneously, "true" 10 and 20 RPMs were used here; Part II provides a better discussion of this approach *versus* reescaling to match Froude numbers.

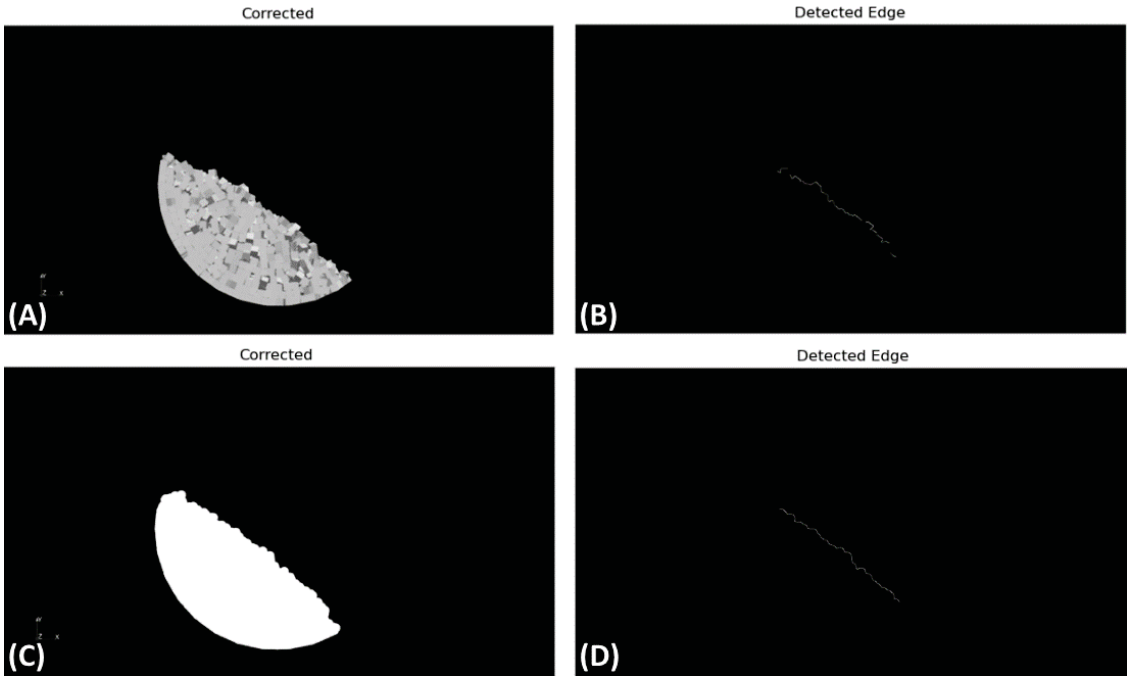

Figure 4.8: Example of a rotating drum simulation post-processing for polyhedra (A, B) and spheres (C, D) at 30x scaling. The .VTK files generated by simulations is imported to Paraview (A, C) and run through the same Python script used for experimental results, generating Canny edges (B, D).

Particle Scaling	Drum Scaling	Part. Size (mm)	Charact. Length (cm)	Ratio
1x	1x	0.5 / 0.6	4.8	99.28 / 80.02
5x	2x	2.4 / 3.0	9.6	39.73 / 32.03
10x	3x / 4x	4.8 / 6.0	14.4 / 19.2	29.78 / 32.01
20x	6x / 8x	9.7 / 12.0	28.8 / 38.4	29.77 / 32.00
30x	10x / 12x	14.5 / 18.0	48.0 / 57.6	33.09 / 32.01
40x	13x / 16x	19.3 / 24.0	62.4 / 76.8	32.26 / 32.00

Table 4.3: Particle and rotating drum scaling, for polyhedral and spherical simulations, with respective sizes separated by a slash. The ratios of characteristic rotating drum test length and particle size, which is limited at a value of 30 or more, are also listed.

gray dotted lines again represent one and two standard deviations of the experimental results. While up-scaled results were in good agreement with experimental measurements, there was a noticeable drop at scales below 10x, with real-scale polyhedra having an angle of repose of 23.51 degrees at 10 RPM and 33.06 degrees at 20 RPM.

The explanation can again be possibly attributed to the individual weight of particles. At smaller scales and lighter particles, the drum's rotational speed is better able to provoke motion, creating a more intense rearrangement of particles. Since they are cube shaped, there is more impacting and interlocking of geometric irregularities, creating a "geometric friction" between particles that prevent them from being pulled by the drum's wall. This observation is supported by the spherical results, where angles were mostly size invariant, and by Figure 4.12, which shows average velocities as functions of time on 1x and 30x scaling. After stabilization (t = 4s), the average velocity at the smaller scale is 2- to 3-times that of the 30x scale.

Up-scaling geometries by the same factor as particles can further verify this hypothesis, since geometric similarity is maintained. Hence, a simulation of 30x particles with 30x drum scaling was performed, and the resulting angle of 38.3 (Std. Dev. 4.8) suggests there are intrinsic

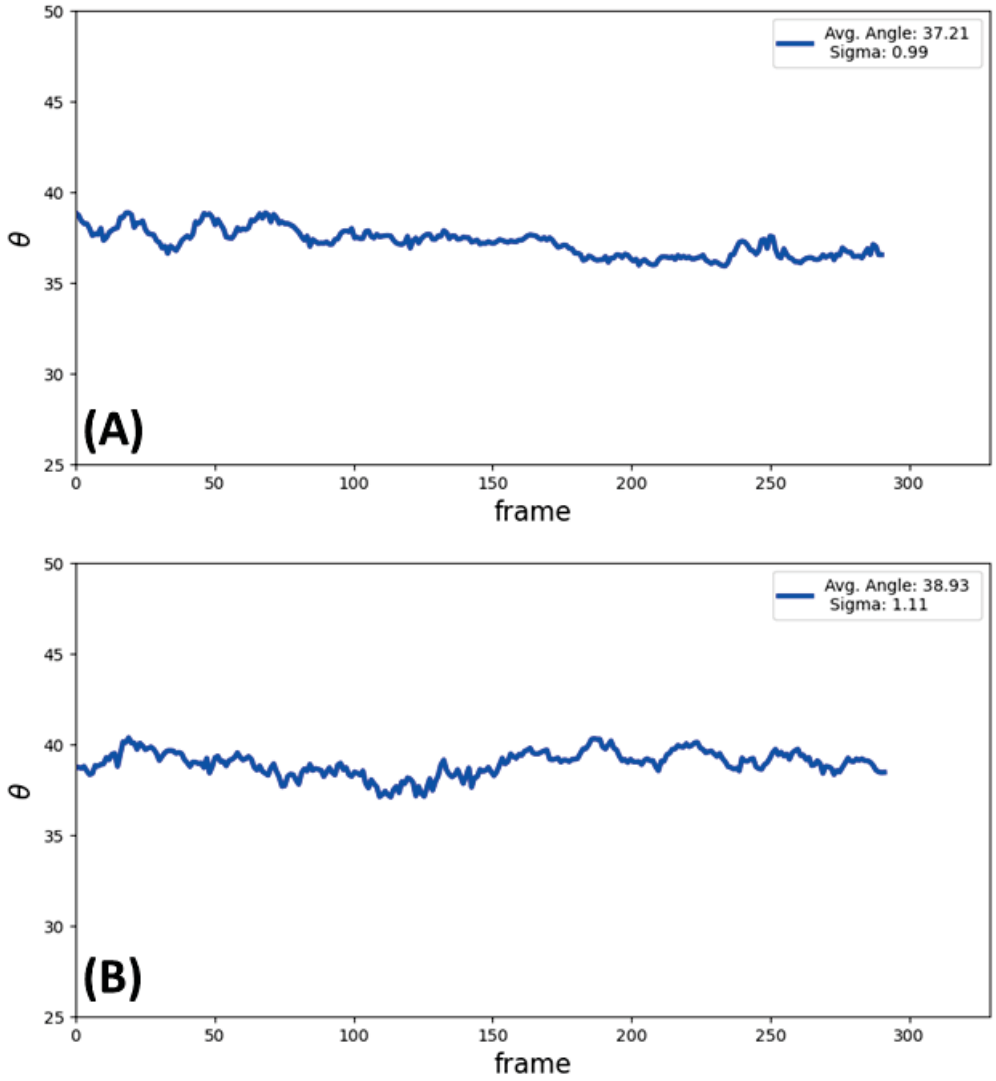

Figure 4.9: Angle *versus* frame graphs, resulting from the procedure shown in Figure 4.8, for the 30x scale simulations at (A) 10 and (B) 20 RPM.

differences between particle scales. Furthermore, the high standard deviation is caused by the increased angular velocity at the drum borders, since the diameter is increased.

To better evaluate the influence of drum angular velocity, it is convenient to use the dimensionless Froude number (Equation 3.1), which is the ratio between centrifugal and gravitational forces. Angular velocity and gravity are, here, constant values; the only variable across scales is the radius R, which is given by $R = f_{CGM}R_{1x}$. Froude numbers increase as scales increase, suggesting that direct scale-up of dynamic simulations impacts flow regimes and can alter angles of repose. Calculated Fr numbers for the 1x and 30x scales are, respectively, $6.8E^{-}5$ and $6.8E-4$, a 10-factor increase precisely because geometric scaling in the 30x simulations was 10. As a final test, the same 30x scale simulation was re-run with a velocity of 3.16 RPM, which then matches Froude numbers with the real-scale simulation. Again, a result of 36.67 (Std. Dev. 0.74) gives credence to the notion that is particle mass, together with interlocking, that distorts the up-scaling of dynamic calibrations.

The polyhedral 40x scale result at 20 RPM, of 40.51 degrees, is the highest AoR observed and, in fact, is the end of an upward trend on polyhedral 20 RPM simulations. Gravity and geometric stability, as in the ledge test, play a key role here. Since rotating speed is higher

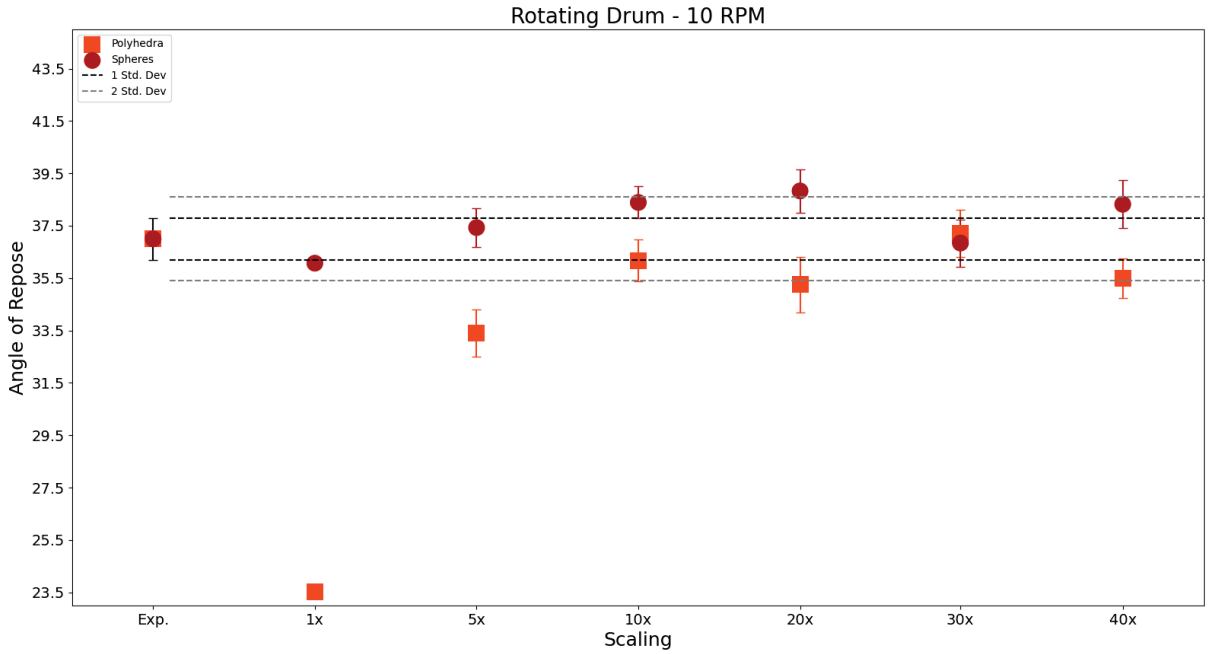

Figure 4.10: Experimental and simulated results for the rotating drum, at 10 RPM, using both polyhedra (square, orange) and spheres (circles, red). Dotted lines represent standard deviations from experimental results.

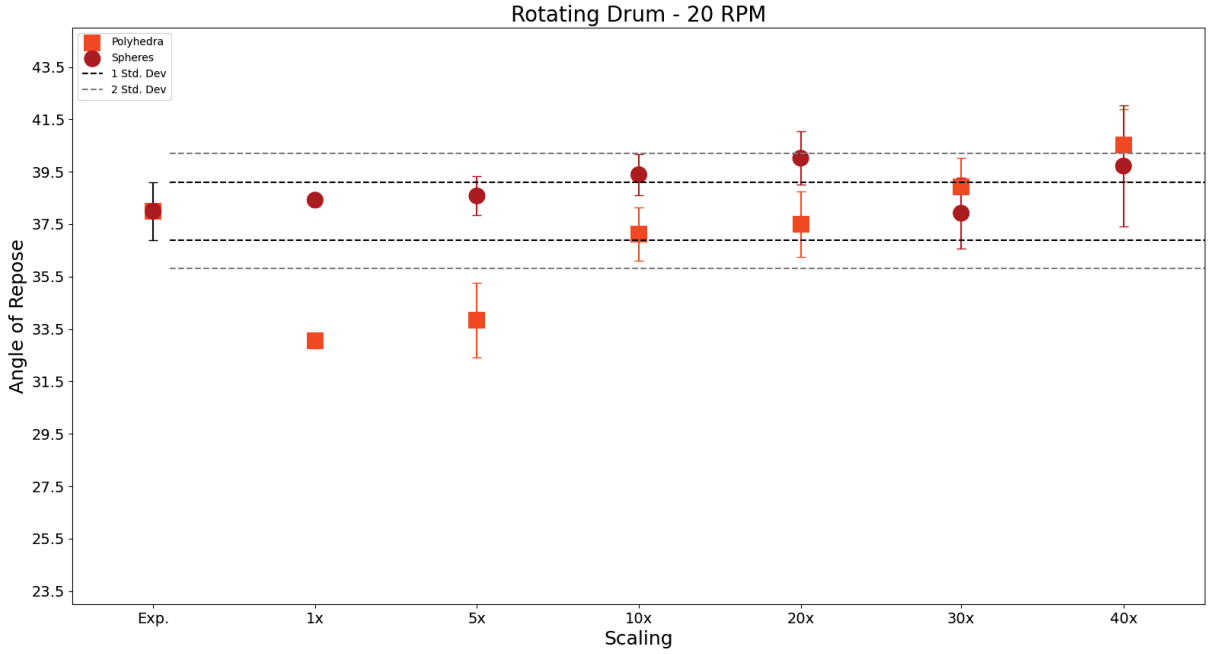

Figure 4.11: Experimental and simulated results for the rotating drum, at 20 RPM, using both polyhedra (square, orange) and spheres (circles, red). Dotted lines represent standard deviations from experimental results.

than in the 10 RPM simulations, the total shear force exerted by the walls on the particles is increased, hence carrying them higher. With increasing masses, the gravitational force is less effective in pulling particles down, so that they fall from a higher point and create a bigger AoR. Spherical simulations again support this hypothesis, since there is a general upward trend with spheres, but less pronounced due to not having the geometrical stability of cubes. [¶]

[¶]In Appendix A, a more thorough discussion on the different effects of mass on polyhedral and spherical simulations is provided.

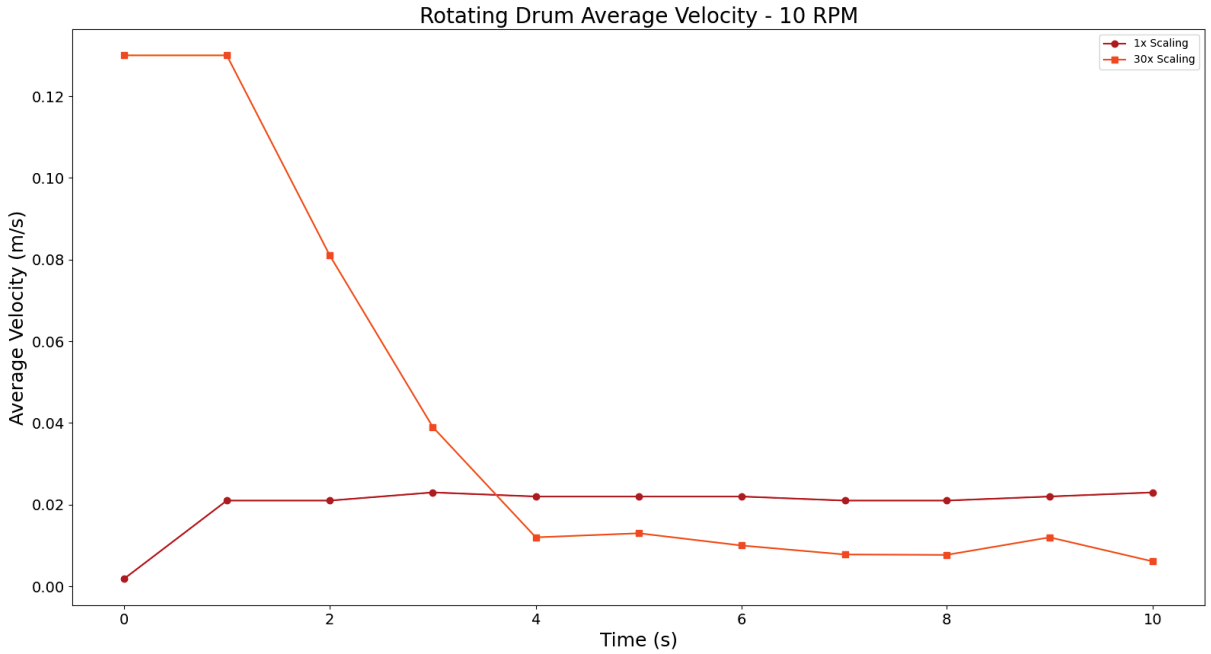

Figure 4.12: Average velocities for particles simulated at 1x (red) and 30x (orange) scale. Velocities drop with increasing particle sizes, a phenomenon which might explain increased AoRs with increased scaling.

Table 4.4 presents number of particles and total running time for rotating drum simulations (simulation time of 12 seconds). Notably, at 1x scaling polyhedral running times were nearly 43 hours. Polyhedral simulations were run 66x and 461x faster, when compared to real-scale, for 5x and 30x scales respectively, a sizeable increase in performance due to the reduction of particle count. Characteristic length ratio was here reduced by approximately three times, while in the ledge test it was reduced by a factor of two, explaining the apparent difference in relative speed-up.

Particle Scaling	Time Step	Number of Particles	Total Running Time (s)
1x	2.8E-6	167,330 / 71,666	154,888 / 6,903
5x	1.4E-5	4,923 / 4,466	2,328 / 657
10x	2.8E-5	2,215 / 4,631	1,365 / 331
20x	5.5E-5	2,151 / 4,770	585 / 167
30x	8.4E-5	2,958 / 4,415	336 / 95
40x	1.1E-4	2,700 / 4,703	254 / 85

Table 4.4: Number of particles and simulation times, and how they relate to particle scaling and choice of time step, for the rotating drum (valid both for 10 and 20 RPM) in polyhedral / spherical simulations.

The simulation pace, calculated by dividing total running time by simulation time, is of 3.28 h/s for the ledge test and 3.58 h/s for rotating drum simulations at real-scale, the latter being slower due to the extra particles and constant motion of the drum mesh. Due to equalling of ratios (number of particles becomes 2.58 times smaller), the pattern is reversed at 30x scale, where simulation paces for ledge test and rotating drum were 42 and 28 s/s, respectively. Energy consumption for a 750W system can be estimated as 32.25 kWh for one 43-hours simulation, which becomes sizeable when multiple such simulations must be run on a calibration process, for instance.

5 PART II - CALIBRATION OF A COHESIVE POWDERED MATERIAL

Calibration of a cohesive material follows the same procedure for a free-flowing solid, with the addition of the cohesion parameter. Here, attractive forces were modeled by the novel formulation given in Equation 2.35.

To demonstrate that the material here shown is cohesive, its AoR on the heap test (Figure 5.1) can be compared to the Carr classification given in Table 2.1. It is clear that this particular material is on the transitional range between free-flowing and cohesive ("Fair to Passable Flow", between 38 and 45 degrees); the irregularities in both heap profiles are also suggestive of cohesion.

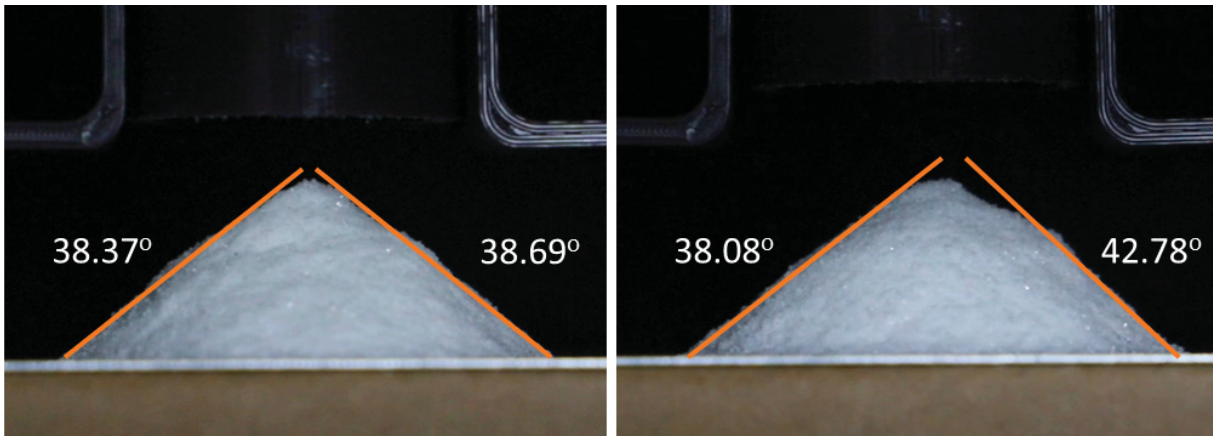

Figure 5.1: Heap test AoR measurements for the cohesive powder. It is classified as a "fair to passable flow" material, suggesting low cohesive strength. Pile edges are non-uniform, a behaviour characteristic of cohesive powders.

As in Part I, and by the same reasoning, all experiments described in Section 3 were performed, but only the ledge and rotating drum tests were used for calibration. An added complication for cohesive materials is the influence of consolidation stress on the AoR; in heap tests, for instance, loading the cylinder by its narrow opening is difficult, and using a tool such as a funnel to facilitate the process tends to pre-consolidate the material. This, in turn, causes the AoR to increase, and this pre-loading is difficult to reproduce in simulations.

This particular material has an assumed average size of 0.335 mm. At real-scale dimensions, correct contact and force resolution can only be achieved at double-precision floating point calculations, which are computationally intensive; for this reason, calibration is done at scales 5x and above.

5.1 EXPERIMENTAL RESULTS

5.1.1 Ledge Test

Ledge test procedures were the same as in the free-flowing tests: the 3 cm cube-shaped hopper was filled with material, and the hatch door quickly pulled to allow solid outflow. Figure 5.2 shows one of three measurements, which average to 23.20 degrees with a standard deviation of 0.46 degrees.

Figure 5.2: Ledge test measurement for one run of the cohesive material. Due to cohesion, there is high variability in repose angles, evidenced by the difference between the above measurement and the average triplicate value of 22.34 degrees.

5.1.2 Rotating Drum

Rotating drum assays, at evenly-spaced RPM intervals between 10 and 50 RPM, were carried out with a sample of the cohesive material, at about 33% of the drum's volume. Particle movement due to rotation causes repeated clumping and de-clumping of the cohesive material and, as evidenced in Figure 5.3, create unstable angles of repose. In (A), the angle formed at 10 RPM is fairly regular, which is to be expected at this velocity; in (B), however, which is a different frame from the same recording, a cascading-like profile is observed. The orange angle of repose line, measured in (A) but equal in both images, serves as a visual aid.

Due to the high variance in cohesive AoRs here shown, the Python-based procedure for average angle measurement adopted in Part I is improper, as it would lead to high standard deviations and a meaningless average value. Therefore, for the cohesive material, the average dynamic repose angle is measured "by hand" in Gimp, and is done with frames that display the behaviour in Fig. 5.3(A).

Such procedure is illustrated in Fig. 5.4, in which four separate frames of the 10 RPM video were extracted and their AoRs measured. Numbers in the top-left corners represent the particular video frames (out of 371) that were chosen, thus showing that measurements were carried out with samples across the whole video duration. At 10 RPM, the average angle is 43.75 degrees with a standard deviation of 0.91 degrees.

In the same manner, Fig. 5.5 shows the same procedure for the 20 RPM run, where the same slumping behaviour is observed (but not shown), and again only straight-edge samples were used. The average angle is calculated as 46.04 degrees with a standard deviation of 0.50 degrees, a slight increase from the 10 RPM case. In both cases, the average angle is about 10 degrees higher than the free-flowing counterpart in Part I, highlighting the effect that cohesion has on particle behaviour.

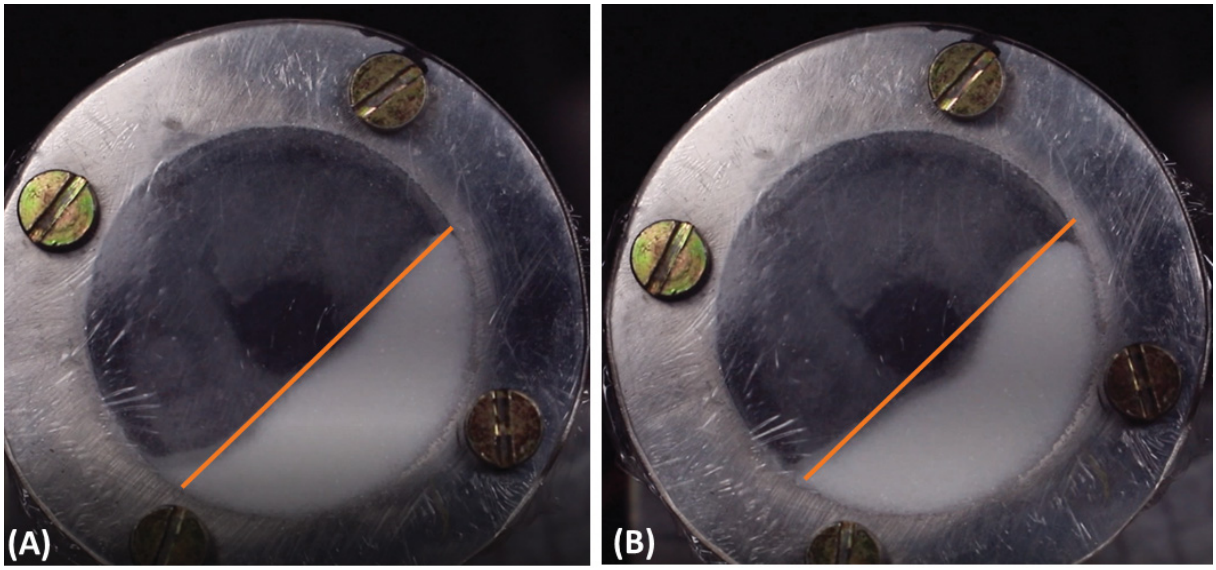

Figure 5.3: Still images of the cohesive material rotating drum experiment at 10 RPM. In (A), the angle profile is nearly continuous, an expected behaviour at low rotational speeds. In (B), material clumping causes a different, cascading profile. The orange line, which refers to the AoR measured in (A), is transposed to (B) to serve as a reference.

5.2 SIMULATION RESULTS

5.2.1 Calibration

Calibration is again done at 30x scaling, and then altered forward and backwards to evaluate the effects of upscaling on cohesive materials. Apart from the computational speed gains, doing so has the added advantage of matching the calibrated upscaling in Part I, since it was previously demonstrated that in dynamic situations, particle behaviour is altered by choice of upscaling; this becomes important for the mixing simulations in Part III.

Table 5.1 shows particle scaling and their corresponding critical time step. Contrary to Part I, the actual time step is smaller than half of the critical value. As attractive forces pull particles into each other, the limit of 0.05D on overlap has a higher tendency to be surpassed, hence creating instabilities in the simulation. For this reason, choice of time step in cohesive simulations need to be more conservative.

Scaling	Particle Size (mm)	Particle Volume (cm³)	Critical Time Step	Time Step
1x	0.335	1.97E-5	3.2E-6	–
5x	1.67	2.46E-3	1.6E-5	0.4E-5
10x	3.35	0.0197	3.2E-5	0.8E-5
20x	6.70	0.157	6.4E-5	1.5E-5
30x	10.05	0.531	9.6E-5	2.5E-5
40x	13.40	1.260	1.3E-4	4.0E-5

Table 5.1: Scaling factors and particle dimensions for the cohesive material.

At 30x scaling, the particle-particle and particle-surface friction coefficients for the cohesive material were found to be 0.35 and 0.7, respectively. The attractive parameter was calibrated to 0.025 which, for the model shown in Equation 2.35, is a low value; this matches the Carr classification and heap test observations made at this chapter's beginning. Finally, for the

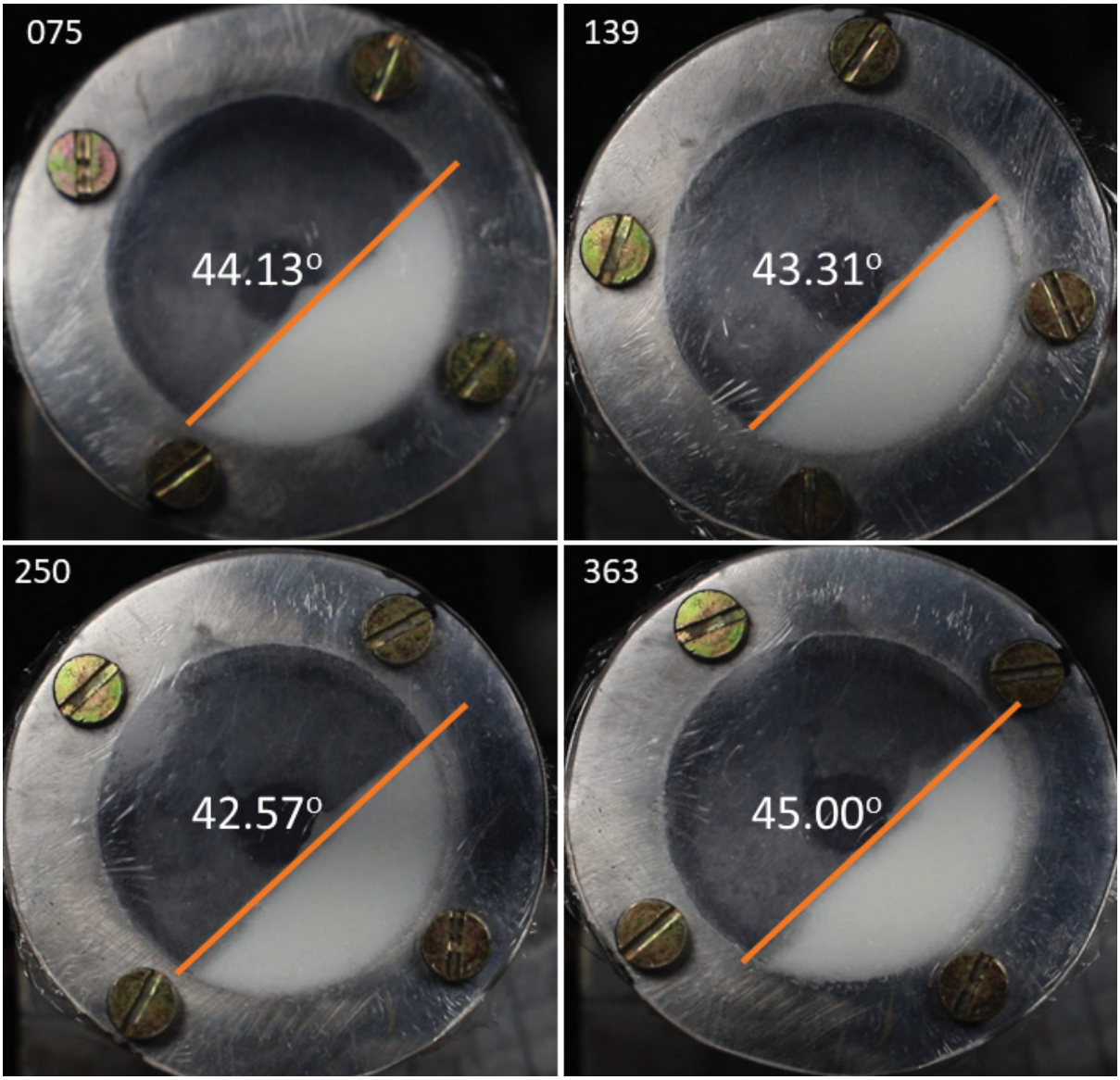

Figure 5.4: Angle of repose measurements for the cohesive powder at 10 RPM. Numbers in top-left corner are extracted video frames from a total of 371. Average angle: 43.75 degrees, Std. Dev.: 0.91 degrees

rolling friction parameter, calibration resulted in a value of 0.06 – smaller than the free-flowing material, suggesting that the cohesive material is less cubic overall.

Besides calibration, Part I had the added purpose of evaluating the computational gain of CGM and, to that end, choice of geometry upscaling was done with the intent of minimizing particle quantities while maintaining a proper particle-geometry ratio. Reevaluating simulation pace would be somewhat redundant – even if the added cohesive force does require extra calculations – since, on a GPU code, the main controlling factor is number of particles and how efficiently they can be distributed to the GPU's threads. This has been sufficiently demonstrated in the preceding chapter, and the focus here is showing how cohesion behaves with changing particle sizes.

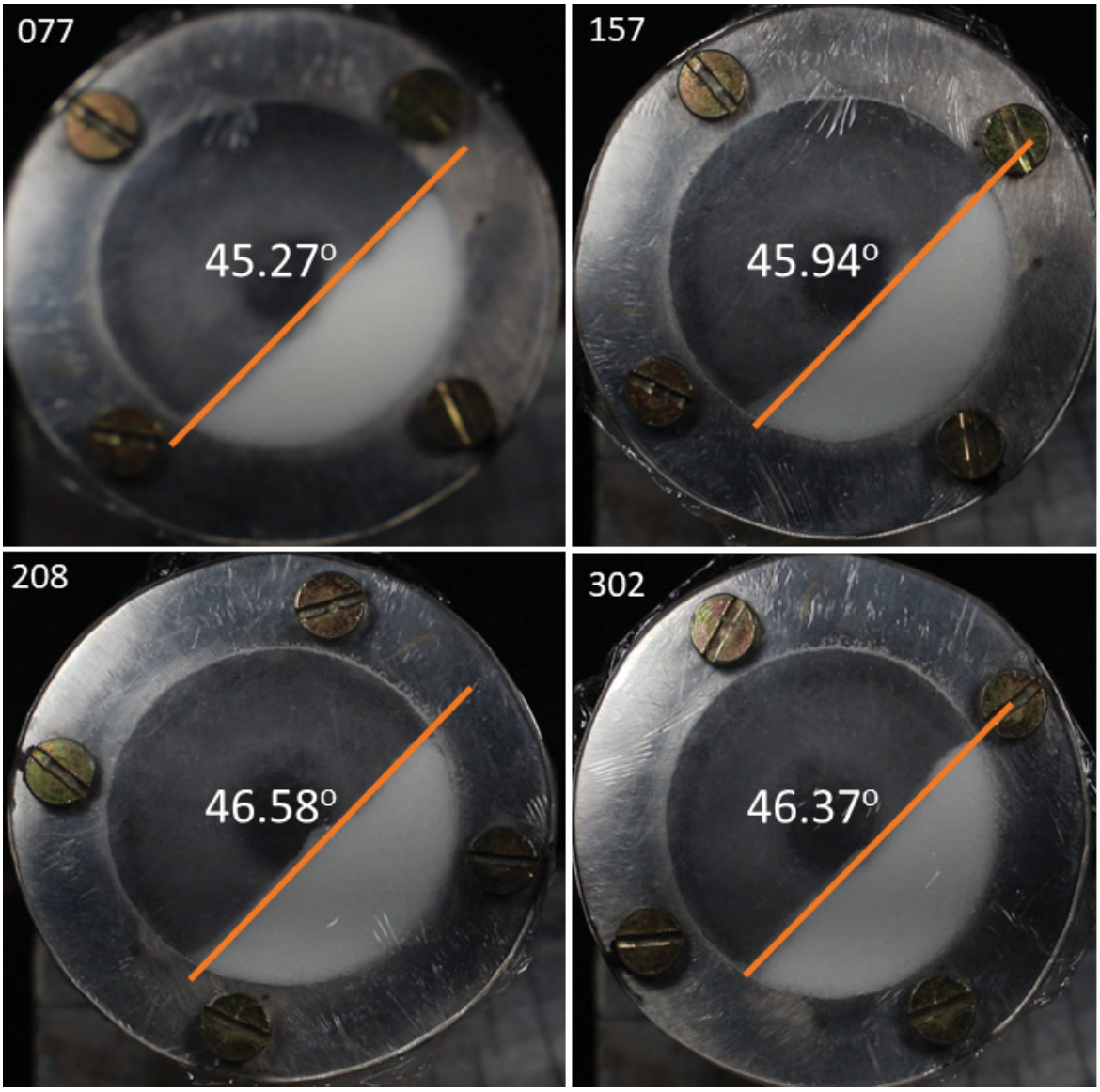

Figure 5.5: Angle of repose measurements for the cohesive powder at 20 RPM. Numbers in top-left corner are extracted video frames from a total of 310. Average angle: 46.04 degrees, Std. Dev.: 0.50 degrees

5.2.2 Ledge Test

As a matter of convenience, the ledge test box upscaling factors and dimensions were kept from Part I; since the cohesive material is a (smaller) cubic particle, the length-to-particle ratio is maintained above the critical range of 25 – 30 (Table 5.2).

Particle Scaling	Box Scaling	Particle Size (mm)	Charact. Length (cm)	Ratio
5x	3x	1.35 / 1.67	9	66.66 / 53.73
10x	5x / 6x	2.70 / 3.35	15 / 18	55.55 / 53.73
20x	10x / 12x	5.40 / 6.70	30 / 36	55.55 / 53.73
30x	15x / 18x	8.10 / 10.05	45 / 54	55.55 / 53.73
40x	20x / 24x	10.80 / 13.40	60 / 72	55.55 / 53.73

Table 5.2: Particle and Ledge Test box scaling, for polyhedral and spherical simulations (respective sizes separated by a slash), of the cohesive material. Ratios of characteristic ledge test length and particle size are also listed.

Figure 5.6 shows the comparison between the average experimental angle of repose (black and gray dotted lines representing one and two standard deviations, respectively) and AoRs measured at different scales. A similar pattern to that of the free-flowing material emerges: while spherical measurements were relatively stable across scales, the real-shaped AoRs have a higher degree of variability to them. Since the cohesive material has a much smaller average size, the (very high) mass effects that caused greatly increased AoRs at 40x scale in the free flowing material were not present.

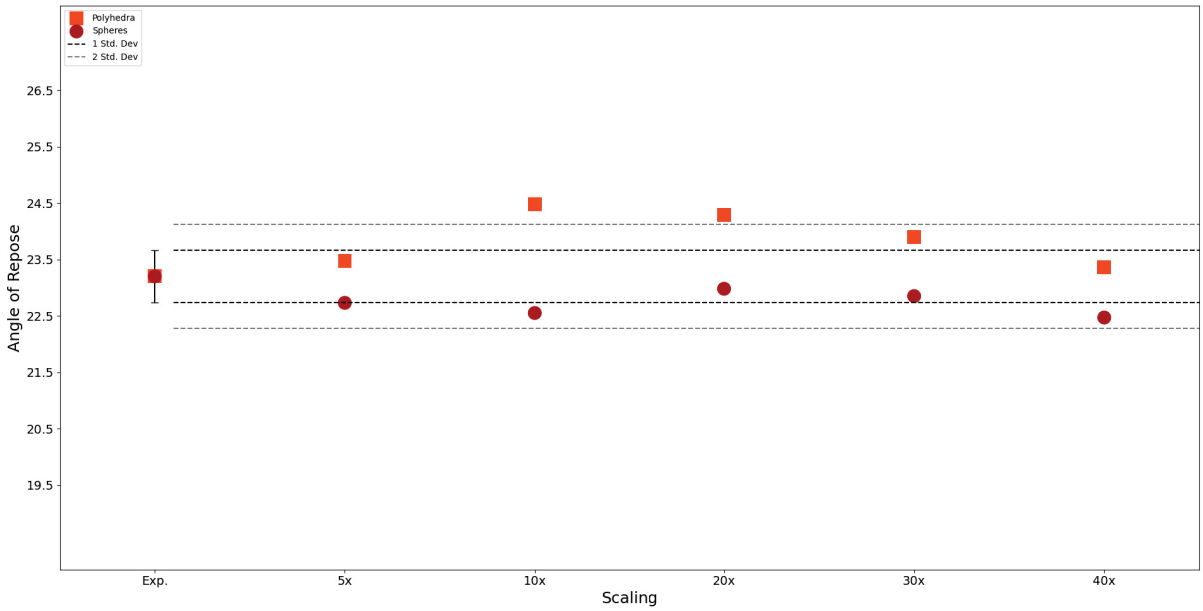

Figure 5.6: Ledge test simulation results for polyhedra (square, orange) and spheres (circles, red), compared to the experimental values. Dotted lines represent standard deviations from experimental results.

Results were generally close to the experimental average. The 10x scaling shows the largest deviation of about one degree, which is within the expected variability in CGM.[8] Previously, it was suggested that mass has a prominent role in ledge test simulation results. To evaluate this effect in cohesive simulations, Figure 5.7 presents polyhedral AoR measurements at 5, 10, 30 and 40x scaling; at the two smallest scales, the "tail end" of the solid heap is curved, which suggests that the increase in particle mass outpaces the increase in cohesive forces. Alternatively, the heavier particles in the other scales were able to break off the attractive force, giving them a more free-flowing profile. This effect, however, is relatively small, as the AoR measurements were sufficiently close.

5.2.3 Rotating Drum

Rotating drum simulations again follow a different scaling logic from that employed in Part I; because of clumping in experimental runs and the unstable AoRs that it brings, it is important to have a wider range of particles across the drum's diameter, as it allows for the development of a clearer repose angle shape. However, to reduce total particle count, drum depth is halved based on the assumption of planar symmetry, which in turn is predicated on the depth-invariant results observed in Part I.

Table 5.3 shows rotating drum upscaling for the cohesive case. Again deviating from previously adopted standards, both polyhedral and spherical geometry scalings were held equal for any given particle scale; apart from being more convenient, it allows for a comparison of polyhedral-vs-spheres holding geometry equal, which was not previously done.

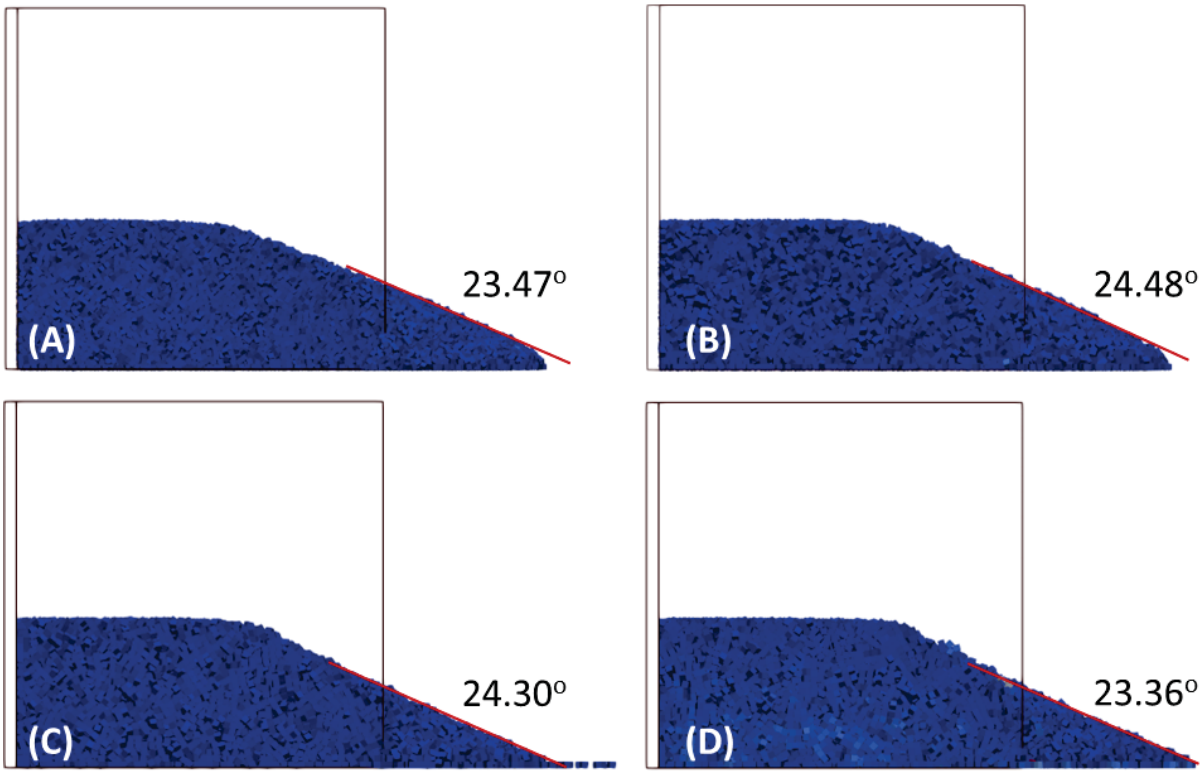

Figure 5.7: AoR measurements of the ledge test at (A) 5x, (B) 10x, (C) 30x and (D) 40x scaling for cohesive polyhedra. At lower particle weights, the larger relative influence of cohesion causes some rounding of the "tail end" of the experiment.

Particle Scaling	Drum Scaling	Part. Size (mm)	Charact. Length (cm)	Ratio
5x	3x	2.4 / 3.0	9.6	39.73 / 32.03
10x	6x	4.8 / 6.0	14.4 / 19.2	29.78 / 32.01
20x	12x	9.7 / 12.0	28.8 / 38.4	29.77 / 32.00
30x	20x	14.5 / 18.0	48.0 / 57.6	33.09 / 32.01
40x	25x	19.3 / 24.0	62.4 / 76.8	32.26 / 32.00

Table 5.3: Particle and rotating drum scaling, for polyhedral and spherical cohesive cases. Characteristic drum lengths and particle sizes are also listed.

In part I, an overlooked aspect of the upscaling of rotating drums was the Froude number and how it should change with increasing geometry sizes. Rotating speeds of 10 and 20 RPM were kept constant across all scales, thus increasing the Froude number (as per Equation 3.1); here, both this and a fixed Froude number approach were explored and the results compared. Some authors suggest that, in a given mixing process, the total number of revolutions – and not rotational speed specifically – is the key variable, thus giving credence to the idea of a fixed-RPM approach.[77–79]

As discussed in section 4.2.3, and using the Froude number equation (3.1), a general rule for the angular velocity with upscaling can be derived by equaling both Froude numbers at different scales, and recognizing that $R = f_{CGM} R_{1x}$:

$$
\begin{aligned}
Fr &= Fr_{1x} \\
\frac{\omega^2 R}{g} &= \frac{\omega_{1x}^2 R_{1x}}{g} \\
\omega^2 R &= \omega_{1x}^2 R_{1x} \\
\omega &= \omega_{1x}\sqrt{\frac{R_{1x}}{f_{CGM} R_{1x}}} \\
\omega &= \frac{\omega_{1x}}{\sqrt{f_{CGM}}}
\end{aligned}
\tag{5.1}
$$

where the subscript $1x$ denotes the real scale and the "subscriptless" variables represent any arbitrary scaling. The Froude number correlates gravitational forces in the denominator to centripetal forces in the numerator; hence, it is sensible that an increase in drum radius needs to be accompanied by a reduction in angular velocities to equilibrate the forces exerted by the walls on the particles.

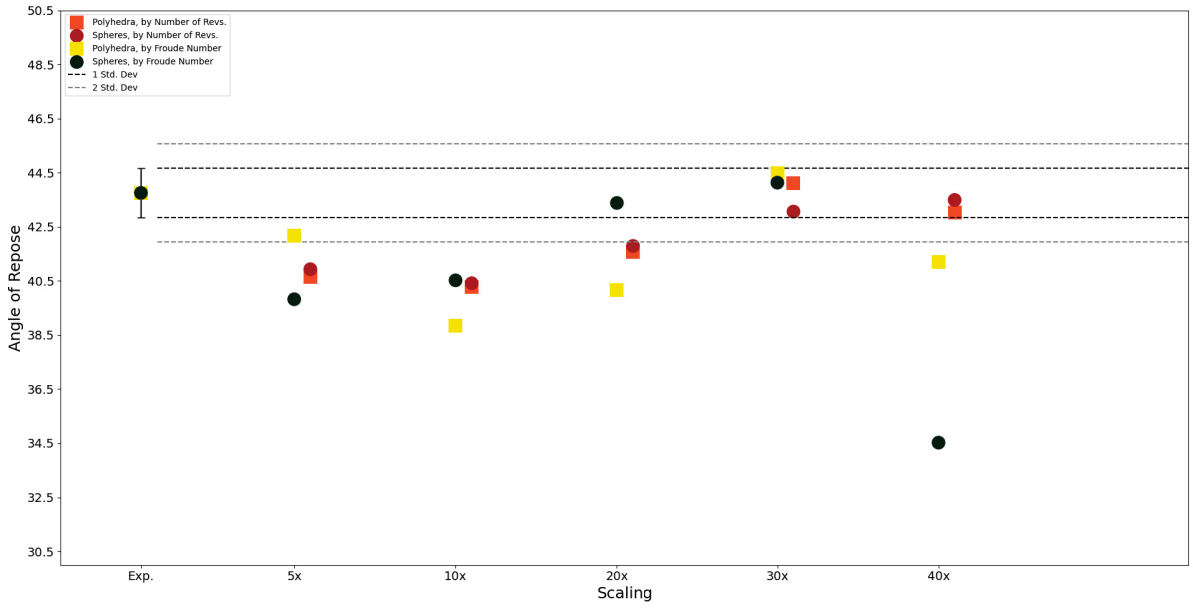

Figure 5.8: Angles of repose measured for the cohesive rotating drum simulations at 10 RPM, both scaled by matching Froude numbers (green, yellow) and number of revolutions (orange, red).

Between both scaling approaches, the general behaviour is similar in the 5- to 20-scaling range (Figures 5.8 and 5.9). The addition of a cohesive parameter causes – unlike in the free-flowing case – some deviations from the calibrated 30x case. In particular, as particle scales are reduced, bulk behaviour gets more cohesive, which also impacts AoR measurements as the material edge gets less defined (Fig. 5.10).

Feng suggests that a contact law of the form $F = KR^{\alpha}\delta^{\beta}$ must be scale invariant if $\alpha + \beta = n_d - 1$, where n_d is the number of dimensions (2D or 3D).[24] This relation holds for the Hertz contact model (Equation 2.13) but is violated for the cohesion contact model here discussed (Equation 2.35). Moreover, penetration depth is generally limited as a percentage of particle radius; hence, from the aforementioned equations, it is clear that the Hertz model increases by the square of particle radius while the cohesive model increases linearly. Normal forces outpace cohesive forces, meaning that the reduction in particle scales relatively increases cohesion.

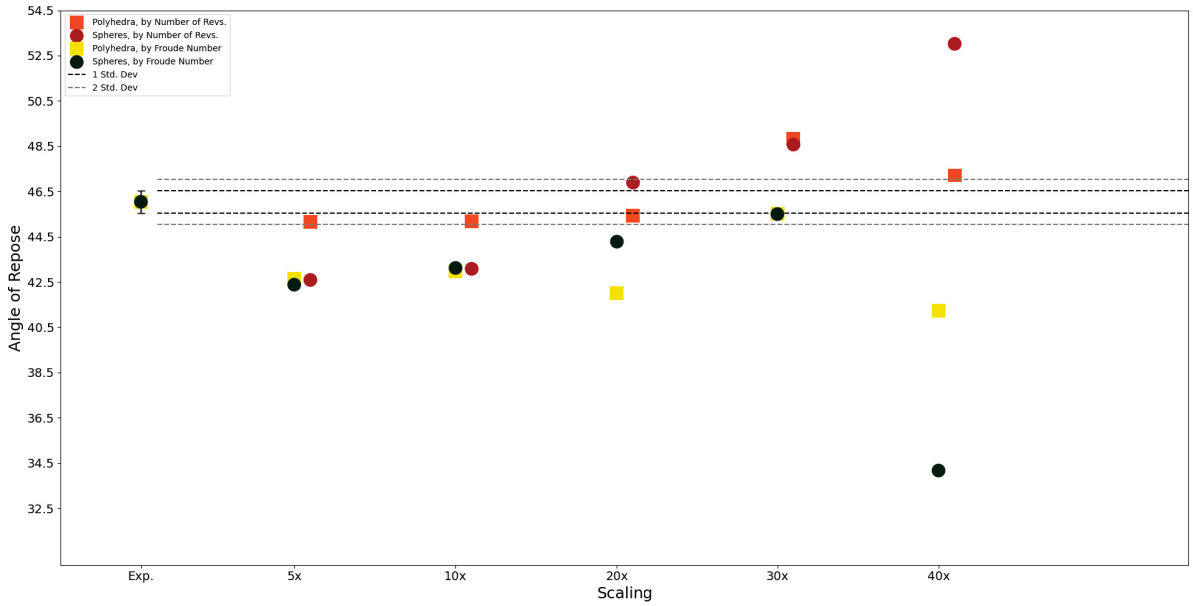

Figure 5.9: Angles of repose measured for the cohesive rotating drum simulations at 20 RPM, both scaled by matching Froude numbers (green, yellow) and number of revolutions (orange, red).

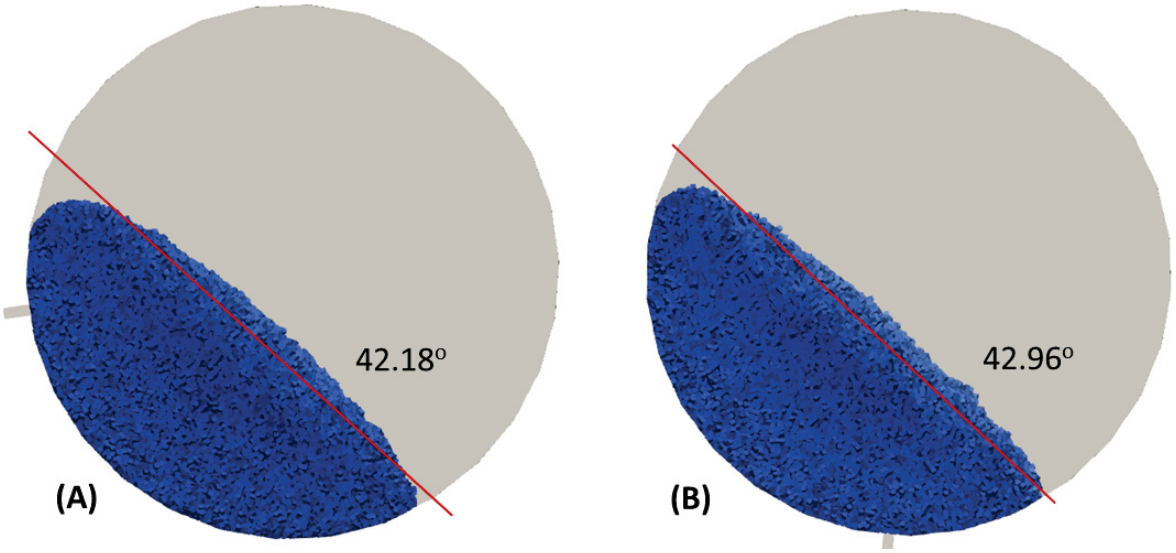

Figure 5.10: Rotating Drum simulation images of the (A) 5x polyhedral and (B) 10x polyhedral cases. Rotation speeds were 10 and 20 RPM, respectively, and rescaled to match Froude numbers.

Similarly, for the Froude-scaled case, particle mass increases at a higher rate than the centrifugal forces from the drum walls, since the former is scaled by f_{CGM}^3 while the latter is linearly increased. The reduction in AoRs at 40x might be imputable to this difference, as the force exerted by the walls might not be enough to compensate the extra particle weight; this is more pronounced in the spherical cases, while the added stability of the cubic polyhedral shape might compensate this phenomenon.

Finally, 30x and 40x scalings at 20RPM show large differences in calibrated Angles of Repose. From Equation 3.1, the Froude number at 30x and 10 RPM is 1.4E-3, which barely falls into the transition range between rolling and cascading regimes (1E-3 to 1E-1);[80] at 20 RPM and larger scales this limit is well exceeded, thus causing the edge profile to become divided into lower and upper angles, which is harder to compare to the experimental run.

Figure 5.11 shows this effect: in (A), the 20x case at 20 RPM is (barely) in the rolling regime; in (B), at 40x and 20 RPM, particle behaviour is fully cascading due to the increase in Froude number. (C) and (D) both show polyhedral particles at 30x scaling, the former at adjusted 10 RPM and fully rolling regime, the latter at true 10 RPM and approaching a cascading profile.

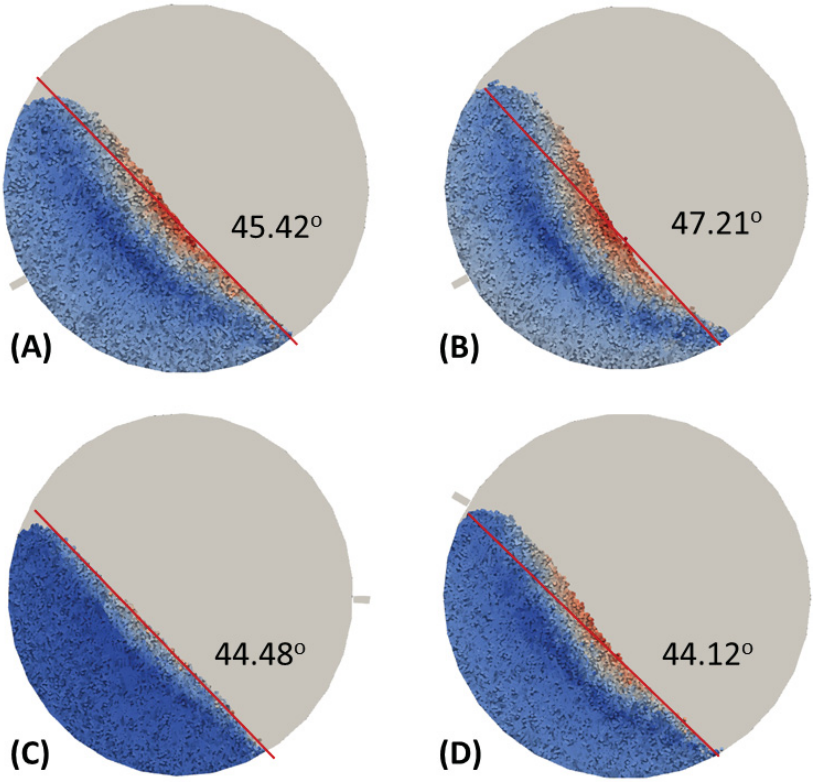

Figure 5.11: Rotating drum images showing the effect of increased Froude numbers on AoR. In (A), 20x scaled particles at 20 RPM are barely in the cascading regime; when the Froude number increases in (B) due to geometry upscaling, cascading is more pronounced. (C) and (D) compare the 30x scale at adjusted and non-adjusted RPMs, respectively, showing a change in flow regime.

In conclusion, results suggest that flow regime, and not the Froude number itself, is the key parameter in rotating drum calibrations. As long as both approaches – maintaining Froude numbers or number of revolutions equal – fall into the same flow regime, results were similar, as evidenced by the proximity between both approaches in 5x to 20x scalings. Greater differences in repose angles occur when the higher RPM in the second approach cause a transition into the cascading regime, thus altering the edge profile itself. In Part I, since geometries were scaled at smaller rates, Froude numbers do not exceed the above limits; hence, the AoRs were unchanged when parameters were retested with adjusted Froude numbers – confirmed by the testing of 30x scaling at an adjusted RPM of 3.16 with similar AoR to the 10 RPM case.

6 PART III - CALIBRATION OF A BINARY MIXTURE IN AN IN-BIN BLENDER (IBB)

Parts I and II were concerned with the individual calibration of two particulate solids (a free-flowing and a cohesive material), with the intent of obtaining a set of parameters that reproduce their bulk behaviour in simulation. Here, both materials were experimentally mixed and its results confronted with those obtained by simulation – this is, in essence, a calibration. If AoR experiments are, in fact, a good proxy for bulk characterization of particulate solids, then the simulations should fall within reasonable range of the experimental results.

6.1 EXPERIMENTAL PROCEDURE

In-Bin Blenders (IBB, Fig. 6.1) are a class of mixing equipment consisting of a bin (a container for bulk solids) that is rotated perpendicular to its longitudinal axis, thus providing mixing by the free-fall of material.

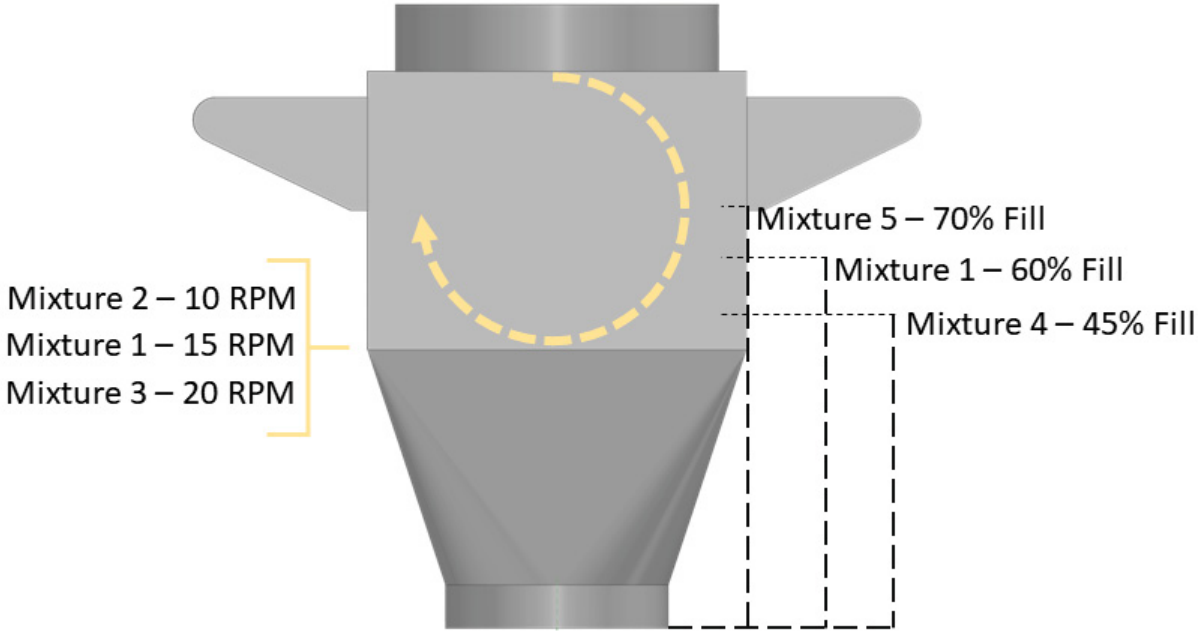

Figure 6.1: CAD representation of the labratory-scale In-Bin Blender (IBB) used in experiments and in simulations. Also shown are fill heights and rotational speeds for all five studied mixtures.

Five mixtures of the free-flowing and cohesive materials, on a 70/30 mass proportion, were carried out in a lab-scale IBB; this ratio of materials was chosen to balance computational load (as the bigger FFM is present in larger quantities) and overall cohesion. Fill percentage (or, more conveniently, total mass) and rotation speed were varied to evaluate the influence of such parameters on the mixing process (listed in Table 6.1). Mixing time was set at 300 seconds for all cases, and both materials were filled separately – the larger free-flowing material was added first and, on top of it, the cohesive material, forming two layers. After completion, the IBB was sampled in three different locations:

- at the top, by removing 100g of material via the main hatch;

- in the middle, using a powder sampling rod to remove 100g from the centre; since it needs to be inserted through the material, this is an invasive procedure;
- and in the bottom, by opening the IBB's butterfly valve; 200g of material is typically removed, as the valve is harder to control.

Sampling order was top–down. Approximately 5g of material, taken from each of the three sampling points, were diluted in 1L of water for quantification.

6.1.1 Experimental Results

Table 6.1 presents the experimental results in terms of the cohesive material, which was measured by an automatic potentiometric titrator – measurements were performed twice for each point, and their standard deviations are reported in parenthesis. The experimental parameters, also listed in the same table, were chosen so that Mixture 1 acts as a "central point", and pairs 2-3 and 4-5 vary one parameter in either direction. Fill percentages (in terms of IBB volume) were estimated at 45, 60 and 70% for total masses of 2.0, 2.5 and 3.0 kg, respectively.

	Mass (kg)	RPM	Top	Middle	Bottom
Mixture 1	2.5	15	33.82% (±0.65)	28.20% (±0.90)	32.31% (±0.65)
Mixture 2	2.5	10	29.99% (±2.06)	32.74% (±0.06)	30.75% (±0.58)
Mixture 3	2.5	20	31.08% (±1.76)	31.12% (±0.00)	32.10% (±2.86)
Mixture 4	2.0	15	34.50% (±1.12)	31.75% (±1.98)	32.67% (±1.77)
Mixture 5	3.0	15	33.23% (±0.13)	31.57% (±0.35)	28.09% (±1.25)

Table 6.1: Results for all experimental IBB runs, in terms of the cohesive material percentage at all three sampling points. Rotation speed and total mass, which were the varied parameters, are also listed for all mixtures.

For a perfect mixture, it would be expected that for all sampling points cohesive material quantification would yield the same value as the theoretical makeup (i.e. 30%); in most cases the theoretical value is surpassed, suggesting some material concentration along the sampled middle line.

In discussing experimental results, it is important to note that the free-flowing material (FFM), due to its larger size and proportion in the mixture, is in a much larger volumetric proportion than the cohesive material (CM); furthermore, there is a large size ratio between both materials, so that the mixing process occurs mainly by percolation of CM through the gaps of the FFM.

The Brazil Nut Effect (BNE)[†] is a phenomenon whereby large particles tend to rise to the top of a shaken container in the presence of smaller particles, seemingly contradicting the idea that heavier matter should fall to the bottom – for example, on a liquid mixture of two different densities. Some proposed mechanisms for BNE include percolation of finer particles through the gaps of larger particles (or void filling) and granular convection of big particles (which does not permit their re-circulation), among others.[81,82]

More recently, a Reverse Brazil Nut Effect (RBNE) has been demonstrated, where large particles "sink" through the smaller particles.[83,84] Hong *et al* proposed a "condensation" mechanism and theoretically predicted that, if $d_l/d_s > \rho_s/\rho_l$ holds (where l and s represents

[†]So called because of the observable tendency that large Brazil nuts have to rise to the top of containers of (smaller) mixed nuts.

large and small particles, respectively), then RBNE happens.[85] Breu *et al* tested this relation in 178 different mixtures, finding that it correctly predicts demixing in only 82% of cases.[86] Overall, there are ten main possible mechanisms for BNE and RBNE, illustrating their non-trivial and curious nature.[82]

Segregation of granular materials in rotating drums has the added component of wall-exerted centripetal forces, which can counterbalance the gravitational forces that cause BNE in the "Cartesian coordinates" examples discussed above; here, segregation occurs in "polar coordinates", where the drum's walls are the top and the center forms a core of smaller particles.[87] Many studies correlate parameters such as fill height, particle shape, rotational speeds and particle densities to the occurrence (or reversal) of the Brazil Nut Effect.[87–90] In terms of rotational speeds, it has been shown that an increase to Froude numbers – or an increase in centrifugal forces over gravity – can invert the segregation pattern from BNE to RBNE, as the smaller and/or lighter particles get pushed to the edges, depending on size and density ratios.[88,90]

Hence, a "first approach" explanation – as simulations should better elucidate the dynamics inside the IBB – can be produced for the behaviour in the RPM-varying simulations. At 10 RPM and a low Froude number, there is a tendency for the smaller cohesive material to accumulate in the core due to the BNE. As speed is increased to 15 RPM, there is a mild reversal of this behaviour as centripetal forces are increased. At 20 RPM, which is closer to cascading, a more homogeneous mixture is obtained, possibly due to the formation of gaps in the rapidly flowing material that are more permissive of particle motion.[89] In all cases, mixture cohesiveness counters segregation,[91] so that the differences across sampling points are not as pronounced. Moreover, cylindrical rotating drums provide only shear forces through the walls; in an IBB, there is lifting of material by its irregular shape, which should influence mixing dynamics.

Cases 1, 4 and 5, which differ only on fill percentage, were remarkably similar, apart from the middle of Mixture 1 and the bottom of Mixture 5. In general, an increase in fill height (which implies a reduction in headspace) reduces mixing performance, both in speed and quality, as there is less freedom of movement and a relatively smaller flowing region.[92]

6.2 SIMULATION RESULTS WITH CALIBRATED PARAMETERS

All simulations were carried out using the calibrated 30x scaled particles from Parts I and II; due to the relatively high particle count, only spheres were simulated. The IBB was upscaled by 5x its original size, and rotational speeds in Table 6.1 were adjusted to match experimental Froude numbers.

Simulation results were "sampled" in a manner that tried to mimic the experimental procedure (Fig. 6.2 (C)); particle .VTK files were imported into Paraview, and three regions corresponding to the sampling points were clipped from the full simulation. Then, by the particle count and mass of each component in these regions, the percentage of CM was computed. In comparing simulations to experiments, a tolerance of ± 10% is assumed permissible.

The bottom point is the most straightforward sampling region, as the experimental procedure consisted in opening a valve; assuming uniform flow out of the IBB, a full slice of the bottom section is taken as a simulated sample. The sampling rod used in the middle is a slender cylinder that has to be introduced through the solid. It can therefore be erratic in the actual point of removal, as well as disturbing the granular bed. For those reasons, middle samples were also taken as a full slice of material. The top point, however, is limited by the hatch opening, and since sampling was done by hand, a more central portion was consistently taken out; in simulations the sample is delimited by a wide cylinder, to ignore material near the wall.

As a parameter of mixing quality, a Subdomain Mixing Index (SMI) is implemented in BlazeDEM. In summary, the simulation domain (i.e. the IBB) is divided into cells, or subdomains, of arbitrary length at least 10x the largest particle. For each non-empty subdomain, the mass ratio of particles is calculated and "compared" to the expected ratio (here, 70/30); the index is then $1 \leq x \leq 0$, where 1 corresponds to a subdomain which exactly matches the expected ratio and 0 is complete segregation (i.e. only one type of particle present). Finally, valid subdomains are averaged to give a global mixing index (NetMI), which represent the overall mixing quality. Mixing index calculations were performed each 0.25 seconds, showing progress over time.[93] All NetMI plots were smoothed using Savitzky-Golay filtering (polynomial order n = 1).

6.2.1 Attempts Using Calibrated Parameters

An attempt at reproducing Mixture 1, using both materials as presented in Parts I and II and with their respective calibrated friction and cohesion values, is shown in Fig. 6.2 (A), while (B) shows the same simulation result with FFM removed and CM isolated.

Cohesive particle distribution is good radially, but it remains "flat" in the plane of rotation. This lack of effective distribution causes quantification results to greatly differ from the experiments. From top to bottom, the CM percentages (as sampled in Fig. 6.2 (C)) are 46.7%, 33.1% and 23.7%, suggesting the AoR calibration approach is not fully capable of representing particle dynamics in this particular case.

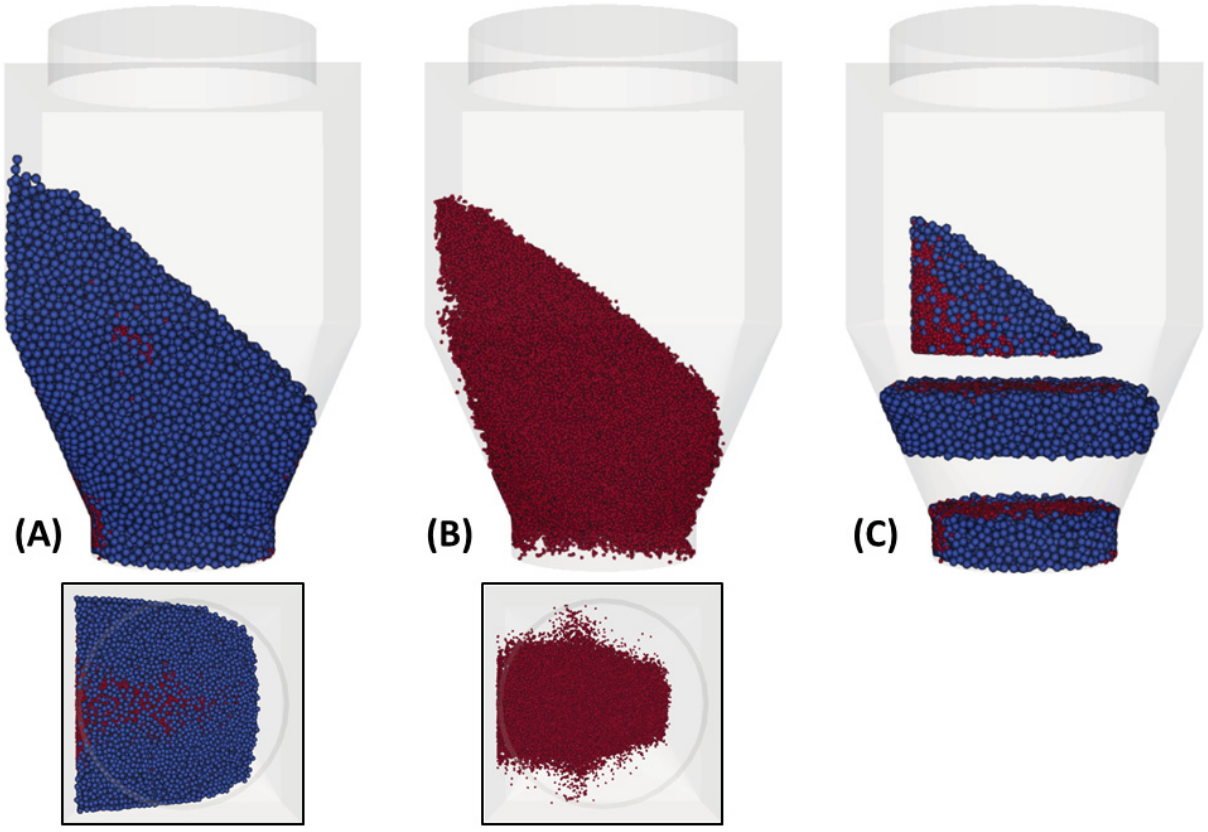

Figure 6.2: Simulation results using particle sizes and parameters as calibrated in Parts I and II, after 5 seconds of stationary settling. In (A), both FFM and CM are shown together; in (B), FFM is removed to isolate the CM. In both cases, the top view of the IBB is presented below, showing a concentration of CM in the rotation plane. (C) shows the sampling methodology applied to both materials.

	Calibrated Params.	(A)	(B)	(C)	(D)	(E)	(F)
Top	46.7%	25.1%	45.8%	34.2%	37.2%	50.7%	20.7%
Middle	33.1%	35.9%	37.6%	43.3%	39.9%	33.6%	24.1%
Bottom	23.7%	23.1%	11.6%	13.2%	5.7%	0.2%	38.8%

Table 6.2: Sampling results for IBB simulations using original parameters and their variations: (A) 0.0 Friction; (B) 1.0 Friction; (C) 0.0 Rolling Fric.; (D) 1.0 Rolling Fric.; (E) 0.5 Cohesion; (F) 1.0 Cohesion.

6.2.2 Effect of Varying Parameters on Simulation Results

To evaluate the effect of friction coefficients (both static and rolling) and cohesion on the results, the same simulation was rerun by individually varying static or rolling friction coefficients to 0.0 and 1.0 (for both components) and CM cohesion to 0.5 and 1.0. Images for each run are presented in Fig. B.1 and Table 6.2 presents sampling results. To save computation time, new simulations were run for 150 seconds.

Smaller friction coefficients improve mixing as resistance to inter-particle motion is reduced, which increases the velocity at which the moving layer flows; similarly to the rotating drum (as discussed in Section 6.1.1), this causes gaps by which smaller particles percolate. Fig. 6.3 (B), which compares the original run to the 0.0 Rolling Damping case during their first revolution, illustrates such behaviour, as the bulky FFM is coloured by particle velocity and CM (solid green) can be seen amongst the rapidly flowing layer at no rolling resistance. Another mechanism by which mixing occurs is visible in the same image (A): at 5 seconds, the repose angle formed by FFM in the higher friction case "traps" CM particles. Lower friction causes them to be nearer the surface, which in turn allows them freedom to move, and percolate, in the flowing layer at 12 seconds, provoking mixing of the material.

Increased CM cohesion has an unexpectedly adverse effect in mixing (Fig. B.1 (E) and (F)), as cohesion generally causes particle clumping that prevent them from segregating.[91] Excessive cohesive forces cause large and stable clumps that prevent mixing, as there is no inter-penetration of different material particles.

It becomes clear that the IBB modelling up to here is insufficient and misses key aspects of the real process. However, an understanding of the general dynamics that develop inside the bin can be gained from current results, which is useful in understanding improvements that have to be made in order to accurately model mixing inside the IBB. Fig. 6.4 presents mixing indices over time for all mixtures, and it is noticeable that in Mixtures (B) – (D) and in the original run, NetMI curves peak between 20 and 80 seconds and then fall until a steady-state is reached. This implies that two separate mechanisms develop inside the IBB: the first promotes mixing and, after a certain degree of homogeneity is attained, the second causes segregation.

The discussion on the effects of lower friction help to characterize the first mechanism, as illustrated in Fig 6.3(A). In the first minutes of rotation – and since both materials were filled separately, CM on top of the FFM – mixing happens by particles falling over each other, which is the defining characteristic of an In-Bin Blender; frictional and cohesive parameters control their inter-penetration, as previously demonstrated. Eventually, both materials get fully incorporated, which is characterized by the peaks of mixing indices.

One possible explanation for the segregative mechanism is the Brazil Nut Effect, as discussed in Section 6.1.1, in rotating drums; however, it is unlikely as good radial distribution was attained for the original case. Fig. 6.3(B) shows velocity-induced percolation that aids mixing, due to the already-segregated state in the first revolutions. At later stages, percolation

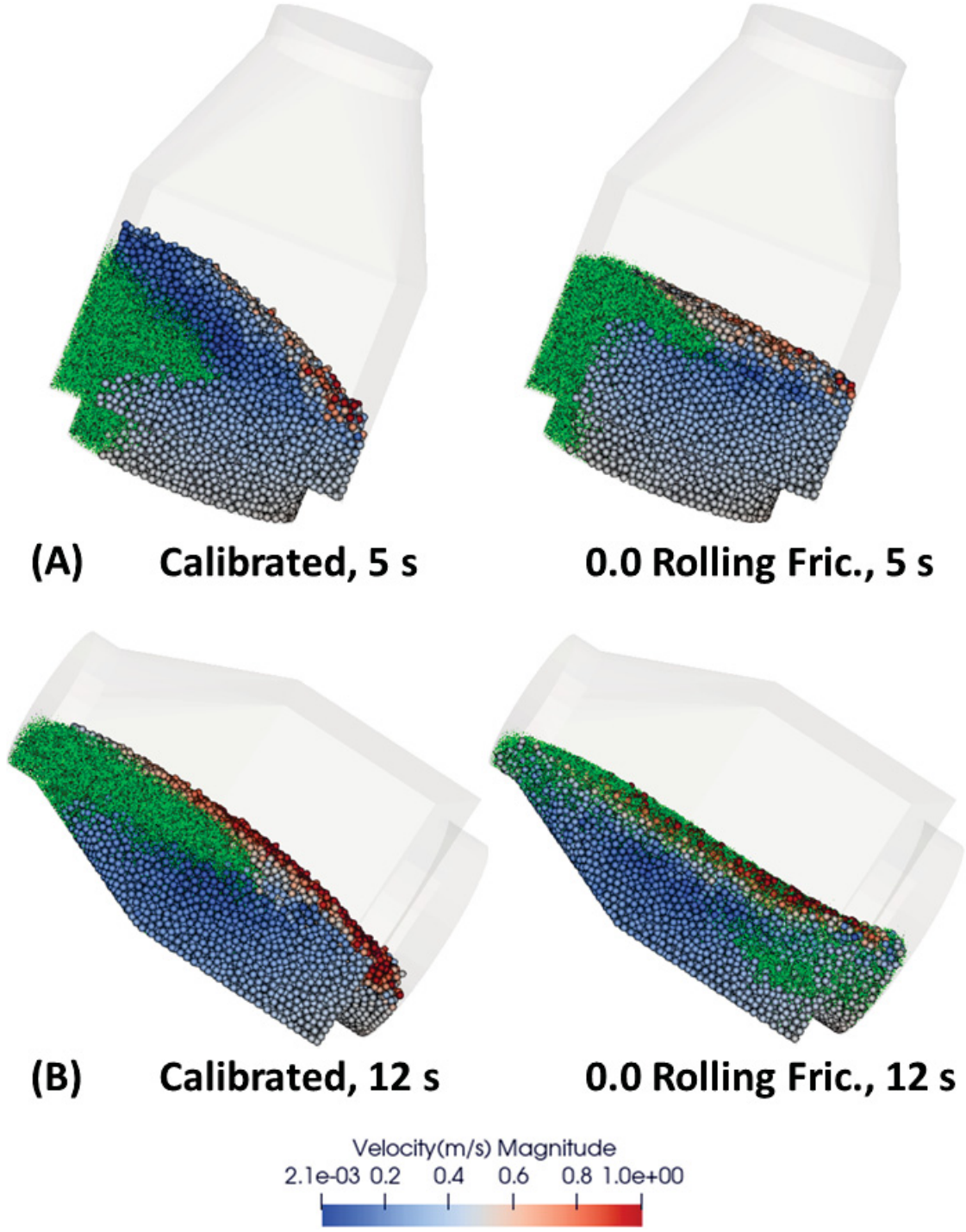

Figure 6.3: Demonstration of the first mixing mechanism between 5 and 12 seconds, whereby the Angle of Repose formed inside the IBB controls mixing rates at the start of operation. FFM material is coloured by velocity, in m/s, and CM is shown in green. In (A), an AoR develops in the left-hand "Calibrated" case due to frictional forces, which trap CM that is unable to freely flow in (B); in contrast, the right-hand "0.0 Rolling Friction" case exposes CM, which is then free to percolate in the rapidly flowing FFM surface layer.

may drive CM particles to the bulk core; however, for poorly mixed cases, finer particles are already concentrated inside the bulk, and this segregative percolation is insignificant.

Fig. 6.5 compares the seventh revolution of the calibrated run (A) to the 0.0 Friction case (B), which shows no de-mixing in the NetMI curves, between 54 and 63 seconds. At this point in time, the former is at peak mixing index and about to segregate, while the latter is

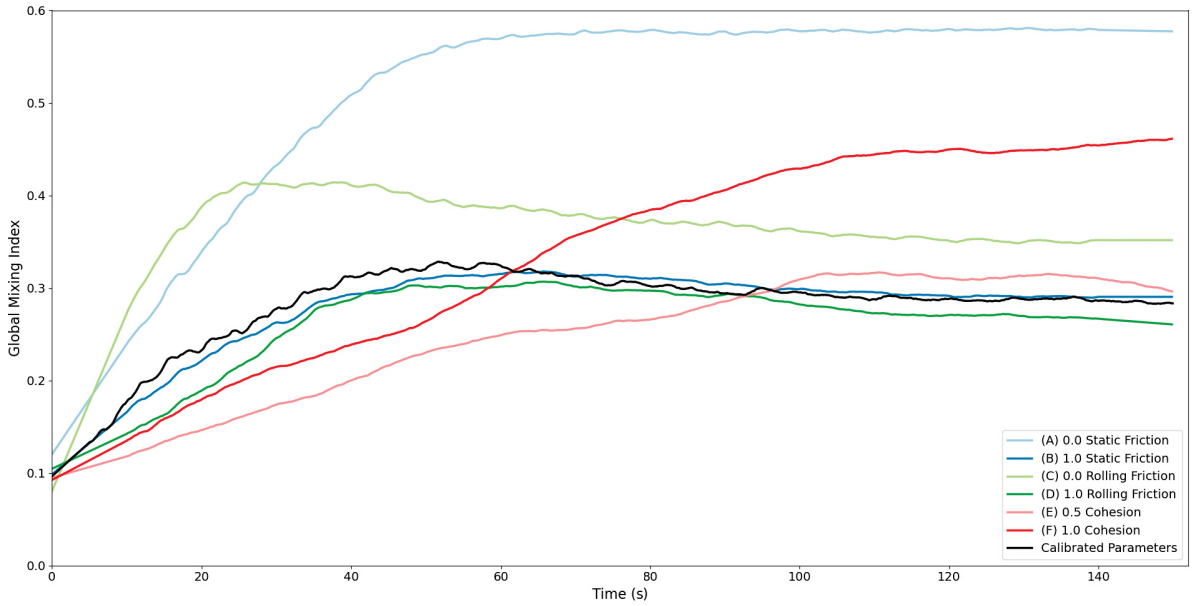

Figure 6.4: Global mixing indices for the original parameters simulation of the IBB and its variations, as shown in Fig. B.1. Curves were plotted up until 150 seconds as it is sufficient time to reach steady-state in most cases.

reaching steady-state. In (A), when the IBB is upright, the mixture is already mildly segregated, suggesting the first mechanism slows down during preceding revolutions. As the bin moves to 1/4 of a revolution, the material slumps forming an AoR dependant on friction. While the frictional case in (A) forms a relatively stable pile, the frictionless material in (B) readily collapses and reaches the IBB top cover. Hence, the downward motion into the 1/2 rev position is much less abrupt in (B) – in (A), the AoR must be overcome for the material to collapse, in essence causing the material to be "poured". At this point, particles get de-mixed by sifting segregation,* which concentrates finer particles near the impact point while larger and heavier particles spread away.[94] This explains why CM has good radial distribution in the end of mixing, but is poorly spread in the axial direction (Fig. 6.2(B))

As a final verification, 0.0 Friction is compared to the 0.0 Rolling Damping case since, for the argument of AoR-controlled mixing to hold, their behaviour should be similar – as the main function of rolling friction is to increase repose angles. The mixing indices (Fig. 6.4) of both rapidly increase due to reduced AoRs; the main difference lies in de-mixing observed at around 27 seconds for 0.0 RD. Fig. B.3 shows this case at 24.7 seconds, in which the profile shape resembles the 1/4 turn in Fig. 6.5(A) – suggesting the same segregation mechanism happening in a similar manner for both cases. Moreover, it implies percolation is highly dependant on friction coefficients, as the frictionless case shown in Fig. 6.5(B) has a better distributed CM profile.

It is reasonable to assume that both proposed mechanisms happen simultaneously and are, therefore, competing. The "flattening" effect, observed in CM, of the second mechanism might reduce the effectiveness of the first; conversely, sifting segregation cannot occur on heavily layered mixtures, like in the first few revolutions. Fig. B.4 demonstrates sifting segregation for FFM and CM on a cylindrical bin, using calibrated parameters. Contrary to the IBB filling procedure, both materials were filled into the simulation together – as if they were "pre-mixed" before pouring. There is clear formation of a central CM "band", while FFM forms a more regular pile.

*While the term "sifting segregation" can more generally be applied to any small-through-large particle percolation, here it refers exclusively to the side-to-side segregation on pile formation.

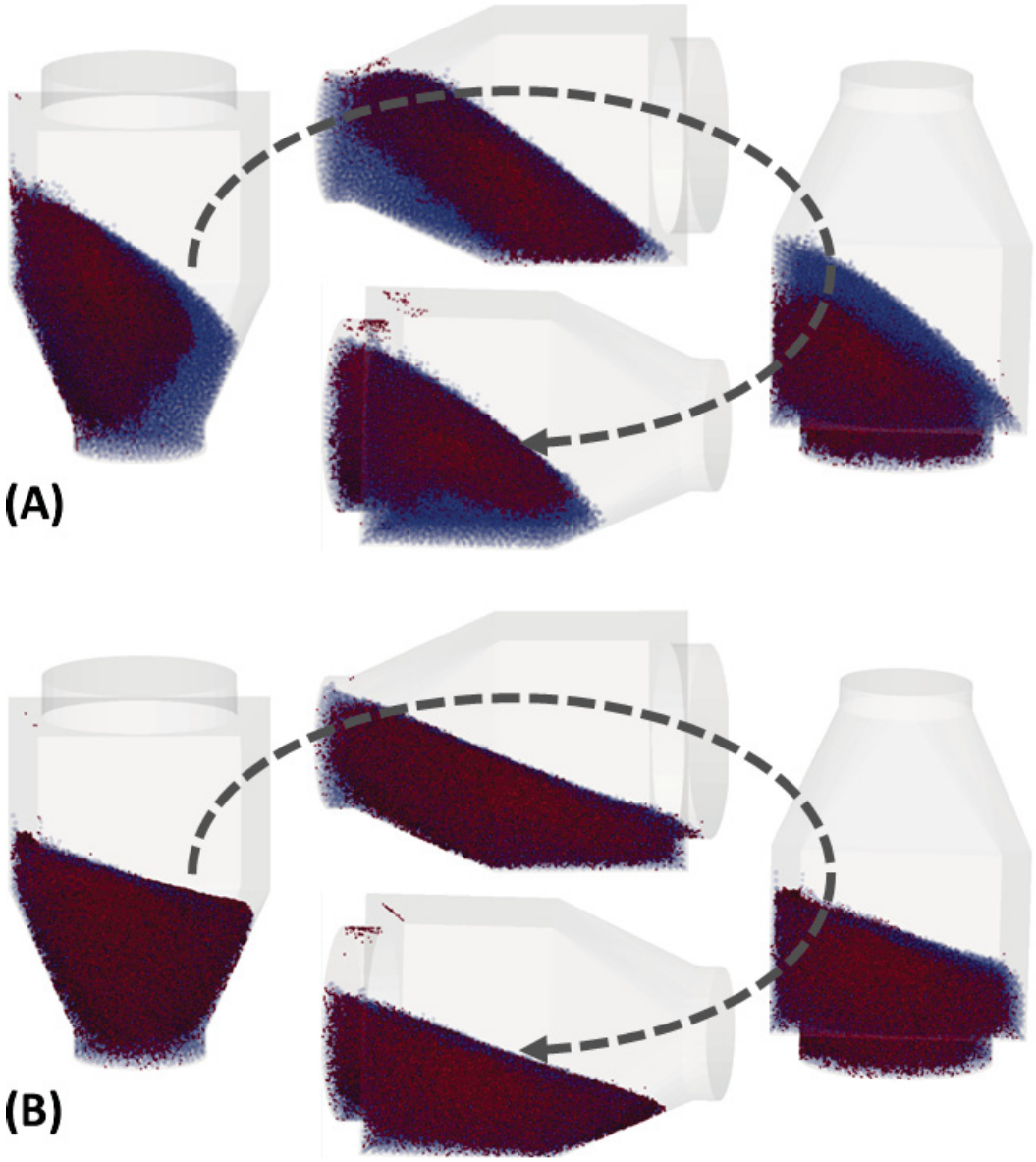

Figure 6.5: The second proposed mixing mechanism, shown on the seventh revolution between 54 and 63 seconds, compared between (A) the "Calibrated parameters" and (B) "0.0 Friction" cases. Both mixing state at the beginning, and AoR formation when the IBB is rotated sideways, control sifting segregation that concentrates CM (red) at the bulk core, while FFM (blue, translucent for ease of viewing) rolls on top.

All preceding discussions are based on simulations that, ultimately, failed to reproduce the correct experimental behaviour. While useful in understanding the basic dynamics of the mixing process, there must be another, unaccounted factor that reduces sifting segregation for these particles. Four conditions must be met for sifting segregation to occur, according to ASTM-set standards:[95,96]

- a difference in particle sizes between materials, with larger size ratios raising segregation tendency;
- a mean particle size of at least 50 μm, with mean sizes above 100 μm showing increased sifting predominance;
- relative motion between particles, which causes a velocity gradient across granular boundaries;

- and sufficiently free-flowing material, as cohesive particles stick together and do not percolate, as already extensively discussed.

The first two conditions are resoundingly met both at real and upscaled sizes, while the third is satisfied by the rotating motion of the IBB. The cohesion criterion, however, is more malleable, as cohesion can have many origins – for example, particle interlocking due to shape.

Parts I and II simulated materials as cube-shaped, an approximation based on microscope images of both particles. This is an over-simplification for modelling purposes, since particle shape tends to be irregular due to diverse reasons, such as methods of production, breakage during transport and handling, etc. Nevertheless, the equivalent-sphere approach dictated that these cubes be resized so that their volume matched a sphere of the assumed particle diameter D. By equalling the volumes of both geometries, it is trivially shown that the side length of such cubes are approximately given by $a = 0.806D$; the cube's face and body diagonals then become $diag_f = 1.14D$ and $diag_b = 1.40D$, respectively. The implication is that cube percolation depends on orientation: a sphere (simulated in place of a cube, as is the case in Part III) tends to under-predict percolation if the cube is perfectly aligned with a given gap, but over-predict if its diagonals face the same gap (Fig. B.2 provides an illustrative example).

It is difficult to assert the net effect that particle shape has on percolation, especially on real systems with wide size (and shape) distributions; it must depend on an "average gap size" generated by the velocity profiles developed inside the IBB, as well as on a statistical probability of particle alignment. Moreover, the above discussion is exacerbated for high aspect ratio particles, but reduced for finer fragments. Some studies have shown a strong effect of particle shape and sizes in segregative mechanisms. It has been experimentally suggested that spheres have a higher tendency to segregate due to higher flowability, while particle angularity tends to prevent percolation.[97,98] The work of Alizadeh *et al* is particularly interesting, as experimental sifting segregation was compared to real-shape and spherical (with rolling friction) solutions.[99] Although their work is concerned with exclusively shape-driven segregation (i.e. both particle types were of the same size) and used highly irregular particles, rolling damping is demonstrated to misrepresent segregation – in accordance with the inability of RD to match percolation (as shown in this work) and other phenomena related to particulate solids.[70,100]

6.2.3 Proposed Adaptations to Original Parameters

In light of the preceding discussions, a number of changes are proposed to improve the accuracy of the DEM modelling, which mostly hinges on controlling percolation rates and its mechanisms.

Since percolation depends on particle size, choosing a properly descriptive particle size distribution is important. A laser diffraction particle analyzer (Mastersizer 3000, Malvern Panalytical) was used to evaluate the full PSD of both FFM and CM. While FFM is well represented by varying ±10% about the mean size and assuming a normal PSD (as was done in Parts I and II), CM has a broader distribution of particle sizes (Fig. 6.6); to better represent it, a wider range of upper and lower values (indicated in the CM curve) was chosen. Shaded regions of the graph indicate the range of sizes that each value are meant to represent, and by numerically integrating their areas the mass percentage of each was calculated. Finally, all three sizes had their material properties set individually, thus allowing for finer control of their behaviour.

Clumping due to cohesion is another mechanism by which segregation is prevented, as it combines particles to create a larger "effective size", more difficult to penetrate into gaps. CM particles were further upscaled 1.5x (by radius), partly to account for cohesive clumping and partly to artificially correct percolation. It should be noted that the cohesive model does create clumps in simulation; the advantage of upscaling is correcting for the lack of finer particles that

are not simulated, as well as reducing overall mixture cohesiveness (an important factor which will be better explored later).

The final, and perhaps less orthodox, modification is the use of CM-to-FFM adhesion to account for particle shape, based on the observations that (A) particle interlocking causes a reduction in segregation rate; (B) there is a dependency on particle orientation for gap penetration (Fig. B.2) and (C) rolling friction, in this particular situation, is a poor proxy for shape. Experimental observations suggest there is little to no real attraction between both materials, so that the inclusion of adhesion is a purely artificial device. Adhesion models particle shape by sticking together both materials as if interlocked or attempting to cross a gap which should be realistically too narrow. Moreover, it aids interpenetration in the first mixing mechanism and prevents segregation in the second, as FFM is bound to CM and thus unable to roll separately.

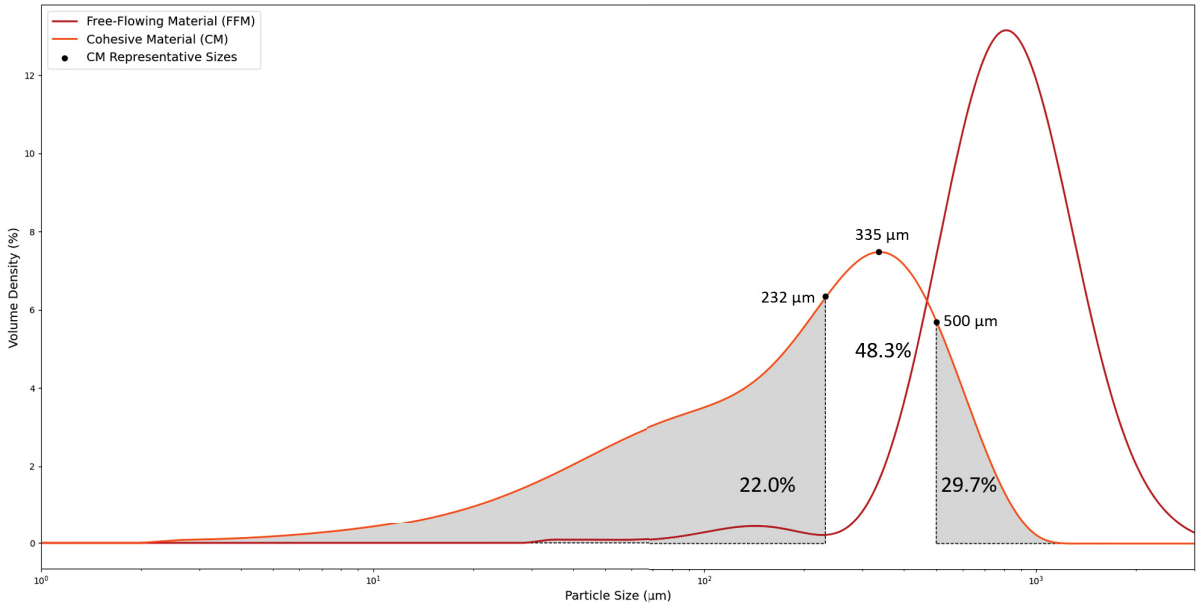

Figure 6.6: Particle Size Distributions for FFM (Red) and CM (Orange). Particle sizes chosen to model the wide distribution of CM are marked as black dots, while shaded areas indicate the size percentages that the above points represent. Plotted in logarithmic scale.

6.3 SIMULATION RESULTS WITH ADHESIVE PARAMETERS

The main simulation parameters that differ between all five simulated mixtures are presented in Table 6.3, with their experimental counterparts in parentheses. IBB geometry was upscaled by 5x in all directions, which increases its volume by 5^3; thus, the experimental mass has to be increased by the same factor. Since experimental filling amount was fixed by total mass, and the same approach taken in simulations, fill percentages were somewhat different from the experimental cases, as a consequence of distinct packing behaviours between real and the idealized spherical particles. However, it should be noted that real fillings were estimated based on uncompressed bulk density, and it is possible values are over-reported. Rotational speeds were adjusted to match experimental Froude numbers by Equation 5.1. When referring to mixtures, the "nominal", experimental parameters are used hereafter.

As a first attempt, it is interesting to demonstrate that using clumping and readjustment of PSD alone is insufficient to improve simulated results to a satisfactory degree, and thus justify the inclusion of adhesion. As in Section 6.2, Mixture 1 is simulated to compare both approaches.

	Mass (kg)	Fill Percentage	RPM
Mixture 1	313 (2.5)	50% (60%)	6.71 (15)
Mixture 2	313 (2.5)	50% (60%)	4.47 (10)
Mixture 3	313 (2.5)	50% (60%)	8.94 (20)
Mixture 4	250 (2.0)	45% (45%)	6.71 (15)
Mixture 5	375 (3.0)	57% (70%)	6.71 (15)

Table 6.3: Simulation parameters for all five mixtures, based on Table 6.4 and adjusted for CGM. The original, experimental parameters are reproduced between parentheses for comparison.

Figure 6.7(A) displays final simulation states with adjusted particle sizes only, showing the big CM particles (green) well distributed whilst smaller sizes (both coloured red) have the same tendency to core segregation. Furthermore, CM quantification from top to bottom was 22.0%, 34.4% and 23.2% (*versus* 46.7% / 33.1% / 23.7% in the first attempt), an improvement due to the proposed modifications; yet, top and bottom points were still relatively devoid of CM due to de-mixing.

Contrary to the above discussion, in which some segregation is observed, Fig. B.5 shows a stable net mixing index (dashed lines), in contrast to the first attempt from Section 6.2 (reproduced here with dotted lines). This is attributable to large CM particles getting better distributed over time, inversely to the segregative phenomena for smaller particles. The solid line presents the correctly calibrated Mixture 1 (with parameters discussed below) for comparison purposes.

Nevertheless, changes to particle sizes alone do not correctly predict experimental mixtures, and the adhesive parameter is needed. Of the original calibrated parameters, two were kept (static friction and CM cohesion, which was extended to all three CM sizes). Rolling friction was maintained at 0.06 for the middle CM size (which is equal to the non-clumped average size in Part II), while it was increased to 0.09 for the larger particles and reduced to 0.01 for the smaller particles, since different sizes aim to model different breakage states.

After extensive trial-and-error, an adhesion parameter of 1 was calibrated for all CM sizes; despite being equal, this coefficient manifests itself differently for the three particle sizes, since (as per Section 5.2.3) the cohesion model is scale-dependant. Figure 6.7(B) shows the state of the adhesive Mixture 1 simulation. Compared to (A), CM is clearly better distributed, indicating some reversal of the segregative mechanism.

Table 6.4 presents calibrated sampling results for all five mixtures in simulation; values in parenthesis are percentage point differences between reported and experimental results (Table 6.1). In all cases, and in all points, results were within 10% of experimental CM quantities. However, the exact pattern has not been achieved for some simulations. For instance, Mixture 3 had increasing CM quantities from top to bottom in the experimental results, while its simulation showed a decrease in the same direction. This can be attributed to experimental sampling variability, which is reflected in the reported standard deviations.

Finally, the global mixing indices for the five calibrated mixtures are presented in Fig. 6.8. The "central" Mixture 1 is plotted in black, while the RPM-varying cases are plotted in orange and the fill percentage mixtures are green. A discussion on the effects both parameters have on mixing is provided below.

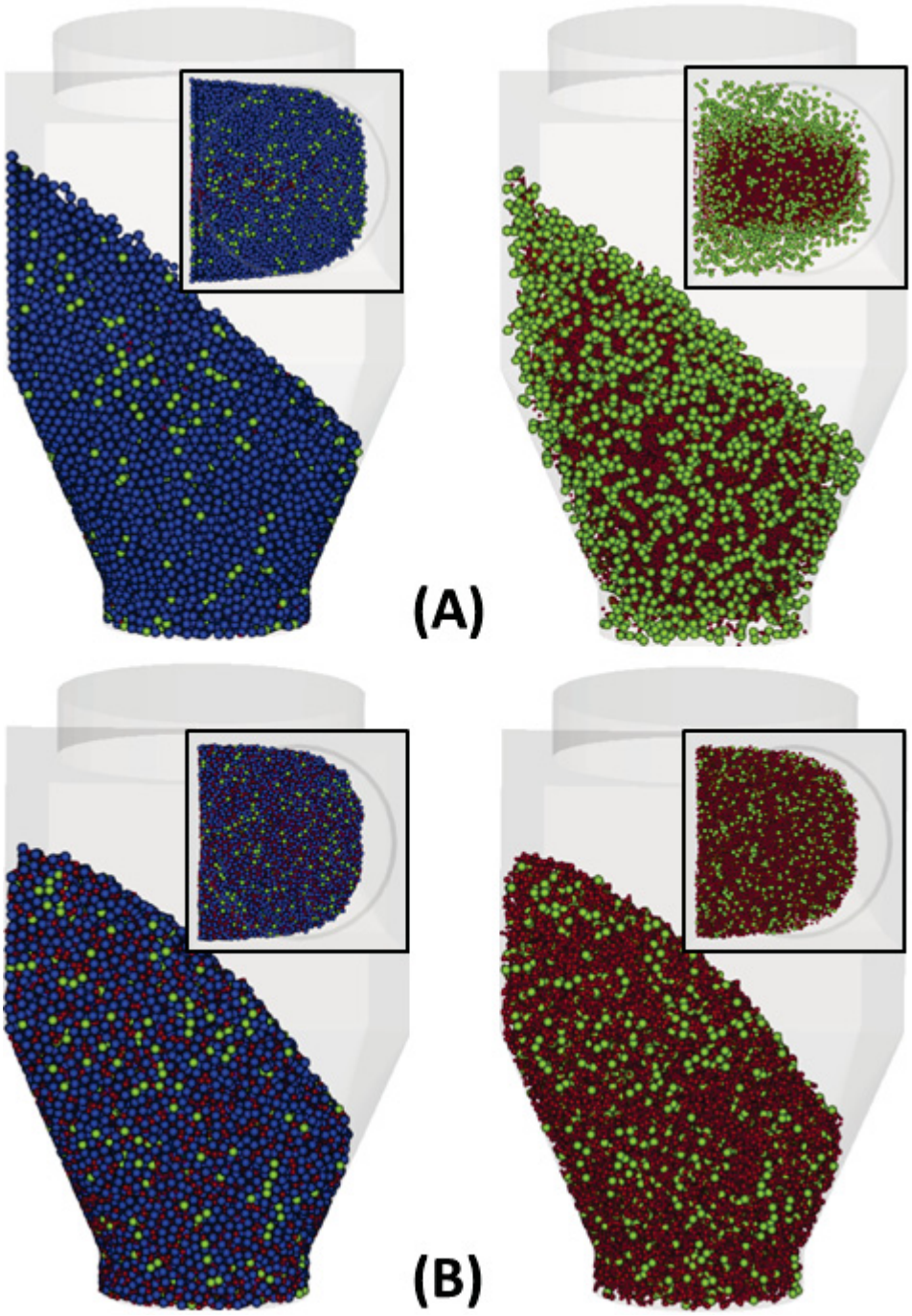

Figure 6.7: Simulation results (at 300 seconds) using readjusted particle sizes, with and without FFM (blue) visible. Insets show the IBB viewed from the top. In (A) the parameters calibrated in Parts I and II were used; without the inclusion of adhesion, the biggest CM particles (green) are well distributed, while the other two smaller sizes (red) show preferential core segregation. With an adhesive parameter between FFM and CM (B), mixing is greatly improved and there is no clear separation between CM sizes.

6.3.1 Effects of RPM

Rotation speed has an obvious effect on mixing rate, as can be clearly seen in Fig. 6.8: the 10-RPM case has a much slower climb towards steady state than its 15 and 20 RPM counterparts. Interestingly, however, Mixtures 1–3 arrive at a similar final mixing index, suggesting little impact on mixing performance. This seemingly goes against the rotating drum BNE discussion

	Top	Middle	Bottom
Mixture 1	31.88% (-1.93 pp)	30.69% (2.49 pp)	30.43% (-1.88 pp)
Mixture 2	32.23% (2.25 pp)	30.92% (-1.82 pp)	29.63% (-1.12 pp)
Mixture 3	31.50% (0.42 pp)	30.21% (-0.90 pp)	29.90% (-2.20 pp)
Mixture 4	31.10% (-3.40 pp)	29.38% (-2.37 pp)	30.78% (-1.89 pp)
Mixture 5	32.47% (-0.76 pp)	30.91% (-0.66 pp)	28.95% (0.86 pp)

Table 6.4: Results for all simulated IBB runs, in terms of the cohesive material percentage at all three sampling points. In parentheses are listed the differences between values on the left and the corresponding experimental result from Table 6.1.

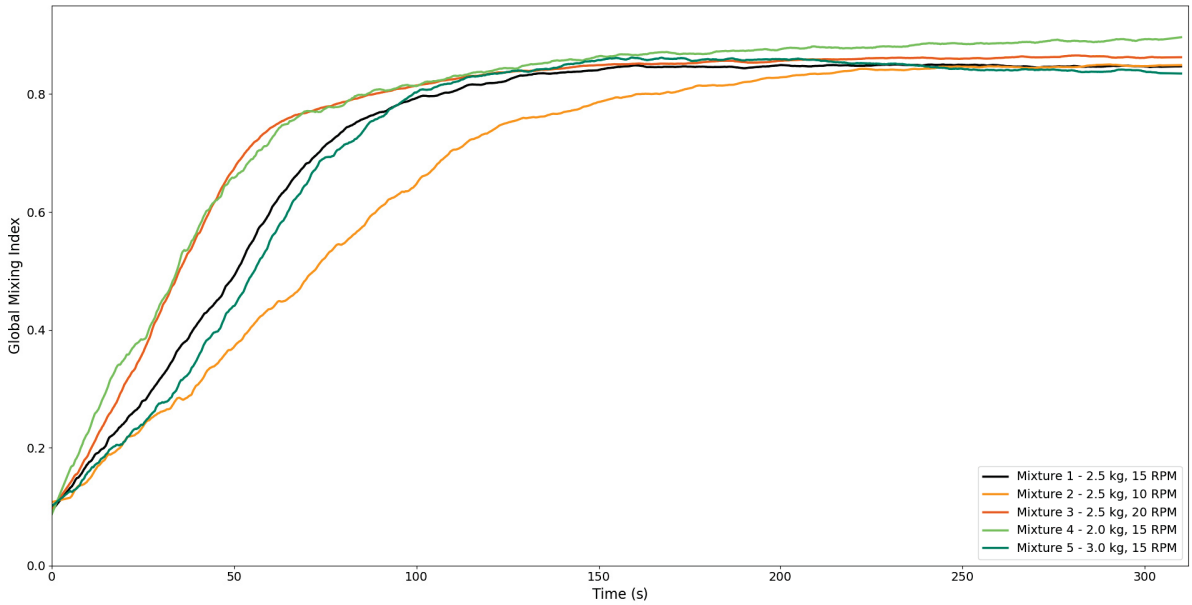

Figure 6.8: Global mixing indices for all five calibrated mixtures. Mixtures 2 and 3, which have varied rotational speeds, are displayed in orange; Mixtures 4 and 5, in green, have varying fill heights.

in Section 6.1.1, in which it was argued that rotational/centrifugal forces were key in explaining differences in experimental results.

In the rotating drum calibrations of Part II, two approaches to upscaling were explored: maintaining a constant Froude number across all scales by proportionally reducing RPMs (or "Froude-adjusted"); and a "Fixed-RPM" approach, in which the respective rotation speeds were kept constant (thus increasing Froude numbers on higher scales), the underlying logic being that number of revolutions is the key controlling variable in mixing.[77–79] The latter resonates with preceding discussions on the mechanisms of IBB mixing, as most of them revolved around particle behaviour during a given revolution.

In Figure 6.9, the mixing index curves for mixtures 1 to 3 (as shown in Fig. 6.8) are redrawn as a function of number of revolutions instead of time. By doing so, differences in their behaviours are practically eliminated, suggesting that mixing state is mostly dependant on revolution numbers.

A final attempt, at nominal 20 RPM, is also shown in Fig. 6.9. This choice of speed is convenient for two reasons: it enables an adjusted *versus* non-adjusted speed comparison for Mixture 3, since 20 RPM was its true experimental parameter; and it provides an attempt at high speeds – it is equivalent to an experimental run at approximately 45 RPM. The resulting curve

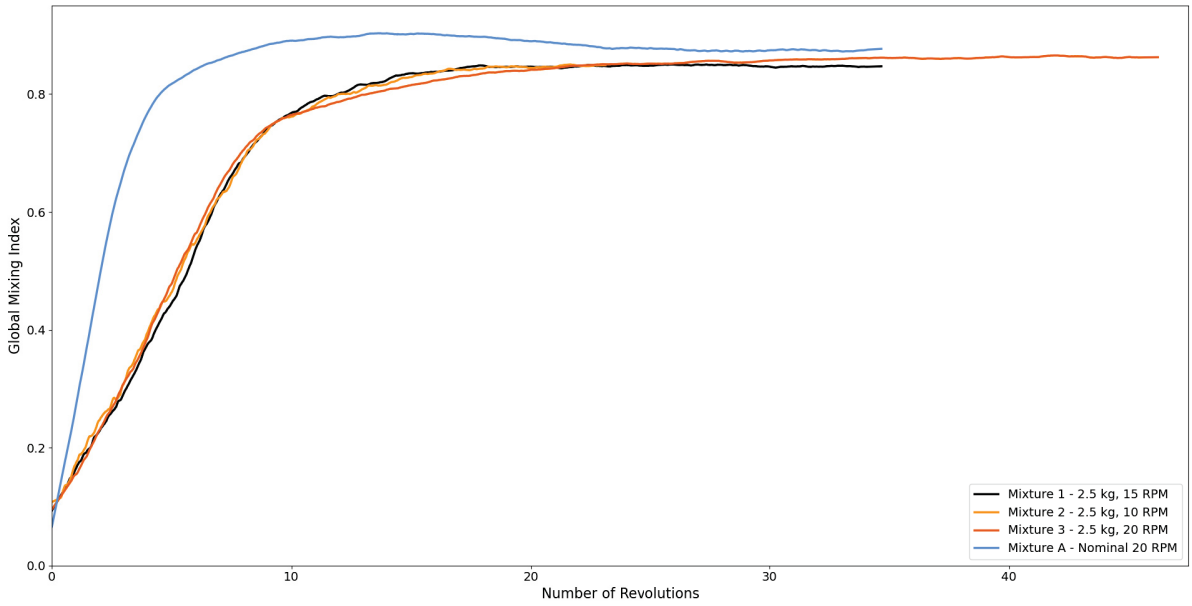

Figure 6.9: Global mixing indices for calibrated mixtures with varying rotational speeds; Mixtures 1 to 3 are reproduced from Fig. 6.9 as functions of number of revolutions. Mixture A uses a nominal (i.e. not scaled by Froude number) 20 RPM speed. Mixing performance is highly dependant on number of revolutions, but higher speeds can cause deviations from that pattern.

from Mixture A shows a large deviation from all other runs, attributable to the increased forces (centrifugal or otherwise) to which particles are subjected. The number of revolutions alone is insufficient as a parameter for upscaling; likewise, the Froude number is arguably incomplete, as only centripetal forces (and not those produced by the IBB's own geometry while lifting material) are taken into account. A number of parameters have to be considered when upscaling such experiments, but it has been demonstrated that, for lower speeds, results are largely invariant with its choice.

6.3.2 Effects of Filling Percentages

Mixture 4 outperforms all others in terms of final homogeneity, and its progress over time closely matches the 20-RPM case; increases in mixing efficiency due to bigger headspaces are attributable to particles having more freedom of movement, thus promoting dispersion.[101,102] Compared to Mixtures 1 and 3, the same final mixing indices were achieved at 127 and 148 seconds, respectively. By a reduction of only 20% in IBB charge, the same mixing quality is attained at less than half the time, which is more efficient in terms of multiple batches in an industrial process.

Figure 6.10 shows total power dissipated by the "dashpot" parts of normal and tangential force modelling for all mixtures in a single steady-state revolution; it serves as an approximation of IBB power consumption, with the caveat that spherical particles tend to underestimate energy requirements.[103] It is therefore better understood, and more useful, as a qualitative comparison for all mixtures. Mixtures 2 and 3 were reescaled to match this particular revolution, by the same procedure adopted to plot mixing indices as functions of number of revolutions.

The insets at the top show IBB positions over time, and it is noteworthy that energy peaks occur in the horizontal-to-vertical transitions (i.e. when the material is allowed to free-fall) rather than the vertical-to-horizontal transition, when solids are lifted and should, theoretically, draw more power. This happens because falling particles are imprinted with higher velocities,

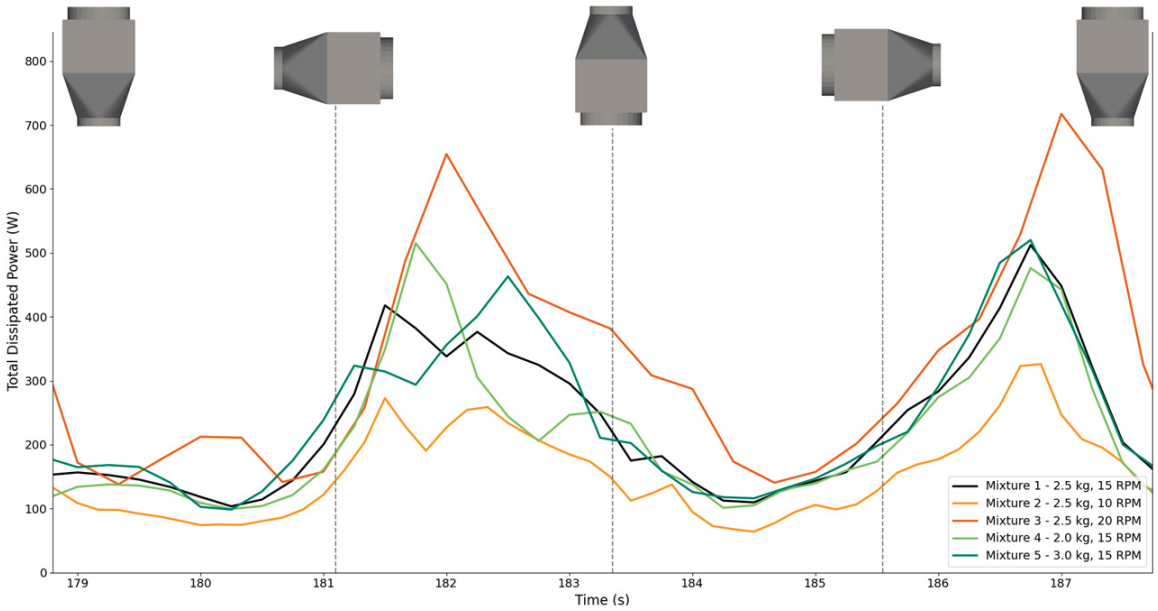

Figure 6.10: Total Dissipated Power by all mixtures during the twenty-first revolution (times in Mixtures 2 and 3 were rescaled to match other cases). Dissipation by normal and tangential forces are a reasonable estimate of real power consumption, although underestimated in spherical simulations. Insets show IBB positions related to their respective points in time.

thus increasing their normal overlap and, by consequence, more energy is dissipated. Figure 6.10 is hence "out-of-phase" with experimental expectations, but conservation of energy dictates the overall behaviour is the same.

Variations in rotational speed have a directly proportional effect on power draw; increases in RPM (such as in Mixture 3) increase energy consumption and vice-versa (Mixture 2). For cases in which RPM is maintained and IBB charge was varied, a similar pattern is to be expected: lower amounts of material means less power needs to be invested in moving the equipment. For Mixture 4, however, the peak between 181 and 183 seconds was highest among mixtures of different masses. Since, as previously discussed, peaks were controlled by material free-fall, it further implies a change in particle dynamics due to the alterations in total mass (Fig. B.6 extends the above figure to more revolutions, showing the same pattern regularly occurring).

Relative to Mixture 1, the average power consumption (for the full 300 second simulations) is 65% and 138% for Mixtures 2 and 3, respectively, while for Mixtures 4 and 5 it is 92% and 103%. It further reinforces Mixture 4 as optimal, since gains in mixing efficiency are accompanied by smaller energy requirements as well.

Another important consideration is particle breakage due to the impact forces to which they are subjected. Peaks in Fig. 6.10 are indicative of differences in particle velocity profiles, which should increase particle fragmentation. Figure 6.11 presents histograms of shear energy accumulated by particles at the end of mixing; if a given particle exceeds its material's energy threshold, it breaks into smaller units.[104] For each mixture, histograms of FFM and CM are presented separately, showing differences in how energy is split between materials due to varied operational parameters.

The added rotational speeds in Mixture 3 cause more shearing, either by higher velocities inside the IBB or by having more revolutions (if compared to Mixtures 1, 4 and 5). The added breakage in Mixture 4, postulated from the dissipated power analysis, is also perceptible when compared to Mixture 1. When considered together, both analyses show that larger headspaces aid mixing by providing more space and freedom for particle mixing, at the cost of higher velocities –

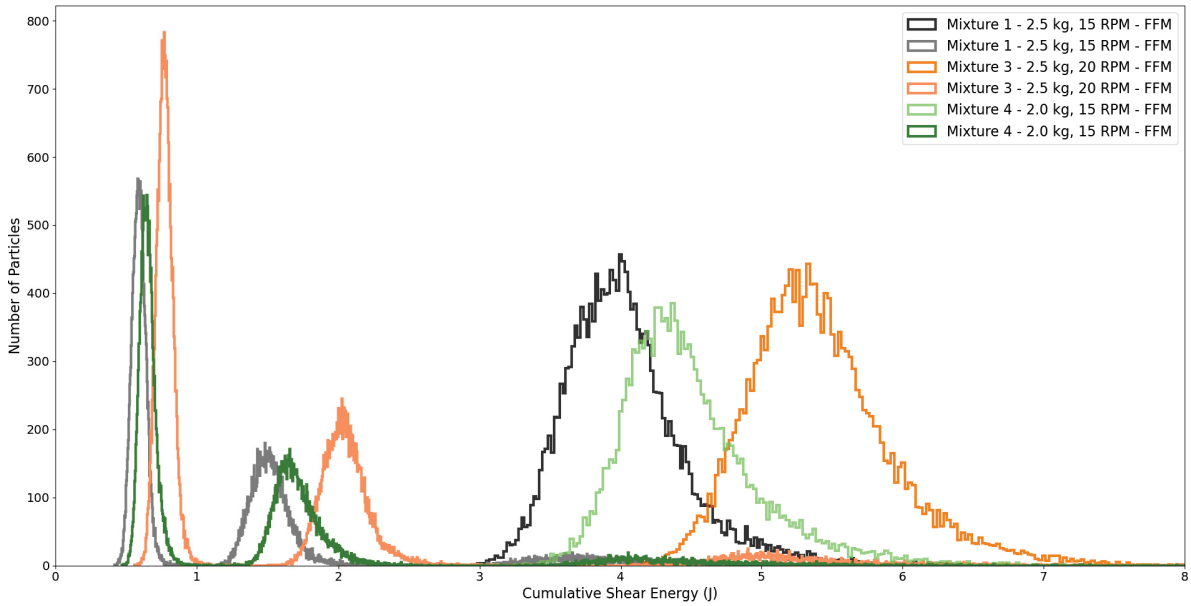

Figure 6.11: Accumulated particle shear energy histograms for Mixtures 1, 3 and 4 at 300 seconds, which is related to particle breakage. Average damage is highest for Mixture 3 due to higher rotational speeds. The increased headspace in Mixture 4, due to lower amounts of material, causes more breakage if compared to Mixture 1.

and, thus, more particle damage – developed inside the IBB. Consideration must be given to fragmentation when its energy threshold is surpassed; as particles subdivide into smaller units, the dynamics of mixing, and its end results, may be fundamentally altered.

6.4 PRELIMINARY ATTEMPTS WITH POLYHEDRAL SIMULATIONS

Polyhedral particles should remove the need for "excessive" adhesive parameters, as shape is correctly taken into account inside the DEM modelling. However, choice of particle shape, specially in the highly polydisperse cases such as the one presented here, becomes key in correctly modelling experimental behaviour. Figure 6.12 presents first attempts (such as done in 6.2) using originally calibrated parameters for Mixture 1, but with CM sizes and PSD readjusted. Moreover, the cubic shapes were maintained from Parts I and II, except for the largest and smallest CM sizes: they were respectively changed to cuboids (aspect ratio 1.5) and triangular orthobicupolas, based on microscope observations of their approximate shape.

Compared to Fig. 6.7, in which the above alterations were introduced with and without adhesion, the overall pile shape and CM distribution is much closer to the adhesive case in (B), which suggests adhesion does, in fact, model shape to a respectable degree. However, quantification of CM yields, from top to bottom, 35.99%, 32.07% and 23.24% in the polyhedral case. Further adjustments to parameters and particle shapes must be carried out in order to better model experimental observations.

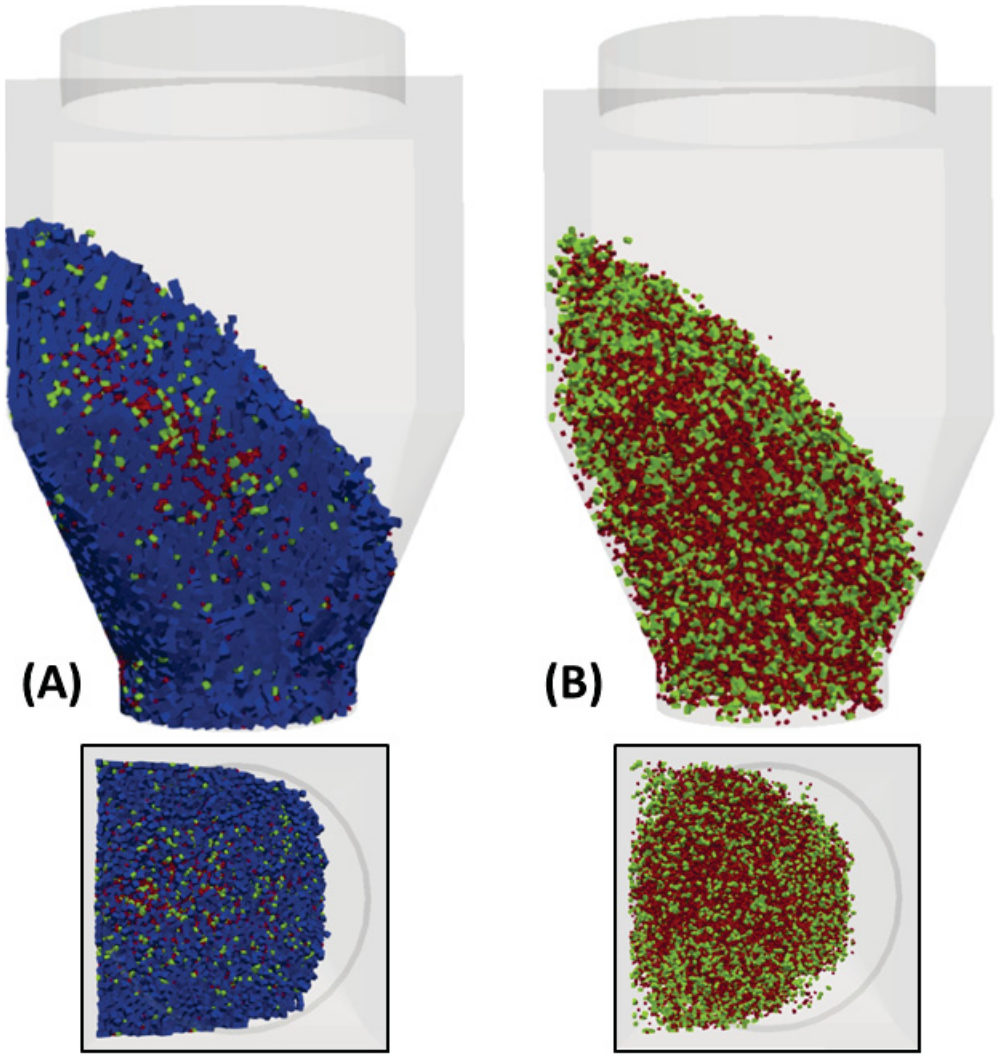

Figure 6.12: Polyhedral simulation results for Mixture 1, using readjusted particle sizes, with and without FFM (blue) visible. Insets show the IBB viewed from the top.

7 CONCLUSIONS

The Discrete Element Method (DEM) was successfully employed to calibrate – to obtain a set of frictional parameters, the static and the artificial rolling damping – for two powdered materials, one of which classed as cohesive. To this end, a series of experiments in which solids come at rest at a defined angle, the Angle of Repose (AoR), were performed; calibration entails reproducing these AoRs on simulations by successive guessing of parameters until simulations and experiments match, and it was done for real-shaped polyhedral particles and then compared to their spherical counterpart. A Coarse Grain Model (CGM) of the real-sized particles was used, where particles are grouped into larger grains 30 times the size of the original particles. Then, to verify the limits and validity of CGM, simulations at larger (40x) and smaller (20x, 10x, 5x and the real-sized 1x) scales were run.

On the ledge test, a simple experiment consisting of restraining solids on a small box and then removing one of the walls (thus permitting material outflow), there is good agreement between experiments and simulations. For the larger-sized free-flowing material in Part I, however, upscaling beyond 30x causes a critical increase in particle mass, which was shown to raise AoRs for polyhedral particles. In Part II, the effects of cohesion were demonstrated to be minimal for this particular test.

The rotating drum is special in the sense that it provides a dynamic angle of repose, thus being important in calibrating particles in motion. Unlike the ledge test, results for the cohesionless case in Part I were consistent for larger scales, but for smaller sizes there is a sizeable drop in AoR for polyhedral simulations. This is attributable to particle weight and shape, since smaller cubic particles suffer more rearranging due to drum movement and their interlocking decreases the AoR. The introduction of cohesion in Part II caused a larger disparity between experimental and simulated results, as the cohesive force law here used is not size-invariant; parameters calibrated at 30x scale caused excessive cohesion at smaller scales. Moreover, the Froude number as a scaling parameter was further explored and compared to a "constant number of revolutions" approach, in which rotational speeds were kept equal across all scales. Flow regime, independent of choice of scaling parameter, was shown to be the main parameter influencing results.

Finally, mixtures of both materials, with varying rotational speeds and fill percentages, were carried out to test the predictive capabilities of calibration. Five mixtures, on a 70/30 split between FFM (the free-flowing material in Part I) and CM (the cohesive material from Part II) were produced in a lab-scale In-Bin Blender (IBB), with speeds ranging from 10 to 20 RPM and total mass – used as a proxy for fill percentage – from 2.0 to 3.0 kg. At 30x particle scaling, and using spherical particles, DEM simulations of the above mixtures were unable to reproduce experimental findings when previously calibrated parameters and assumptions were used. Main DEM parameters (both friction coefficients and cohesion) were systematically modified in an attempt to better approximate simulated and experimental results. The resulting simulations were unable to do so; however, they were useful in understanding IBB mixing dynamics for a polydisperse mix. Two mechanisms were proposed: in the beginning, the initially separated particles diffuse through each other by a relatively small interface, created by the free-falling motion characteristic of IBBs; this mechanism is largely influenced by the AoR, that "traps" particles and subdues interface creation. The second mechanism is again induced by free-fall, but causes sifting segregation due to the large particle size ratios under a velocity gradient.

Based on the above observations, a number of adjustments were proposed, such as particle clumping and improvements to CM particle size distribution; the biggest improvement, however, was achieved by using a FFM-CM adhesive parameter to correct for the lack of particle shape. By artificially creating attraction between both materials, rates of segregation in the second mechanism are reduced by mimicking particle interlocking. All five mixtures were then succesfuly reproduced within a 10% range of experimental quantifications. In the RPM-varying cases (which were adjusted to match experimental Froude numbers), rotational speeds had an obvious influence on mixing speed; when mixing index plots were readjusted to number of revolutions, however, all mixtures behaved approximately the same. Hence, at low rotational speeds, the total number of revolutions is the key parameter that controls mixing. The lowest fill mixture had the best results in terms of mixing speed and final quality, owing to a larger headspace that provides more ample room for diffusion to occur; the drawback is an increase in particle breakage, which has to be considered in the operation of a real IBB.

Overall, it has been demonstrated that particle shape is an important parameter that the rolling friction coefficient cannot quite capture. Furthermore, the Angle of Repose, which is extensively used to characterize bulk behaviour, is imprecise when large size ratios and cohesive particles are concerned, as percolation *phenomena* are not captured by its experiments.

REFERENCES

[1] Daisuke Nishiura, Mikito Furuichi, and Hide Sakaguchi. Real-scale DEM simulations on the fault evolution process observed in sandbox experiments. *Advanced Powder Technology*, 32(11):4432–4441, 2021.

[2] Top 500. Earth Simulator -SX-Aurora TSUBASA - SX-Aurora TSUBASA B401-8, Vector Engine Type20B 8C 1.6GHz, Infiniband HDR200. `https://www.top500.org/system/179927/`, 2022. Acessado em 04/07/2022.

[3] Top 500. K computer, SPARC64 VIIIfx 2.0GHz, Tofu interconnect. `https://www.top500.org/system/177232/`, 2022. Acessado em 04/07/2022.

[4] Dr. Donald Kinghorn. AMD Threadripper 3990x 64-core Linpack and NAMD Performance (Linux). `https://www.pugetsystems.com/labs/hpc/AMD-Threadripper-3990x-64-core-Linpack-and-NAMD-Performance-Linux-1666/`, 2020. Acessado em 05/07/2022.

[5] Xiaowei Weng. Modeling of complex hydraulic fractures in naturally fractured formation. *Journal of Unconventional Oil and Gas Resources*, 9, 09 2014.

[6] Vinicius Daroz. ESSS Rocky's 200 million particle simulation on Oracle Cloud pushes DEM analysis to a new height. `https://rocky.esss.co/blog/rocky-200-million-particle-simulation-on-oracle-cloud/`, 2022. Acessado em 03/08/2022.

[7] Nicolin Govender, Daniel N. Wilke, and Schalk Kok. Blaze-demgpu: Modular high performance dem framework for the gpu architecture. *SoftwareX*, 5:62–66, 2016.

[8] C. Bierwisch, T. Kraft, H. Riedel, and M. Moseler. Three-dimensional discrete element models for the granular statics and dynamics of powders in cavity filling. *Journal of the Mechanics and Physics of Solids*, 57(1):10–31, 2009.

[9] MD Skogen, Rubao Ji, Anna Akimova, Ute Daewel, Cecilie Hansen, SS Hjøllo, Sonja van Leeuwen, Marie Maar, Diego Macías, Erik Mousing, Elin Almroth-Rosell, Sevrine Sailley, MA Spence, TA Troost, and K.E. Van de Wolfshaar. Disclosing the truth: Are models better than observations? *Marine Ecology Progress Series*, DYNMOD, 01 2020.

[10] P. A. Cundall and O. D.L. Strack. A discrete numerical model for granular assemblies. *Geotechnique*, 1979.

[11] Shaojun Liu, Yuanwen Li, and Xiaozhou Hu. Effect of Particle Volume Fraction on the Performance of Deep-sea Mining Electric Lifting Pump Based on DEM-CFD. *Jixie Gongcheng Xuebao/Journal of Mechanical Engineering*, 2020.

[12] Bayisa Regassa, Nengxiong Xu, and Gang Mei. An equivalent discontinuous modeling method of jointed rock masses for DEM simulation of mining-induced rock movements. *International Journal of Rock Mechanics and Mining Sciences*, 2018.

[13] Józef Horabik and Marek Molenda. Parameters and contact models for dem simulations of agricultural granular materials: A review. *Biosystems Engineering*, 147:206–225, 07 2016.

[14] Jidong Zhao and Tong Shan. Coupled CFD-DEM simulation of fluid-particle interaction in geomechanics. *Powder Technology*, 2013.

[15] Hermann Kureck, Nicolin Govender, Eva Siegmann, Peter Boehling, Charles Radeke, and Johannes G. Khinast. Industrial scale simulations of tablet coating using GPU based DEM: A validation study. *Chemical Engineering Science*, 2019.

[16] Ju Eun Kim and Young Mi Chung. CFD-DEM Simulation of the Fluidized-bed Granulation of Food Powders. *Biotechnology and Bioprocess Engineering*, 2019.

[17] Jesica D. Oroná, Susana E. Zorrilla, and Juan M. Peralta. Computational fluid dynamics combined with discrete element method and discrete phase model for studying a food hydrofluidization system. *Food and Bioproducts Processing*, 2017.

[18] Jannatul Azmir, Qinfu Hou, and Aibing Yu. CFD-DEM simulation of drying of food grains with particle shrinkage. *Powder Technology*, 2019.

[19] R. Berger, C. Kloss, A. Kohlmeyer, and S. Pirker. Hybrid parallelization of the liggghts open-source dem code. *Powder Technology*, 278:234–247, 2015.

[20] Andriarimina Daniel Rakotonirina and Anthony Wachs. Grains3d, a flexible dem approach for particles of arbitrary convex shape - part ii: Parallel implementation and scalable performance. *Powder Technology*, 324:18–35, 2018.

[21] Eun Hyun Park, Volodymyr Kindratenko, and Youssef M.A. Hashash. Shared memory parallelization for high-fidelity large-scale 3d polyhedral particle simulations. *Computers and Geotechnics*, 137:104008, 2021.

[22] Daniel Nasato, Christoph Goniva, Stefan Pirker, and Christoph Kloss. Coarse graining for large-scale dem simulations of particle flow – an investigation on contact and cohesion models. *Procedia Engineering*, 102:1484–1490, 12 2015.

[23] Alberto Di Renzo, Erasmo Napolitano, and Francesco Maio. Coarse-grain dem modelling in fluidized bed simulation: A review. *Processes*, 9:279, 02 2021.

[24] D.R.J. Owen and Jeffery Loughran. On upscaling of discrete element models: Similarity principles. *Engineering Computations: Int J for Computer-Aided Engineering*, 26:599–609, 08 2009.

[25] Thomas Roessler and André Katterfeld. Scaling of the angle of repose test and its influence on the calibration of dem parameters using upscaled particles. *Powder Technology*, 330, 05 2018.

[26] Jakub Hlosta, Lucie Jezerská, Jiří Rozbroj, David Žurovec, Jan Necas, and Jiří Zegzulka. Dem investigation of the influence of particulate properties and operating conditions on the mixing process in rotary drums: Part 2-process validation and experimental study. *Processes*, 8:184, 02 2020.

[27] P. A. Cundall and O. D. L. Strack. A discrete numerical model for granular assemblies. *Geotechnique*, 29(1):47–65, 1979.

[28] B.K. Mishra and Raj K. Rajamani. Simulation of charge motion in ball mills. part 1: experimental verifications. *International Journal of Mineral Processing*, 40(3):171–186, 1994.

[29] Li li WANG. Chapter 6 - one-dimensional visco-elastic waves and elastic-visco-plastic waves. In Li li WANG, editor, *Foundations of Stress Waves*, pages 219–264. Elsevier, Oxford, 2007.

[30] Su Bin Yeom, Eun-Sol Ha, Min-Soo Kim, Seong Hoon Jeong, Sung-Joo Hwang, and Du Hyung Choi. Application of the discrete element method for manufacturing process simulation in the pharmaceutical industry. *Pharmaceutics*, 11(8), 2019.

[31] Nicolin Govender, Daniel N. Wilke, Patrick Pizette, and Nor-Edine Abriak. A study of shape non-uniformity and poly-dispersity in hopper discharge of spherical and polyhedral particle systems using the blaze-dem gpu code. *Applied Mathematics and Computation*, 319:318–336, 2018. Recent Advances in Computing.

[32] Alberto M. Puga, Nicolin Govender, and Raj K. Rajamani. Verification of polyhedral dem with laboratory grinding mill experiments. *KONA Powder and Particle Journal*, 39:208–218, 2022.

[33] K. L. Johnson. *Normal contact of elastic solids - Hertz theory*, pages 84–106. Cambridge University Press, 1985.

[34] Zilin Yan, Sam Wilkinson, E. Stitt, and M. Marigo. Discrete element modelling (dem) input parameters: understanding their impact on model predictions using statistical analysis. *Computational Particle Mechanics*, 2:1–17, 07 2015.

[35] Adina Negrea and Mihai Predoi. The elastic contact of a sphere with an elastic half-space, a comparision between analytical and finite element solutions. *Scientific Bulletin. Series A: Applied Mathematics and Physics. Politehnica University of Bucharest*, 74, 01 2012.

[36] Nicolin Govender, Patrick Pizette, Daniel Wilke, and Nor-Edine Abriak. Validation of the gpu based blaze-dem framework for hopper discharge. In *IV International Conference on Particle-based Methods - Fundamentals and Applications PARTICLES 2015*, 08 2015.

[37] Daniel Queteschiner, Thomas Lichtenegger, Simon Schneiderbauer, and Stefan Pirker. Adaptive coarse-graining for large-scale dem simulations. In *12th International Conference on Computational Fluid Dynamics in the Oil & Gas, Metallurgical and Process Industries*, 05 2017.

[38] K L Johnson. One hundred years of hertz contact. *Proceedings of the Institution of Mechanical Engineers*, 196(1):363–378, 1982.

[39] Mingjing Jiang, Zhifu Shen, and Jianfeng Wang. A novel three-dimensional contact model for granulates incorporating rolling and twisting resistances. *Computers and Geotechnics*, 65:147–163, 2015.

[40] F.P. Di Maio and A. Di Renzo. Modelling particle contacts in distinct element simulations: Linear and non-linear approach. *Chemical Engineering Research and Design*, 83(11):1287–1297, 2005.

[41] Loc Vu-Quoc, Xiang Zhang, and Lee Lesburg. Normal and tangential force-displacement relations for frictional elasto-plastic contact of spheres. *International Journal of Solids and Structures - INT J SOLIDS STRUCT*, 38:6455–6489, 09 2001.

[42] Alberto Di Renzo and Francesco Paolo Di Maio. Comparison of contact-force models for the simulation of collisions in dem-based granular flow codes. *Chemical Engineering Science*, 59(3):525–541, 2004.

[43] Jonathan Fleischmann, Radu Serban, Dan Negrut, and Paramsothy Jayakumar. On the importance of displacement history in soft-body contact models. *Journal of Computational and Nonlinear Dynamics*, 11, 08 2015.

[44] R. D. Mindlin and H. Deresiewicz. Elastic Spheres in Contact Under Varying Oblique Forces. *Journal of Applied Mechanics*, 20(3):327–344, 06 1953.

[45] Kazuyoshi Iwashita and Masanobu Oda. Micro-deformation mechanism of shear banding process based on modified distinct element method. *Powder Technology*, 109(1):192–205, 2000.

[46] C.M. Wensrich and A. Katterfeld. Rolling friction as a technique for modelling particle shape in dem. *Powder Technology*, 217:409–417, 2012.

[47] Changhua Xie, Huaqing Ma, and Yongzhi Zhao. Investigation of modeling non-spherical particles by using spherical discrete element model with rolling friction. *Engineering Analysis with Boundary Elements*, 105:207–220, 08 2019.

[48] André Katterfeld, C.J. Coetzee, Tim Donohue, Johannes Fottner, Andrew Grima, Álvaro Ramírez-Gómez, Dusan Ilic, Rimantas Kacianauskas, Jan Necas, Dingena Schott, Kenneth Williams, and Jiri Zegzulka. Calibration of dem parameters for cohesionless bulk materials under rapid flow conditions and low consolidation. Technical report, 07 2019.

[49] Radek Dubina and Jan Eliáš. Effect of rolling resistance in dem models with spherical bodies. *Transactions of the VŠB - Technical University of Ostrava Civil Engineering Series*, 16, 12 2016.

[50] Jun Ai, Jian-Fei Chen, J. Rotter, and J. Ooi. Assessment of rolling resistance models in discrete element simulations. *Powder Technology*, 206:269–282, 01 2011.

[51] Behzad Soltanbeigi, Alexander Podlozhnyuk, Christoph Kloss, Stefan Pirker, J. Ooi, and Stefanos-Aldo Papanicolopulos. Influence of various dem shape representation methods on packing and shearing of granular assemblies. *Granular Matter*, 23:26, 05 2021.

[52] Kazuyoshi Iwashita and Masanobu Oda. Rolling resistance at contacts in simulation of shear band development by dem. *Journal of Engineering Mechanics*, 124:285–292, 3 1998.

[53] N.V. Brilliantov and T. Pöschel. Rolling friction of a viscous sphere on a hard plane. *Europhysics Letters*, 42(5):511 – 516, 1998.

[54] Yihong Qiu, Yisheng Chen, Geoff Zhang, L. Liu, and William Porter. *Developing Solid Oral Dosage Forms*. Elsevier, 01 2009.

[55] Xin Li, Qinfu Hou, Kejun Dong, Ruiping Zou, and Aibing Yu. Promote cohesive solid flow in a screw feeder with new screw designs. *Powder Technology*, 361:248–257, 2020.

[56] Bram Bekaert, L Penne, Wouter Grymonpré, Bernd van snick, Jens Dhondt, J Boeckx, J Vogeleer, Thomas Beer, Chris Vervaet, and Valérie Vanhoorne. Determination of a quantitative relationship between material properties, process settings and screw feeding

behavior via multivariate data-analysis. *International journal of pharmaceutics*, 602:120603, 04 2021.

[57] John Fitzpatrick, Tariq Iqbal, C Delaney, T Twomey, and M.K Keogh. Effect of powder properties on the flowability of milk powders with different fat contents. *Journal of Food Engineering*, 64:435–444, 10 2004.

[58] Thomas Roessler and André Katterfeld. Dem parameter calibration of cohesive bulk materials using a simple angle of repose test. *Particuology*, 45:105–115, 2019.

[59] Luca Orefice and Johannes Khinast. A novel framework for a rational, fully-automatised calibration routine for dem models of cohesive powders. *Powder Technology*, 361, 11 2019.

[60] Vahid Hassanzadeh, Chris M. Wensrich, and Roberto Moreno-Atanasio. Elucidation of the role of cohesion in the macroscopic behaviour of coarse particulate systems using dem. *Powder Technology*, 361:374–388, 2020.

[61] Jamie Clayton. Chapter 17 - an introduction to powder characterization. In Ajit S. Narang and Sherif I.F. Badawy, editors, *Handbook of Pharmaceutical Wet Granulation*, pages 569–613. Academic Press, 2019.

[62] Dewei Xu, Kenneth M. Liechti, and K. Ravi-Chandar. On the modified tabor parameter for the jkr–dmt transition in the presence of a liquid meniscus. *Journal of Colloid and Interface Science*, 315(2):772–785, 2007.

[63] Stefan Luding. Luding s.: Cohesive, frictional powders: contact models for tension. granul. matter 10(4), 235-246. *Granular Matter*, 10:235–246, 06 2008.

[64] Liz Ivoneth Del Cid. *Discrete element methodology for the analysis of cohesive granular bulk solid materials*. PhD thesis, Colorado School of Mines, 2015.

[65] John Morrissey. *Discrete element modelling of iron ore pellets to include the effects of moisture and fines*. PhD thesis, University of Edinburgh, 11 2013.

[66] Alisa Vasilenko, Sara Koynov, Benjamin J. Glasser, and Fernando J. Muzzio. Role of consolidation state in the measurement of bulk density and cohesion. *Powder Technology*, 239:366–373, 2013.

[67] M. Javad Mohajeri, Mats J. van den Bos, Cees van Rhee, and Dingena L. Schott. Bulk properties variability and interdependency determination for cohesive iron ore. *Powder Technology*, 367:539–557, 2020.

[68] K.L. Johnson, Kevin Kendall, and A.D. Roberts. Surface energy and contact of elastic solids. *Proceedings of The Royal Society A: Mathematical, Physical and Engineering Sciences*, 324:301–313, 09 1971.

[69] Wei Chen, Tim Donohue, Kenneth Williams, André Katterfeld, and Thomas Roessler. Modelling cohesion and adhesion of wet, sticky iron ores in discrete element modelling for material handling processes. In *Iron Ore Conference*, 07 2015.

[70] Nicolin Govender, Rafał Kobyłka, and Johannes Khinast. The influence of cohesion on polyhedral shapes during mixing in a drum. *Chemical Engineering Science*, 270:118499, 2023.

[71] Thomas Roessler, Christian Richter, André Katterfeld, and Frank Will. Development of a standard calibration procedure for the DEM parameters of cohesionless bulk materials – part I: Solving the problem of ambiguous parameter combinations. *Powder Technology*, 2019.

[72] Anita Mehta and G. C. Barker. The dynamics of sand, 1994.

[73] Hamzah M. Beakawi Al-Hashemi and Omar S. Baghabra Al-Amoudi. A review on the angle of repose of granular materials, 2018.

[74] R E Riley and H H Hausner. Effect of particle size distribution on the friction in a powder mass. *Int. J. Powder Met. 6: 17-22(Jan 1970).*, 1 1970.

[75] C.R. Jones, A. Corona, Carlos Amador, and Peter Fryer. Dynamics of fabric and dryer sheet motion in domestic clothes dryers. *Drying Technology*, 40:1–18, 05 2021.

[76] H. Chen, Y.G. Xiao, Y.L. Liu, and Y.S. Shi. Effect of Young's modulus on DEM results regarding transverse mixing of particles within a rotating drum. *Powder Technology*, 318, 06 2017.

[77] C.V. Liew, A.D. Karande, and P.W.S. Heng. In-line quantification of drug and excipients in cohesive powder blends by near infrared spectroscopy. *International Journal of Pharmaceutics*, 386(1):138–148, 2010.

[78] Maitraye Sen, Subhodh Karkala, Savitha Panikar, Olav Lyngberg, Mark Johnson, Alexander Marchut, Elisäbeth Schäfer, and Rohit Ramachandran. Analyzing the mixing dynamics of an industrial batch bin blender via discrete element modeling method. *Processes*, 5(2), 2017.

[79] Amit Mehrotra and Fernando J. Muzzio. Comparing mixing performance of uniaxial and biaxial bin blenders. *Powder Technology*, 196(1):1–7, 2009.

[80] J Mellmann. The transverse motion of solids in rotating cylinders—forms of motion and transition behavior. *Powder Technology*, 118(3):251–270, 2001.

[81] Tongge Wen, Xiangyuan Zeng, Ziwen Li, and Yonglong Zhang. Size segregation under different gravity levels by using polyhedral particles. *Planetary and Space Science*, 226:105634, 2023.

[82] Matthias Schröter, Stephan Ulrich, Jennifer Kreft, Jack B. Swift, and Harry L. Swinney. Mechanisms in the size segregation of a binary granular mixture. *Phys. Rev. E*, 74:011307, Jul 2006.

[83] Troy Shinbrot and Fernando J. Muzzio. Reverse buoyancy in shaken granular beds. *Phys. Rev. Lett.*, 81:4365–4368, Nov 1998.

[84] Troy Shinbrot. The brazil nut effect — in reverse. *Nature*, 429(6990):352–353, May 2004.

[85] Daniel C. Hong, Paul V. Quinn, and Stefan Luding. Reverse brazil nut problem. *Physical review letters*, 86(15):3423–3426, Apr 2001. Article.

[86] Andreas Breu, Hans-Martin Ensner, Christof Kruelle, and Ingo Rehberg. Reversing the brazil-nut effect: Competition between percolation and condensation. *Physical review letters*, 90:014302, 02 2003.

[87] S.Y. He, J.Q. Gan, D. Pinson, and Z.Y. Zhou. Particle shape-induced radial segregation of binary mixtures in a rotating drum. *Powder Technology*, 341:157–166, 2019. Continuous Manufacturing/Processing.

[88] Decai Huang, Ming Lu, Surajit Sen, Min Sun, Yaodong Feng, and Anna Yang. Spin brazil-nut effect and its reverse in a rotating double-walled drum. *The European Physical Journal E*, 36(4):41, Apr 2013.

[89] Marleen Arntz, Wouter den Otter, Wim Briels, Paul Bussmann, Hendrik Beeftink, and Remko Boom. Granular mixing and segregation in a horizontal rotating drum: A simulation study on the impact of rotational speed and fill level. *AIChE J.*, 54:3133–3146, 12 2008.

[90] S.H. Chou, L.T. Sheng, W.J. Huang, and S.S. Hsiau. Segregation pattern of binary-size mixtures in a double-walled rotating drum. *Advanced Powder Technology*, 31(1):94–103, 2020.

[91] Ahmed Jarray, Hao Shi, Bert J. Scheper, Mehdi Habibi, and Stefan Luding. Cohesion-driven mixing and segregation of dry granular media. *Scientific Reports*, 9(1):13480, Sep 2019.

[92] Koyel Sen, Natasha Velez, Carl Anderson, James K. Drennen III, Ahmed S. Zidan, and Bodhisattwa Chaudhuri. Multicomponent granular mixing in a bohle bin blender-experiments and simulation. *International Journal of Pharmaceutics*, 578:119131, 2020.

[93] Migyung Cho, Prashanta Dutta, and Jaesool Shim. A non-sampling mixing index for multicomponent mixtures. *Powder Technology*, 319, 07 2017.

[94] Mariagrazia Marucci, Banien Al-Saaigh, Catherine Boissier, Marie Wahlgren, and Håkan Wikström. Sifting segregation of ideal blends in a two-hopper tester: Segregation profiles and segregation magnitudes. *Powder Technology*, 331:60–67, 2018.

[95] ASTM. Standard Practice for Measuring Sifting Segregation Tendencies of Bulk Solids. `https://www.astm.org/d6940-18.html`, 2020. Acessado em 14/04/2023.

[96] Fuji Jian. A review of distribution and segregation mechanisms of dockage and foreign materials in on-farm grain silos for central spout loading. *KONA Powder and Particle Journal*, 39:100–109, 2022.

[97] Tong Deng, Vivek Garg, Hamid Salehi, and Michael S.A. Bradley. An experimental study on free-surface rolling segregation and correlations with angle of repose and particle sphericity. *Powder Technology*, 379:307–320, 2021.

[98] Emilia Jakubowska and Natalia Ciepluch. Blend Segregation in Tablets Manufacturing and Its Effect on Drug Content Uniformity—A Review. *Pharmaceutics*, 13(11), 2021.

[99] Mohammadreza Alizadeh, Ali Hassanpour, Mehrdad Pasha, Mojtaba Ghadiri, and Andrew Bayly. The effect of particle shape on predicted segregation in binary powder mixtures. *Powder Technology*, 319:313–322, 2017.

[100] Nicolin Govender. Study on the effect of grain morphology on shear strength in granular materials via gpu based discrete element method simulations. *Powder Technology*, 387:336–347, 2021.

[101] M. Lemieux, F. Bertrand, J. Chaouki, and P. Gosselin. Comparative study of the mixing of free-flowing particles in a v-blender and a bin-blender. *Chemical Engineering Science*, 62(6):1783–1802, 2007.

[102] Albert Alexander, Paulo E. Arratia, Christopher L. Goodridge, Osama S. Sudah, Dean Lance Brone, and Fernando J. Muzzio. Characterization of the performance of bin blenders: Part 1 of 3: Methodology. *Pharmaceutical technology*, 28:70–86, 2004.

[103] Nicolin Govender, Raj Rajamani, Daniel N. Wilke, Chuan-Yu Wu, Johannes Khinast, and Benjamin J. Glasser. Effect of particle shape in grinding mills using a GPU based DEM code. *Minerals Engineering*, 129:71–84, 2018.

[104] Luís Marcelo Tavares, Victor A. Rodriguez, Marina Sousani, Carles Bosch Padros, and Jin Y. Ooi. An effective sphere-based model for breakage simulation in DEM. *Powder Technology*, 392:473–488, 2021.

APPENDIX A – ON THE EFFECTS OF MASS UPSCALING IN POLYHEDRAL PARTICLES

Throughout Parts I and II, in which the calibration of polyhedral and spherical particles is demonstrated at different particle scales, one common given reason for the behaviour of some polyhedral calibrations are "mass effects" (i.e. changes in bulk behaviour due to increased particle mass). Here, this idea is further developed to provide some clarity to the reasoning behind these claims.

Repose angle formation is strongly related to rotational motion, as evidenced by spherical simulations and Fig. A.1, which shows the same material and scaling with (A) and without (B) rolling damping on the ledge test. As discussed in Section 2.2, rolling friction is a mathematical tool to account for non-sphericity and is not needed in polyhedral particles, as resistance to rolling is offered by the particle's own particular shape.

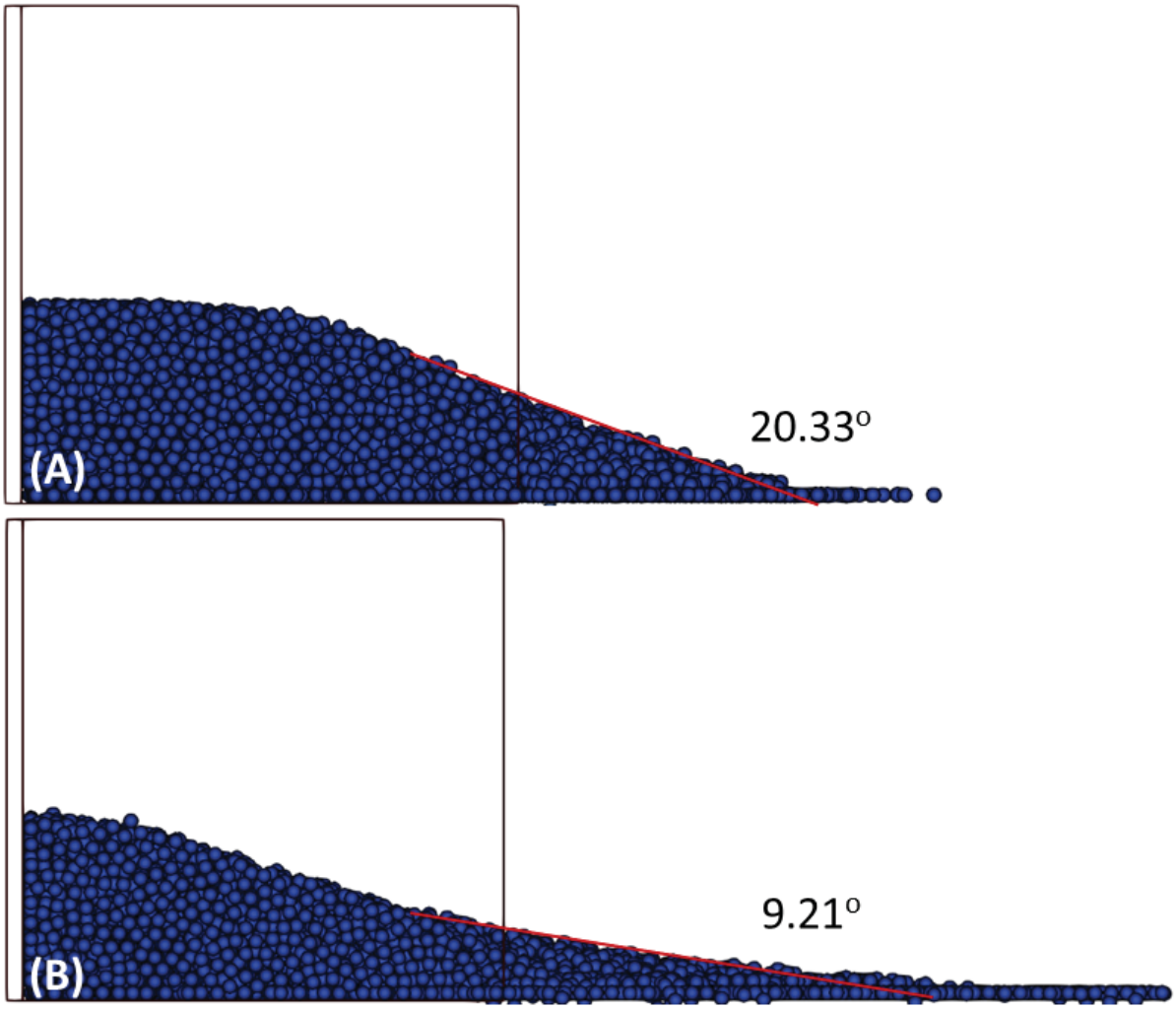

Figure A.1: Ledge test simulations at 30x scale with (A) and without rolling damping (B). The angle of repose is considerably increased by the presence of the artificial counter-torque to rolling motion. Moreover, more particles leave the simulation domain in (B) due to excessive rolling.

In Section 4.2.2, which discusses the upscaled simulations of the ledge test, it is stated that for the 40x polyhedral case, the Angle of Repose is increased due to the stability of cubes

added to the relatively big masses achieved in that case. The mathematical construction of this stability is given by Euler's moment equation:[7]

$$\begin{aligned} \tau &= \dot{H} + \omega \times H \\ H &= I\omega \end{aligned} \tag{A.1}$$

where τ is the applied torque, ω the angular velocity and H the angular momentum, which is then given by the product of angular velocity and I, the inertia tensor. The last parameter (also called moment of inertia) is hence analogous to rolling damping, as it controls the relationship between torque and angular motion – with the important caveat that it is a real physical property and not a mathematical device.

DEM is perhaps more concerned with the "reversed" form of Equation A.1: we wish to calculate $\dot{H}$, or the variation in angular momentum, due to a know, computed torque. It is clear from the above equation that larger values of the inertia tensor reduce this "conversion" into angular motion. Euler's equation is calculated with an axis fixed to the body and, in the case of DEM, about the particle's center of mass; thus, the inertia tensor is given by:

$$I = mL^2 \tag{A.2}$$

where L is a characteristic length (depending on the particle's shape) originating from the pivot point (here, the center of gravity), and m is the particle mass. Thus, particle mass and size increase the inertia tensor, which in turn increases the particle's resistance to rotation.

Finally, the nature of the acting torque needs to be defined. As argued in the aforementioned Section 4.2.2, gravity is unable to dislodge particles from their stable, packed positions. For an arbitrary geometric point in a cube (e.g. a vertex), the gravitational torque is given by $\tau_g = mgL\sin\theta$; while this equation is proportional to mL, I is proportional to mL^2, showing that resistance to angular motion increases at a greater pace than the corresponding torque, thus explaining the observed "mass effects".

The above hypotheses can be simply verified by varying the two main parameters – gravity and inertia tensor – and observing the impact on the angles of repose. While BlazeDEM automatically computes the moment of inertia, it can be reescaled by a user-defined parameter. Figure A.2 shows the anomalously high ledge test AoR for the free-flowing material (A) in Part I and compares it to two other runs of the same scale and material, with increased gravity (B) and reduced inertia tensor (C). In both cases there is a reduction in repose angles, which become closer to the calibrated 30x case.

Figure A.3 is the reverse idea: to the correctly calibrated 30x scale, the inertia tensor was increased. As shown in (B), there is a sharp increase in AoR, which approaches the original 40x run. Therefore, it is reasonably demonstrated that the inertia tensor plays a key role in the disparities observed between 30x and 40x polyhedral calibrations. An argument could be made that, based on the above discussion, it is length rather than mass that causes this phenomenon, but physically the resistance to rolling (and, by extent, the inertia tensor) has to necessarily arise from particle mass; hence, the name "mass effects".

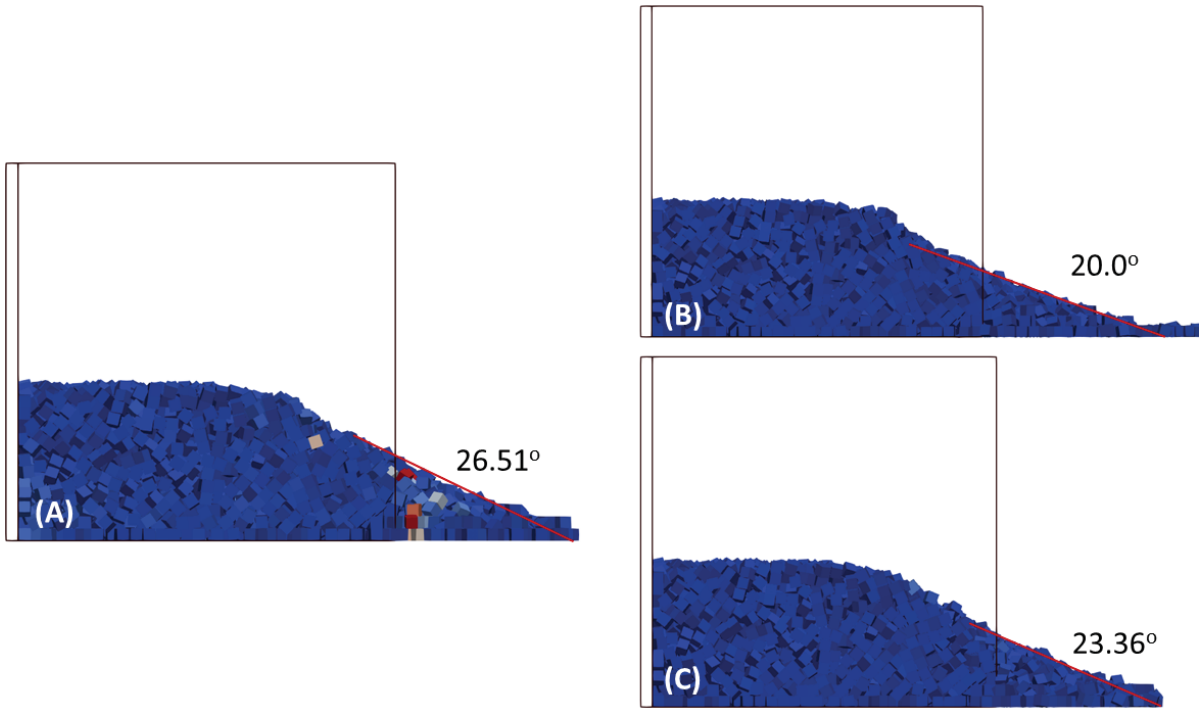

Figure A.2: Ledge test AoRs for the free-flowing material, at 40x scaling, using polyhedral particles. In (A), the original result from Part I is reproduced, while a case with higher gravity (B) and reduced inertia tensor (C) are also presented.

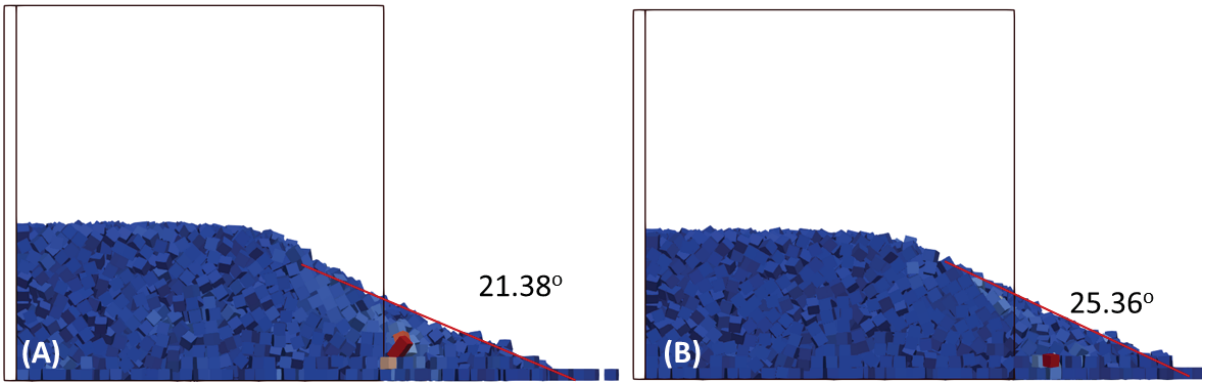

Figure A.3: Ledge test AoRs for the free-flowing material, at 30x scaling, using polyhedral particles. In (A), the original result from Part I is reproduced, while in (B) the same material is simulated with a higher inertia tensor. An increase in AoR is observed due to increased resistance to rolling.

APPENDIX B – IN-BIN BLENDER IMAGES

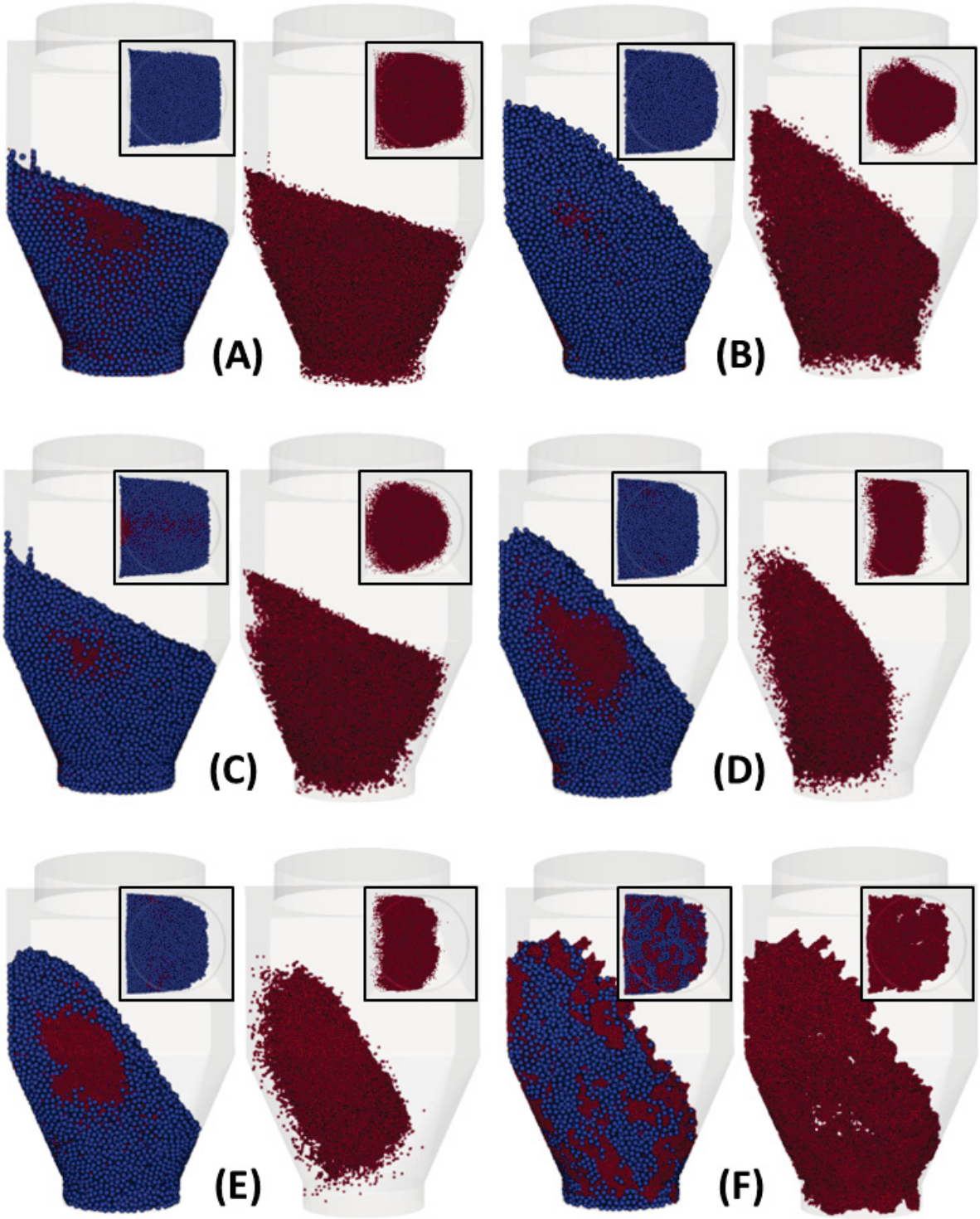

Figure B.1: Mixture 1 simulation results using modified parameters; FFM is shown in blue, while CM is coloured red. Insets on the frontal IBB show the top view for the associated frontal image. A single parameter of the original attempt was changed for each run: the static (A, B) and rolling (C, D) friction coefficients were set to 0 and 1, respectively, while CM cohesion was increased to (E) 0.5 and (F) 1.0.

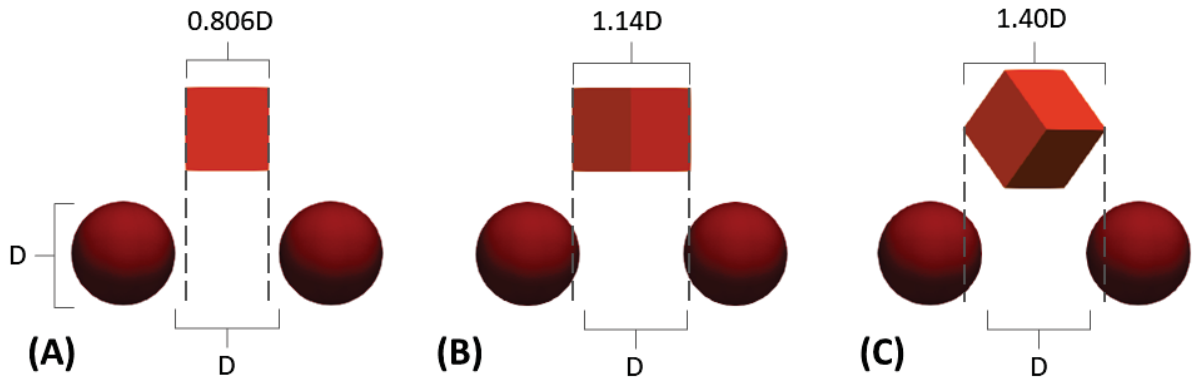

Figure B.2: Illustration on the effect of particle shape on percolation. Depending on cube orientation with relation to an arbitrary particle gap (for simplicity, equal to the sphere diameter D), the percolation "characteristic length" changes to (A) side length, (B) face diagonal and (C) body diagonal. If the same cube were to be simulated as a sphere of diameter D, percolation would happen with equal ease across all cases.

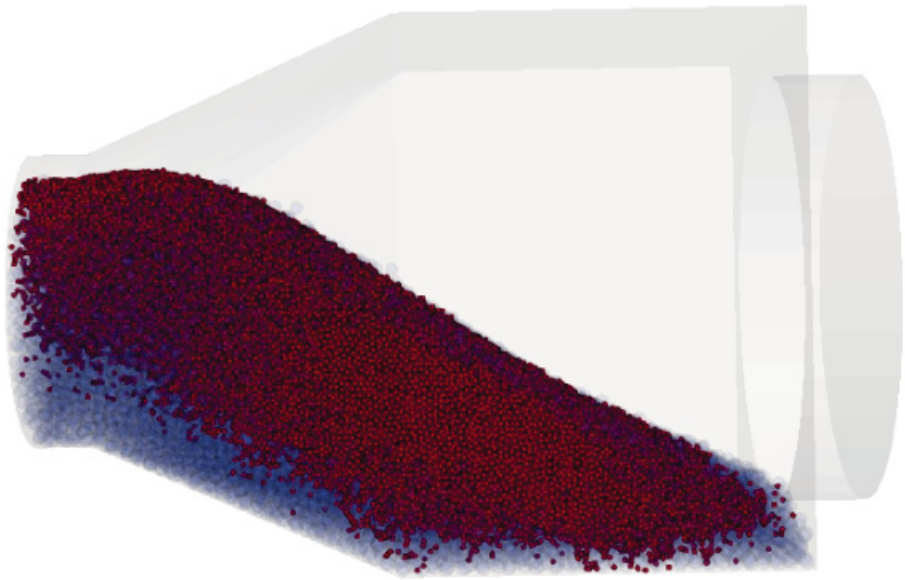

Figure B.3: Mixing state of the 0.0 Rolling Damping case, at 27.4 seconds and 1/4 of a revolution. CM (red) is partially distributed in FFM (blue, translucent for ease of viewing).

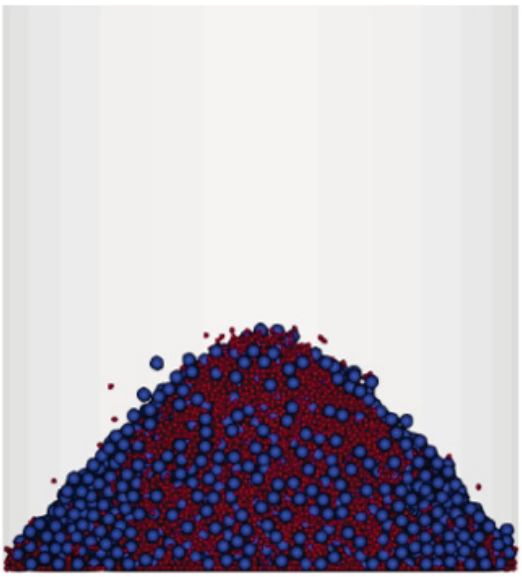

Figure B.4: A simulation of sifting segregation on a cylindrical bin, using calibrated FFM and CM. Both were filled as a mixture by a narrow circular region placed in the middle, so that the impact point for pile formation was the center of the bin. The finer CM particles concentrate around the impact point, while bigger FFM particles roll to the sides. The cylinder is sliced lengthwise, so that the inside of the pile can be visualized.

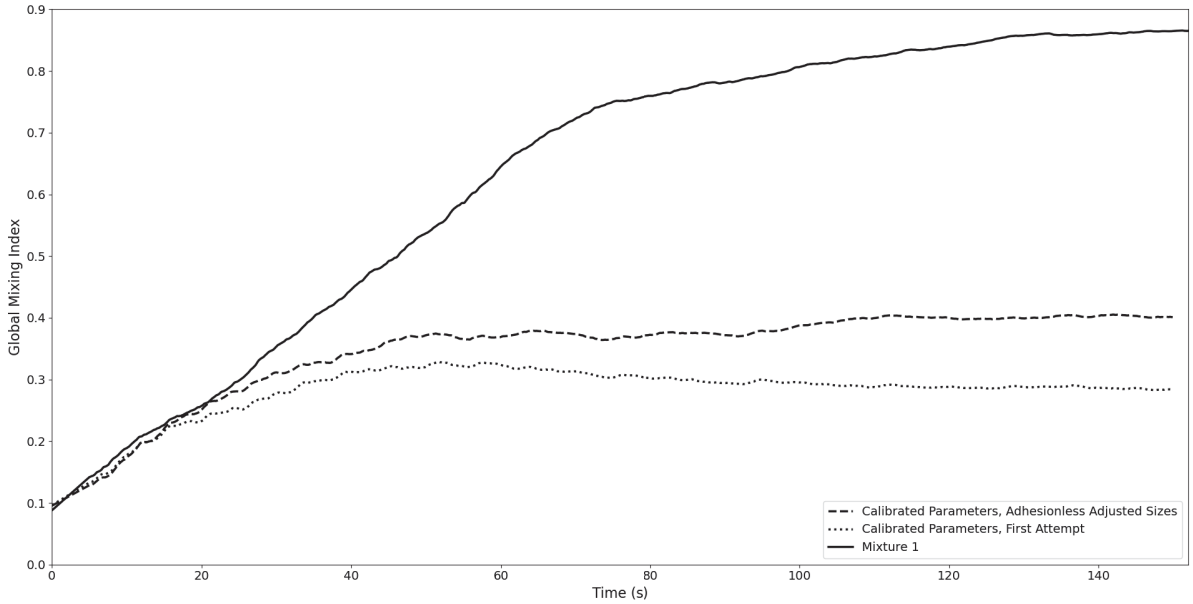

Figure B.5: Global mixing indices over time for three attempts at simulating Mixture 1. The dotted line reproduces the curve obtained in Section 6.2, using original particle sizes and calibrated parameters. Dashed line uses the same parameters, but particle sizes and PSDs have been readjusted. Finally, the solid line improves on the previous attempt by including an adhesive FFM-CM parameter that greatly improves mixing.

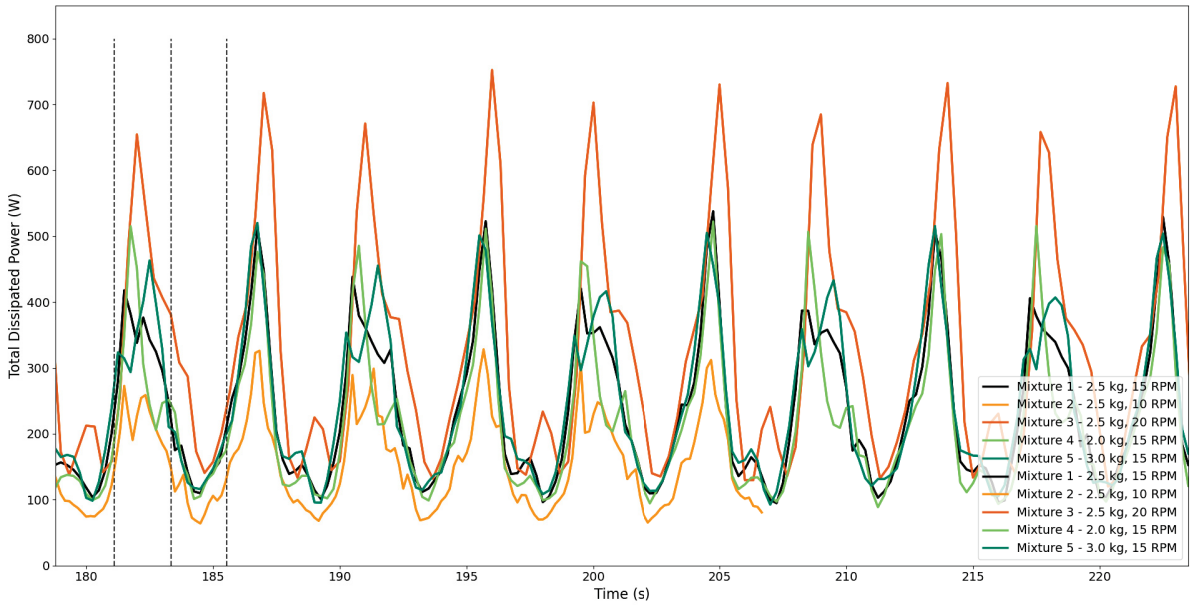

Figure B.6: Total Dissipated Power by all mixtures between the twenty-first and twenty-fifth revolutions (times in Mixtures 2 and 3 were rescaled to match other cases). Hence, Fig. 6.10 is here extended to encompass more revolutions, thus showing pattern repeatability in the original image. The auxiliary dotted lines are kept for reference.